Crystal Plasticity based Formability Analysis of Transformation Induced Plasticity Steels

by

Pingcheng Zhang

A thesis

presented to the University of Waterloo

in fulfillment of the

thesis requirement for the degree of

Master of Applied Science

in

Mechanical and Mechatronics Engineering

Waterloo, Ontario, Canada, 2018

AUTHOR'S DECLARATION

This thesis consists of material of which I authored or co-authored: see Statement of Contributions included in this thesis. This is a true copy of the thesis, including any required final revisions, as accepted by my examiners.

I understand that my thesis may be made electronically available to the public.

STATEMENT OF CONTRIBUTIONS

The following co-authors have contributed to the current work:

Professor Kaan Inal supervised this MASc thesis.

Professor Shi-Hoon Choi provided the microstructural and experimental data set for duplex stainless steel that was used to calibrate the numerical framework.

Dr. Christopher Kohar assisted with the drafting of the numerical implementation chapter and assisted in structuring, proof reading and editing of this work.

Dr. Abhijit Brahme provided research guidance, converted EBSD measurements to the synthetic microstructure for simulations, pole figures and orientation distribution functions.

The balance of this work is my own.

ABSTRACT

This thesis outlines a framework to model to aid the development and utilization of transformation induced plasticity (TRIP) assisted multiphase steels in the automotive industry for light weighting applications. Automakers rely on accurate characterization and prediction of sheet metal formability to implement these materials into the structure successfully. They rely on accurate numerical models for predicting and evaluating sheet formability compared to the costly experimental method. However, predictive modeling of TRIP steel in formability is difficult due to the combination of dislocation and transformation mechanisms occurring during deformation for various strain paths. This research is aimed to provide a tool to quickly and accurately capture the micro and macro mechanical response of TRIP assisted steels, as well as calculating the forming limit diagram used in evaluating formability.

This thesis presents a rate-dependent Taylor type elasto-viscoplastic crystal plasticity model with a micro-mechanics based transformation criteria to simulate the mechanical response of TRIP steel. A new stress-based transformation criterion, based on the micromechanics of habit-plane interaction, was developed to initiate transformation. This model inherently captures the triaxiality effect of martensite through the accumulated shear strain on slip systems. Simulations are calibrated and compared to experimental measurements of Duplex Stainless Steel (DSS). Simulations of single crystal and polycrystalline aggregates show that although high Schmid factor habit planes were favourable for transformation, competition exists between the lower Schmid factor dislocation planes that generate higher elastic stress needed for transformation. The calibrated model is then used to predict the forming limit diagram using the Marciniak-Kuczynski approach. The mechanism of transforming from low strength austenite to high strength martensite showed enhanced formability by at least 20% compared to without transformation. This is achieved by the TRIP mechanism suppressing localization at critical moments during deformation. However, the single variant martensite selection scheme had a negligible influence on formability predictions. Through a parametric study of the transformation criteria, formability can be enhanced on the biaxial regime by up to 13% over the baseline DSS material. Conversely, poor control of the transformation parameters could lead to a reduction of 50% in formability. The results highlight the importance of a physics based simulation to utilize TRIP assisted steels fully.

iv

ACKNOWLEDGEMENTS

First, I would like to thank my supervisor Professor Kaan Inal for accepting me into the graduate program at the University of Waterloo Computational Mechanics Research Group, and the years of support, leadership, assistance, and guidance he has provided me. Professor Shi-Hoon Choi from the Suncheon National University of the Republic of Korea for providing valuable EBSD, microstructure and experimental data for model calibration. I also gratefully acknowledge Dr. Christopher Kohar and Dr. Abhijit Brahme for providing guidance and discussions throughout the completion of this work. Next, I would like to thank my friends, colleagues at the University of Waterloo, Computation Mechanics Research Group, and members of DotS both past, present, and future; for all the company, support, positive energy, time and most importantly memories together.

Lastly, I would like to thank my family: To my dad, Robert, for being strict and supportive at the right times. To my mom, Susan, for spoiling and disciplining me in her own way. To my brother, Dong, who constantly makes me accountable to be a good role model. To my project car, for providing the worst enjoyment to time and money ratio of all time, and always being in the back of my mind.

TABLE OF CONTENTS

LIST OF FIGURES

ix

LIST OF TABLES

1 INTRODUCTION

Government mandated carbon footprint and fuel economy targets for highway vehicles in the form of Combined Average Fuel Economy (CAFE) standards have been encouraging vehicle mass reduction developments. Enacted by the United States Congress in 1975, CAFE's purpose was to reduce energy consumption by increasing the fuel economy of cars and light trucks in North America [1]. There are several ways to improve fuel economy:

1) Improvement of aerodynamics by reducing drag.

2) Improve drivetrain efficiency such that more energy is converted to forward motion.

3) Reduce the weight of the vehicle.

Studies have shown that only 12-15% of the energy in fuels overcome the forces that resist forward motion, of these, vehicle weight most significantly affects inertial and rolling resistance forces [2]. A 10% reduction in vehicle weight yields 5-6% improvement in fuel economy [2]. After CAFE's implementation, the adjusted fuel economy of vehicles immediately increased by 70% (seen in Figure 1) through drastic vehicle weight reduction programs. However, manufacturers are ever challenged to balance demand for increasing fuel economy expectations with more progressive standards in government standards in vehicle safety, such as the National Highway Traffic Safety Administration (NHTSA) and European New Car Assessment Program (Euro NCAP) [3], and vehicle performance.
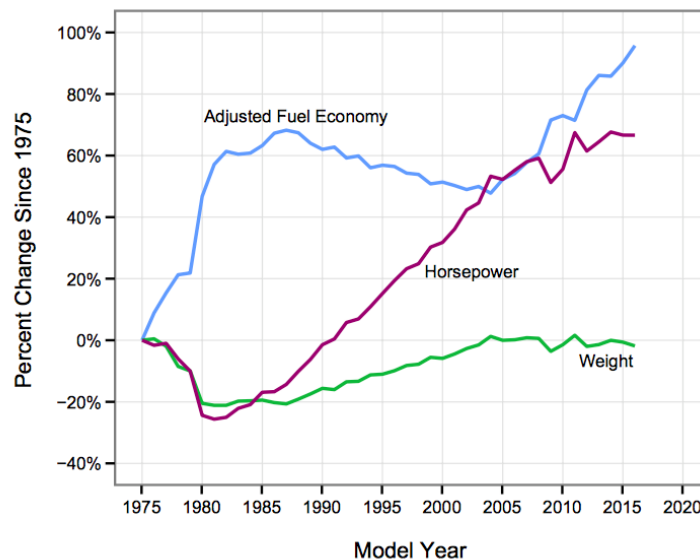
Figure 1: Vehicle Mass, Horsepower and Fuel Economy from 1975-2016 [4]

Automakers have been accomplishing the goal of vehicle lightweighting by reducing the body in white mass [5] through the intelligent use of new and advanced light weight alloys [6] [7] [8] [9] [10], composites [11] [12] and high strength steels [13] [14] [15]. Advanced High Strength Steel (AHSS) has been used to achieve weight savings by replacing conventional steel components that are strength limited, such as the roof structure, B-pillars, bumpers, with thinner gauges of steels with higher strength. Furthermore, additional weight savings with AHSS has been achieved by further stretching the material to yield a higher thickness reduction throughout a component during manufacturing. Since the early 1980s, the automotive industry has accelerated the development of AHSS to exploit their benefits and capabilities fully. AHSS includes dual phase (DP) steel [16] [17] [18] [19] [20], transformation induced plasticity steel [21] [22] [23] [24] [25] [26] [27] [28], complex phase steels [29] [30], hot stamping steels [31] [32] [33] [34] [35], twinning induced plasticity (TWIP) steels [36] [37] [38] [39] and Quench and Partitioning (Q&P) steels [40] [41] [42]. "TRansformation Induced Plasticity (TRIP)" steels were developed to take advantage of the transformation of austenite to martensite induced by deformation. Steels exhibiting the TRIP deformation mechanism offer increased strength and increased elongation [43]. Due to these characteristics of TRIP steels, it is an excellent candidate to reduce the weight of formability limited components on a vehicle. To utilize these materials, the development of accurate simulation tools is critical to its successful deployment in the automotive industry. The focal area of this research contributes to the development of a predictive simulation tool that can capture the TRIP mechanism for multiphase AHSS under deformation.

Two classifications of modeling techniques have been developed to simulate the mechanical response of steels: phenomenological based macro-scale plasticity and micro-scale polycrystalline plasticity. A macro-scale plasticity model approximates the physical behavior of the material via mathematical equations of various functionalities that depend on the application. The micro-scale polycrystalline plasticity model, also known as crystal plasticity, is a physics-based model, which computes the crystallographic slip resulting from dislocation glide on individual crystal lattices with the highest atomic density [44]. The cumulative sum of all the different crystal orientations comprises the texture of the overall material. Initial texture bias naturally gives rise to anisotropy due to the readily available slip systems in specific directions. Upon initiation of dislocation glide, the crystal lattice will shear and accumulate. During the deformation process, the orientation of the crystals will change due to rotation, leading to an

2

evolution of the microstructure and anisotropy. In a material like steel, the main deformation mechanism is dislocation glide at room temperature, which is a fairly well understood mechanism. However, the TRIP mechanism observed in AHSS is complex and still requires substantial attention to capture the macro and micro-mechanical behavior in simulations of large deformation, let alone predict the formability of these materials.

The objective of the present work is the development of micro-scale predictive simulation tool to capture the TRIP mechanism from austenite to martensite in multiphase AHSS to enable its use vehicle light weighting strategies. The proposed transformation framework will take advantage of the micro-scale physics and trigger transformation based on an evolving transformation criteria that can be related to several physical phenomena observed in experiments. The successful implementation of the proposed model will then be used to simulate the mechanical response of a duplex stainless TRIP steel (65% ferrite, 35% austenite). Once calibrated, the *Marciniak and Kuczynski* (MK) [45] framework will be used to calculate forming limit diagrams (FLDs) to evaluate formability of this TRIP-assisted steel. The transformation criteria will be varied, and its effect on the FLD will be studied in detail to provide insight into the formability characteristics of AHSS that exhibit the TRIP effect.

This thesis is structured as follows: In Chapter 2, the background of AHSS and the physics of the TRIP effect is presented. A review on crystal plasticity micromechanical modeling and the various transformation criteria currently existing in literature is presented. Sheet metal forming techniques for TRIP assisted steels are also presented in this chapter. Chapter 3 identifies the scope and objective of the research. Chapter 4 details the constitutive model of the elasto-viscoplastic Taylor type crystal plasticity model, the selected transformation criteria, and the numerical implementation of the proposed framework. Chapter 5 presents the *Marciniak and Kuczynski* (MK) [45] framework for calculating forming limit diagrams. Chapter 6 presents the calibration process of the mechanical properties and experimental measurements for the TRIP-assisted steel used in this study. In Chapter 7, simulations of single crystal textures, which highlight the transformation mechanism, are presented. Simulations of the polycrystalline response for different strain paths is also presented. Finally, simulations and parametric studies of formability are presented. Chapter 8 presents a summary of the key conclusions and a list of future works to improve upon this framework.

2 BACKGROUND AND LITERATURE REVIEW

2.1 Advanced High Strength Steel

The need for automakers to satisfy customer demands and government mandates for fuel efficient vehicles has accelerated research and development into lightweight vehicles structures. The steel industry and automakers are attempting to replace low alloy carbon steel with thinner gauge high strength steel to reduce the mass throughout the vehicle in a manner that satisfies a wide range of safety and performance targets [46]. Advanced High Strength Steels (AHSS) is a new and ever evolving classification of high strength steel that has been developed to satisfy the needs of the auto industry. There exist different generations of AHSS for use in the auto industry, which are classified by their alloying elements and manufacturing process technologies. In each of these generations, there are trade-offs between the tensile strength and elongation strain to failure. Figure 2 presents a graphical representation of the various grades of AHSS that highlights this trade-off between tensile strength and elongation.
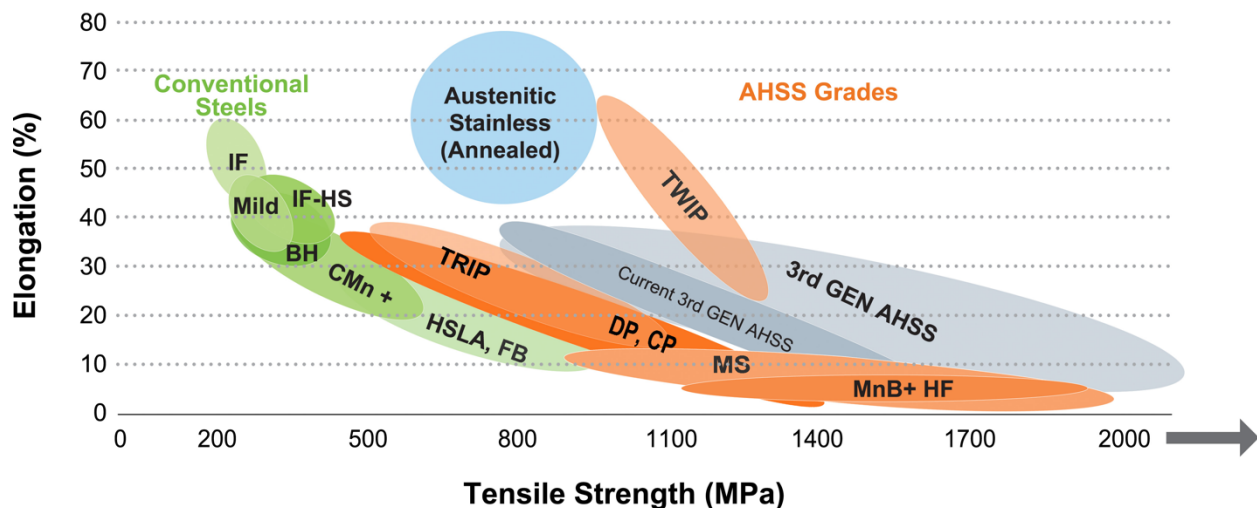
Figure 2: Steel Strength vs Elongation Chart [47]

First generation AHSS employs a variety of alloying elements and processing technologies to achieve microstructure control of different phases, such as austenite, bainite, ferrite, and martensite, where each phase has a trade-off concerning strength, ductility and mechanical properties. By tailoring the microstructure, a wide variety of first generation AHSS can be achieved (i.e. dual phase (DP) steel [48], complex phase (CP) steel [49], martensitic steels and

4

transformation induced plasticity (TRIP) steels [50]). Second generation AHSS use high volume fractions of manganese to supress stacking fault energy during alloying, yielding a heavy austenite microstructure. Instead of the classical dislocation slip mechanism, the low stacking fault energy results in crystals undergoing a large and abrupt rotation, known as twinning. Steels exhibiting this behavior are known as twinning induced plasticity (TWIP) steel, these materials demonstrate incredible strain hardening and uniform elongation strain to failure due to the twining deformation mechanism [51]. However, the incorporation of the manganese alloying element is often too expensive for the implementation of a mass-produced commercial vehicle. The recently developed third generation AHSS uses a quench and partition (Q&P) technique to finely distribute and temper martensite upon an austenite matrix, thus achieving a combination of high strength and ductility. Currently, further developments are enhancing the capabilities of third generation AHSS steel; however, their full potential has yet to be realized. As such, research in the advancement of steel requires the development at several stages including the initial alloy chemical composition and the processing techniques to achieve the desired microstructural configuration.

2.1.1 *Alloying Elements*

The mechanical properties of steel can vary dramatically based on the chemical composition of the alloying elements. These alloying elements affect the formations of carbides through the microstructure that alters the motion of dislocations throughout the grains of a material. Although a significant amount of literature has been dedicated to studying the effects of various steel compositions [52] [53], this current study is limited to the discussion of alloying elements about austenite (γ) and ferrite (α) stabilizers. By adding stabilizing elements to the chemistry, the equilibrium phase diagram for the final phase composition of austenite and ferrite can be modified accordingly:

- γ −stabilizer, expanding the γ −field, and encouraging the formation of austenite over wider composition limits.
- α −stabilizer, contracting the γ −field, and encouraging the formation of ferrite over wider composition limits.

The effects of the stabilizers on the equilibrium diagram depend on some degree of the electronic structure of the alloying element, which is reflected in their relative positions in the periodic classification. Figure 3 presents the classification of stabilizers and their effects on the phase diagram. These stabilizers are classified into the following four categories:
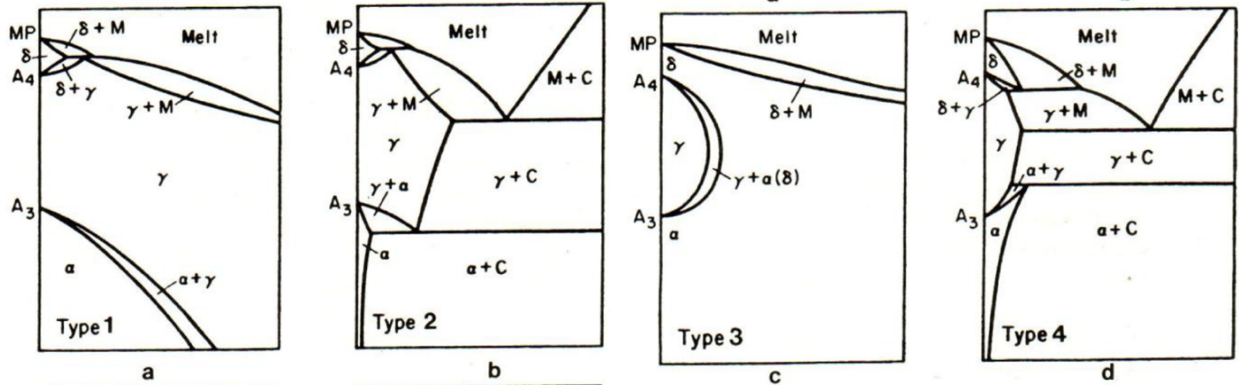
Figure 3: Effects of alloying (a) Open γ - field; (b) expanded γ - field; (c) closed γ - field; (d) contracted γ - field [54]

Type 1: Open γ −field (Ni, Mn, Co, inert metals such as Pt): These alloying elements widens the temperature range for stable austenite by depressing the $\alpha - \gamma$ transformation and raising the $\gamma - \alpha$ transformation. Both Ni and Mn, if added in sufficient concentration, eliminate the body center cubic α −iron phase and replace it, down to RT, with the γ −phase.

Type 2: Expanded γ −field (C, N, Cu, Zn, Au): Carbon and nitrogen are the most important elements in this group. The γ −phase field is expanded, but its range of existence is cut short. The expansion of the γ −phase by carbon, and nitrogen, underlies the heat treatment of steels, by allowing formation of solid solution (of austenite).

Type 3: Closed γ −field (Si, Al, Be, P, Ti, V, Mo, Cr): Many elements restrict the formation of γ −iron causing the γ −area of the diagram to contract. This encourages the formation of ferrite. One result is that the δ − and α − phase fields become continuous, such that they not amenable to the normal heat treatments involving cooling through the γ/α phase transformation.

Type 4: Contracted γ −field (B, Ta, Zr, Nb): The γ −loop is strongly contracted, but is accompanied by compound formation.

2.1.2 Equilibrium Phase Transformation

Over the years, steel manufacturers have generated an enormous database for processing conditions of steel that are dependent on the initial chemical composition. The equilibrium phase diagram was initially developed to characterize the physical state of single substances over a range of temperature and pressures. However, adaptations of the phase diagram were used to characterize steel microstructure at varying chemical compositions through a binary mixture plot [55]. The most commonly used diagram for steel making is the Iron-Iron carbide phase diagram, where iron-carbon phase combinations are characterized. For steels with more complex chemistries, a carbon equivalent can be calculated that relates the combined effects of different alloying elements used to an equivalent amount of carbon.

Figure 4 presents a typical iron-carbon phase diagram under equilibrium conditions. Several regions signify the various phase and phase combinations of austenite (γ-Fe), ferrite (α-Fe), cementite (Fe_3C) and graphite that can be achieved through uniform cooling of the bulk mixture. This cooling allows diffusion of the carbon content throughout the material to achieve the lowest energy state. Thus, the diagram can be used to calculate the resulting phase composition based on distances from various regions on the diagram.
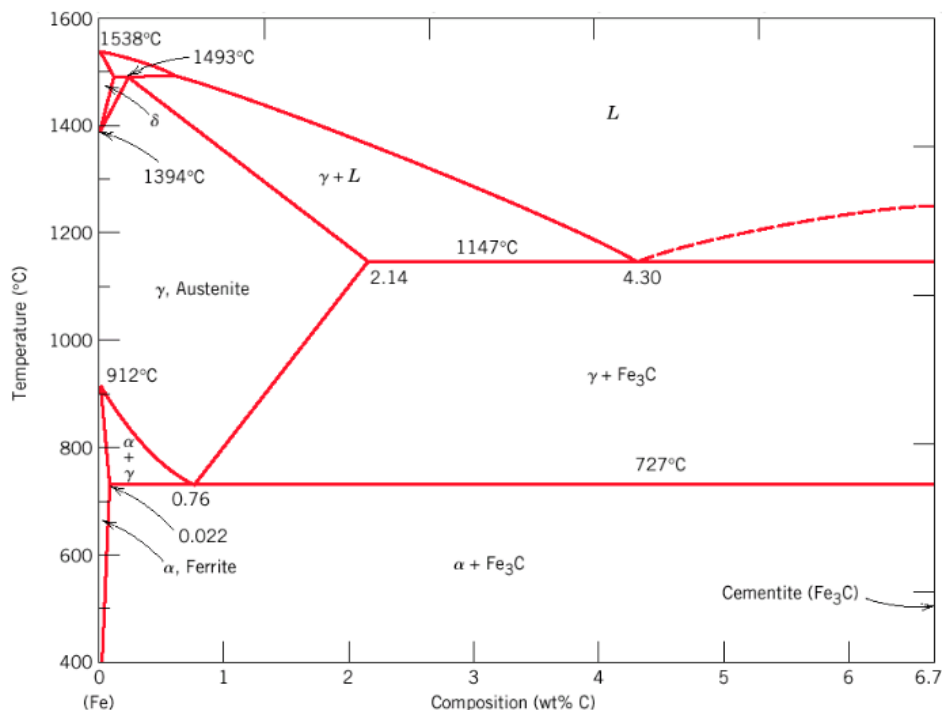
Figure 4: Iron - carbon phase diagram [56]

7

2.1.3   Time Temperature Transformation

In the equilibrium phase transformation, the cooling schedule is often over a sufficiently long period to allow for the equilibrium of the alloy mixture at the lowest energy state. However, during various cooling schedules, the individual phase can deviate from equilibrium to arrive at a unique phase. Once cooled to a lower temperature, the energy of the lattice atoms will be too low for diffusion to establish equilibrium and thus, preserves the metastable phase [52]. These metastable phases include austenite, bainite, martensite and pearlite. This introduces a time temperature transformation (TTT) phenomenon that allows steel to adopt more complex microstructures through careful control of the cooling rate and temperature.
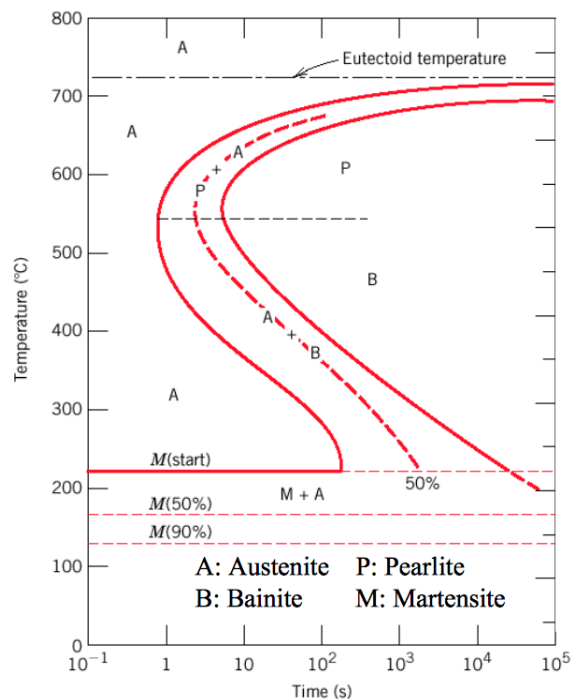
Figure 5: TTT diagram for steels [56]

Figure 5 presents a typical TTT diagram of steel. The TTT diagram describes the conditions where metastable phases can be obtained with constant cooling rates during a controlled quenching process. Over time, further processing technology improvements explored holding the material at different temperatures and cooling rates to generate more complex microstructures [57]. To form martensite, the material is typically cooled very rapidly (quenched) from a high temperature where austenite is stable. Due to the time constraint nature of the quenching process, a diffusion-less transformation occurs where the resultant phase takes on the chemical composition of the parent

8

phase. With this quenching technique, steel phases with unique chemical compositions, as well as unique mechanical properties, are obtained at RT.

2.1.4   Crystal Arrangements of Steels

Several critical micromechanical phases in steels are inherently composed of many repeating atom arrangements called "lattice cell" structures. Common lattice arrangements are cubic, body-centered cubic (BCC), body-centered tetragonal (BCT) and face-centered cubic (FCC) seen in Figure 6. Austenite in steels takes the FCC lattice arrangement, while ferrite is observed as BCC. On the other hand, martensite has been observed in BCC and BCT variants, depending on the parent phase alloying element.

Body Center Cubic   Body Center Tetragonal   Face Center Cubic
       (BCC)   (BCT)   (FCC)
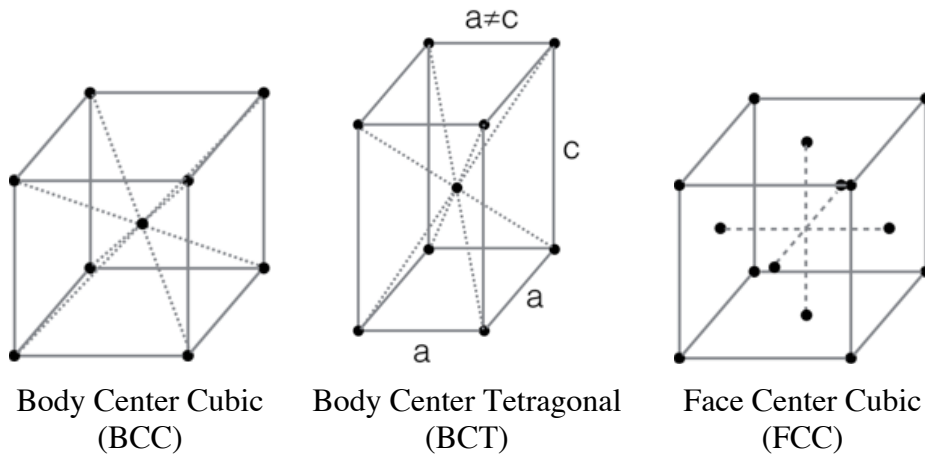
Figure 6: Cubic lattice orientations BCC, BCT and FCC

2.1.4.1   BCC vs BCT Martensite

Due to the generality of martensite to describe any phase formed by diffusion-less transformation, it is necessary to differentiate between the variations of martensite formed in steels. *Olson and Cohen* [58] noted that martensitic variants formed a tetragonal structure caused by lattice distortions of interstitial atoms or the ordering of substitutional atoms (either long or short range) in the parent body center cubic phase. Figure 7 presents a visual representation of iron-carbon system lattice cells distorting the parent lattice. Depending on alloying content and temperature, martensite transformation in Fe-Pd alloys can result in three possible lattice orientations: FCC, BCT, and face center tetragonal (FCT) [59]. Substantial amounts of certain alloying elements have been shown to alter the resultant martensite lattice cell. *Watanabe and*

9

Wayman summarized the findings on martensite structure in Fe-Al-C alloy systems and noted that the addition of 7% aluminum and 2% carbon resulted in high martensite tetragonality [60], while alloying elements such as nickel [61] and platinum [62] had no effect on tetragonality resulting in BCC martensite. *Cayron* [63] acknowledged the existence of both BCC and BCT martensite, however the majority of transformation models assumes the final martensite to take the BCC form.
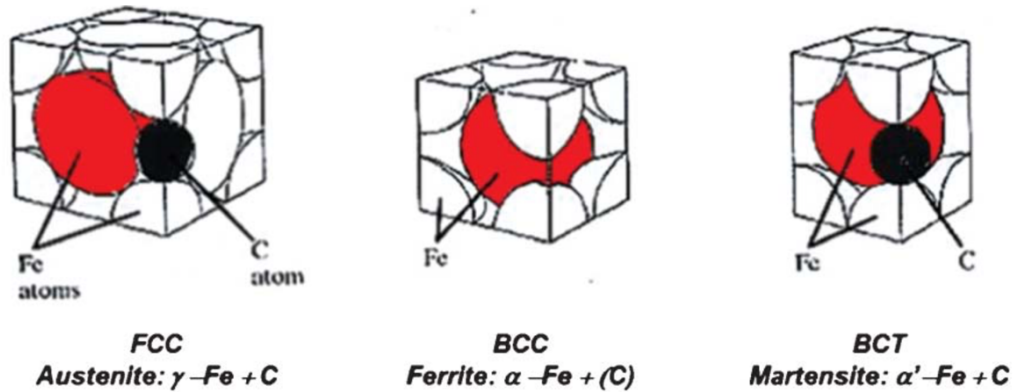
Figure 7: FCC, BCC, BCT Iron-carbon systems [64]

2.1.4.2 Texture

Crystallite aggregates consist of grains, each of which has its own orientation. The distribution of these orientations is usually not random. Amalgam of many grains that represents the microstructure of the material and its orientation represents what is called the "texture". A crystallographic orientation can be represented in 3-dimensional Bunge Euler space ($\varphi_1, \Phi, \varphi_2$). Furthermore, texture can be represented as a 2-dimensional projection called a pole figure for a given projection (i.e. {100}). Figure 8 presents a standard projection of a pole figure with the goniometer set for {100} reflections.
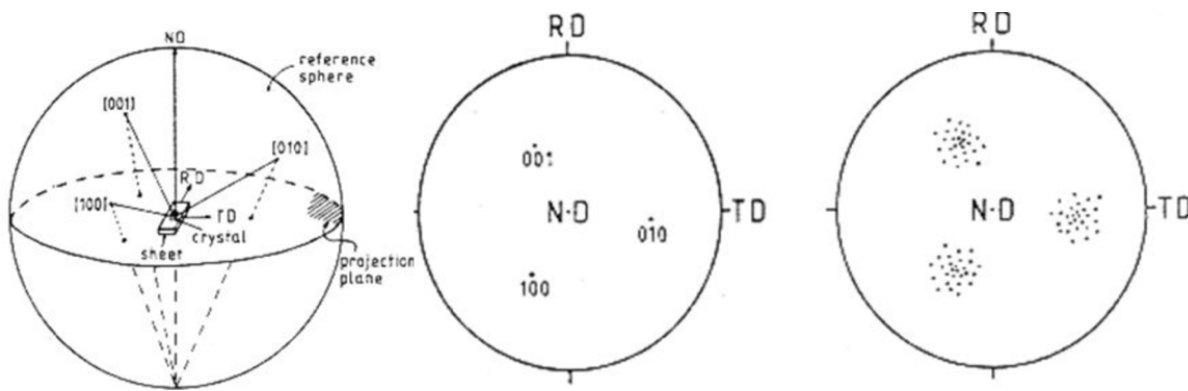
Figure 8: Pole figure of a single crystal with goniometer set for {100} [65]

10

Another method to represent the 3-dimensional Bunge Euler space is using an orientation density function (ODF). A cube is used to represent the entire orientation space and slices through the φ_2 direction is used for analysis, a sample orientation space and ODF plot is shown in Figure 9.
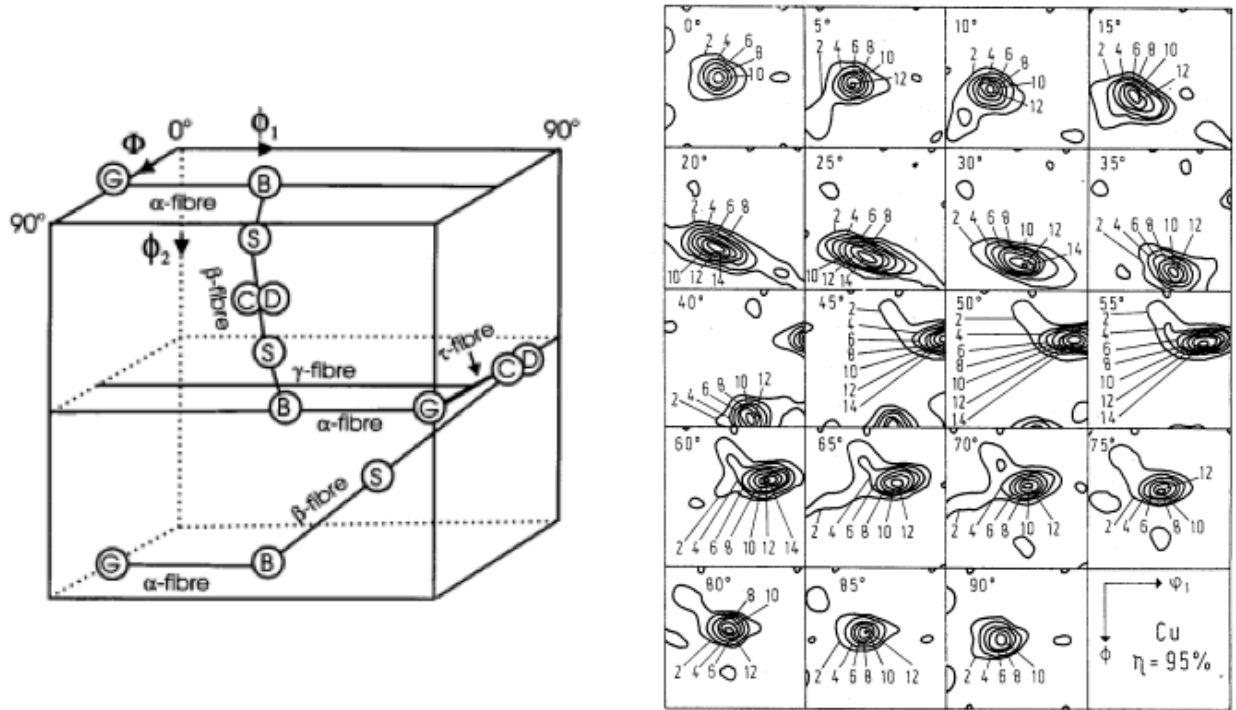
Figure 9: 3D orientation space and ODF slices at 5° slices of the φ_2 direction of a FCC Cu texture [66]

2.2 *Transformation Induced Plasticity (TRIP) Steels*

Martensite remains one of the greatest technological advancements in steels where it can confer an outstanding combination of strength and toughness. However, high volume fractions of martensite often makes the steel brittle and necessitates a tempering treatment to allow carbon to diffuse for enhancing ductility. Transformation induced plasticity (TRIP) steel is a unique classification of First Generation AHSS where metastable austenite transforms into martensite upon mechanical deformation [67] [68]. Many other materials are now known to exhibit the same type of solid-state phase transformation, known as martensite transformation [67]. Taking advantage of the TRIP mechanism, TRIP steels often offer substantially higher work hardening rates, tensile strength and strain elongation when compared to conventional high strength steel and other AHSS, demonstrated in Figure 10. These combinations of mechanical properties elect TRIP

11

steel as an excellent candidate for vehicle structures that require high strength yet flexibility to be formed into complex geometries such as bumper supports, frame rails, roof rails, crash box, B pillar, and seat frames [69].
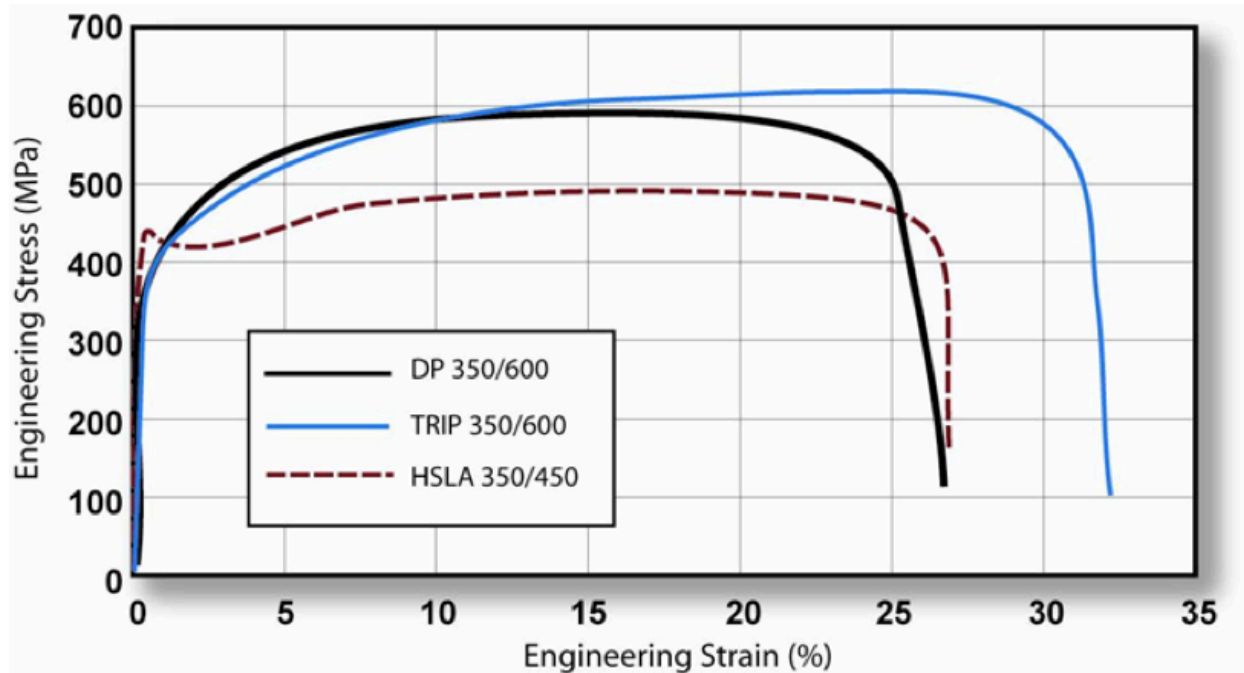
Figure 10: HSLA 350, DP 350 and TRIP 350 Stress Strain Curves [47]

TRIP steels use austenite stabilizers (i.e., carbon) and carbide suppressers (i.e., silicon and aluminum) to retain carbon content within the austenite phase. The addition of nickel and manganese are also common alloying elements in fully austenitic TRIP steels. The processing temperature history of TRIP steel will be dependent on the desired volume fraction of ferrite and retained austenite. Figure 11 presents a typical temperature process control and the steps are summarized as follows:

Step 1: Heat up the steel and hold above eutectoid temperature for fully austenitic microstructure. If some ferrite is desired, a temperature between ferrite start (AC3) and eutectoid (AC1) temperature can be used.

Step 2: Rapidly cool to an intermediate temperature above the Martensite-Start temperature (Ms) to avoid the formation of unwanted phases.

Step 3: Continuously vary the cooling to RT to partially transform some austenite into bainite to achieve the desired composition.
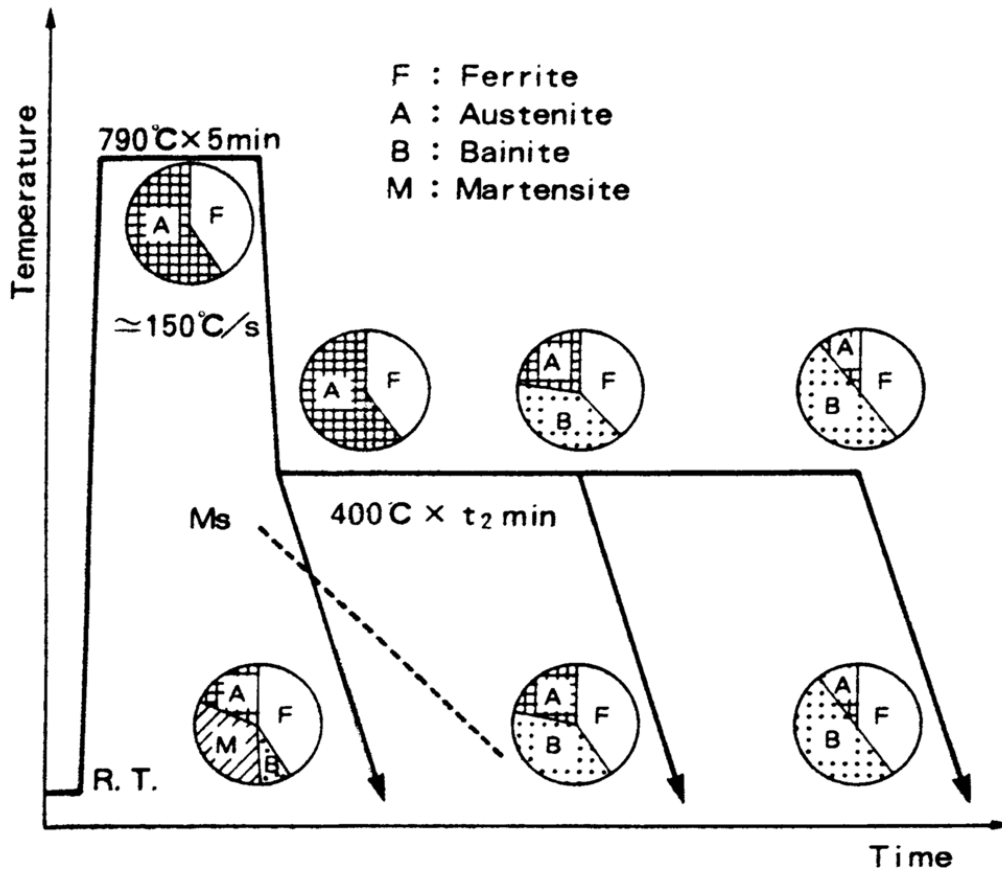
Figure 11: TRIP steel processing temperature history, resulting in ferrite, bainite, retained austenite and martensite [70]

2.2.1 Thermodynamics of Transformation Induced Plasticity

The underlying driving force of martensite transformation is a thermodynamics consideration. Evaluating phase composition from an energy standpoint, the differentiation of various phases is due to the assumption of the lowest energy state of the material. The energy level of various phases changes with temperature. When a temperature threshold, T_0, is reached, the stability of one phase becomes more favourable; however, this is usually not enough to cause transformation. Some form of energy input, $\Delta G^{\alpha' \to \gamma}$, is necessary to trigger transformation, commonly seen as undercooling to martensite start temperature M_s, or superheating to austenizing temperature, A_s, as seen in Figure 12.
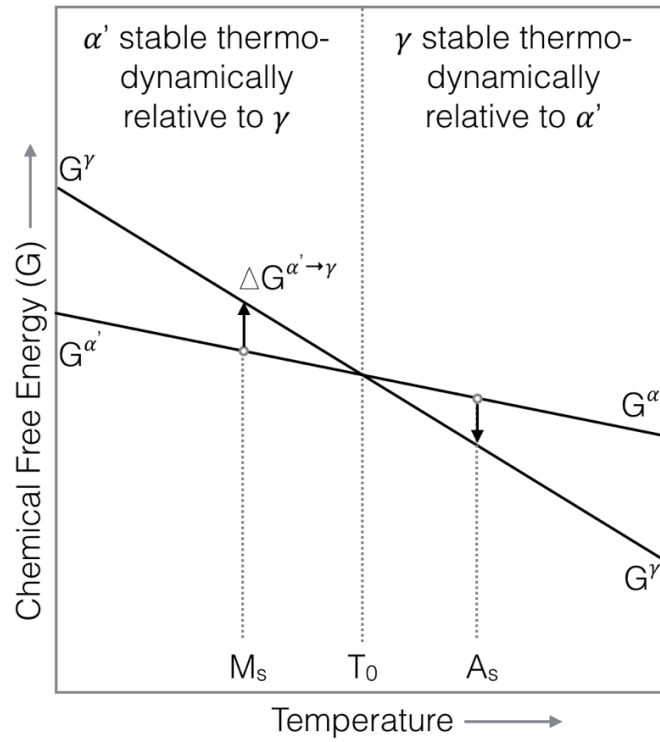
Figure 12: Chemical free energy vs temperature of γ and α' phases

Kaufman and Cohen (1958) [71] developed a thermodynamic model for martensite transformation in steels of varying chemical composition and a large range of temperatures. Chemical driving force equations were summarized from an extensive database of experimental works. The model presents, $\Delta G^{\alpha' \to \gamma}$, a difference in free energy between, G^{γ}, free energy of austenite and, $G^{\alpha'}$, free energy of martensite, often referred to as the stability of austenite, all of which varies with temperature. Tabulated values for various alloying elements in iron-alloy binary systems are presented in the paper, which can be summed together with respect to their weight percentage for an iron-alloy.

$$G^{\gamma} - G^{\alpha'} = \Delta G^{\alpha' \to \gamma} \qquad (\quad 2.1 \quad)$$

Perlade, Bouaziz and Furnemont (2003) [72], used an energy based model similar to that of *Kaufman and Cohen* [71]

$$\Delta G^{\alpha' \to \gamma} = \Delta G^{\sigma=0} + \frac{\partial \Delta G}{\partial \sigma} \sigma_{\gamma} \qquad (\quad 2.2 \quad)$$

14

where, $\Delta G^{\alpha' \to \gamma}$, transformation driving force is split into, $\Delta G^{\sigma=0}$, chemical and, $\frac{\partial \Delta G}{\partial \sigma}\sigma_\gamma$, mechanical contributions. They incorporated the effects of grain size into the model and were successful in capturing the martensite evolution trends during deformation. The physical phenomenon of latent heat of transformation is caused by, $\Delta G^{\alpha' \to \gamma}$, energy difference released during transformation. The latent heat of transformation releases a substantial amount of energy that contributes to local heating of the transformed region. *Rusinek and Klepaczko* (2009) experimentally showed a temperature rise of more than 100°C in quasi-static tensile tests of TRIP 800 steels, due to both plastic work and latent heat of transformation [73].

It is well known through the experimental work of *Angel* [34] that AISI 304 stainless steel (which is a TRIP steel) is very sensitive to temperature. At 22°C the generated volume fraction of martensite is nearly half of the same experiment conducted at 0°C. At a temperature of 50°C, the TRIP phenomenon is nearly eliminated. *Olson and Cohen* theorized that chemical driving force and stacking fault energy plays a critical role in understanding this difference [26].

Stacking fault energy (SFE) is a thermodynamic calculation of surface [74] [75] and volume free energy [76]. *Lecroisey and Pineau* [77] showed that the SFE of a material could be modified by chemical composition and temperature. Preference to accommodate deformation through TRIP instead of other deformation mechanisms is studied and related back to stacking fault energy (SFE). Shockley partial dislocations formed on low SFE FCC phase introduces embryos for martensite and sites for twinning [58] [78] [79]. Increasing stacking faults offer potential initiation points for dislocation slip and therefore becomes more favourable deformation mechanism as SFE increases.

2.2.2   *Mechanics of Transformation Induced Plasticity*

The nature of TRIP takes place when metastable retained austenite transforms to martensite under deformation. This transformation at the lattice level distorts the FCC structure of austenite into a BCC structure of martensite through a shear mechanism and is at the origin of the crystallographic theories of martensite transformation.

2.2.2.1 Bain and Dunkirk Orientation for Martensite Formation

Bain and Dunkirk [80] proposed a distortion that allows an FCC lattice to be transformed into a BCC lattice through an intermediate BCT lattice. Figure 13 presents two FCC base cells that are side by side with the BCT cell highlighted in between. Although one variant of martensite is presented, *Wechsler et al.* [81] have shown that up to 24 unique possible variants of martensite could develop within the parent phase. *Patel and Cohen* [82] incepted the idea of a preferred martensite variant formation due to a maximum mechanical driving force. This concept of preferred martensite variants was later reinforced by *Magee* [83] for preferred variants in iron-based alloys.
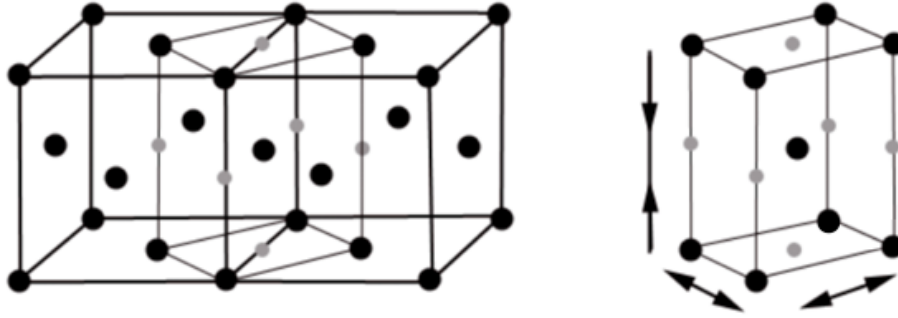
Figure 13: Bain distortion - FCC to BCT to BCC transformation.

By choosing the ½ $[110]\gamma$, ½ $[\bar{1}10]\gamma$ and $[001]\gamma$ directions as new reference frame, a BCC lattice is achieved by expanding the first two vectors by 12.6% and contracting the third by 20.3%. Depending on the material and the lattice parameters, the volume increases by 1%-4% when transformation takes place. The shape change necessary to accommodate martensite transformation is an invariant plane strain on a plane with a unit normal $(\vec{p} : \gamma^*) = (p_1 \; p_2 \; p_3)$, and a displacement in the unit direction $[\gamma : \vec{d}] = [d_1 \; d_2 \; d_3]$ of magnitude η. The terms γ and γ^* define the real and reciprocal bases of the austenite [84] [85]. The deformation can be represented by a matrix P for austenite.

$$P = \begin{bmatrix} 1 + \eta d_1 p_1 & \eta d_1 p_2 & \eta d_1 p_3 \\ \eta d_2 p_1 & 1 + \eta d_2 p_2 & \eta d_2 p_3 \\ \eta d_3 p_1 & \eta d_3 p_2 & 1 + \eta d_3 p_3 \end{bmatrix} \qquad (\quad \textbf{2.3} \quad)$$

16

2.2.2.2 Habit Planes and Fault Bands for Martensite Formation

In the context of this thesis, habit planes are the planes of a crystal that are the product of transformation [86]. Habit planes were first determined in the 1930s from optical microscopy on martensite plates that formed in monocrystalline austenite. *Scheil* [87] proposed that shear stress on the habit planes is the mechanism that activated martensite transformation in austenite.

Table 1: FCC fault band systems

α	Fault band systems	α	Fault band systems	α	Fault band systems
1	$[112] \otimes (11\bar{1})$	5	$[121] \otimes (1\bar{1}1)$	9	$[211] \otimes (\bar{1}11)$
2	$[1\bar{1}2] \otimes (1\bar{1}\bar{1})$	6	$[1\bar{2}1] \otimes (111)$	10	$[2\bar{1}1] \otimes (11\bar{1})$
3	$[11\bar{2}] \otimes (111)$	7	$[12\bar{1}] \otimes (1\bar{1}\bar{1})$	11	$[21\bar{1}] \otimes (1\bar{1}1)$
4	$[1\bar{1}\bar{2}] \otimes (1\bar{1}1)$	8	$[1\bar{2}\bar{1}] \otimes (11\bar{1})$	12	$[2\bar{1}\bar{1}] \otimes (111)$

A shear dislocation on the habit plane in the [111] direction is called fault bands. The FCC crystal has a total of 12 fault band systems, which are summarized in Table 1. The intersection of fault bands from different habit planes creates a highly favorable site for the formation of martensite. The intersection line of the two shear or glide bands is a location of very high strain concentration that helps to distort the 60° of the $(110)_\gamma$ plane (Figure 14 a). and b).) into the 70.5° of the $(111)_\alpha$ plane (Figure 14 c). and d).). *Borgers and Burgers* [88] visually represented the process needed to obtain BCC cell from an FCC lattice matrix shown in Figure 14.
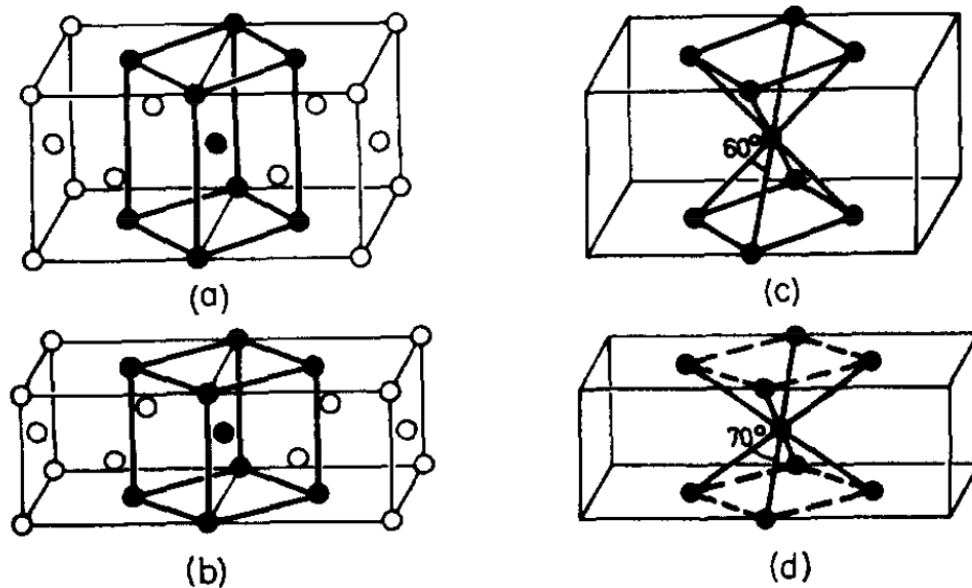
Figure 14: Bain correspondence between FCC and BCC lattice a). and c). FCC lattice with BCT cell in heavy lines. b). and d). compressed FCC lattice with BCC cell in heavy lines.

2.2.2.3 Orientation Relationship Due to Martensite Transformation

Understanding the crystal lattice relationship between austenite and martensite is an important and necessary component in accurately modeling the micromechanics of martensite transformation. Martensite transformation follows a rigid nature resulting in a fixed orientation relationship (OR) with respect to the parent γ-phase through a rotation. A significant effort has been made through the years to understand, measure and develop models to capture this rotation. Through the study of OR, experimental techniques have been developed to identify between α-ferrite and α'-martensite by analyzing orientation of nearby parent γ-austenite phase [89]. *Bain and Dunkirk* [80] first proposed a model to capture the OR of martensite. However, when compared with measurements from X-ray diffraction, the proposed OR model deviated by more than 10° from the experimental measurements. In the 1930s, with the use of X-ray diffraction, researchers have experimentally determined several additional ORs such as *Kurdjumov-Sachs* [89] and *Nishiyama-Wassermann* [90] [91]. Using transmission electron microscopy (TEM) diffraction in the 1950s, ORs such as *Greninger-Troiano* [92] and *Pitsch* [93] are observed. More recently *Miyamoto et al*. [94] determined a precise average OR from Electron Back Scatter Diffraction (EBSD) measurements. Table 2 presents a summary of these relationships.

Table 2: Summary of orientation relationships observed in martensite

Orientation Relationship	Plane	Direction
Bain-Dunkirk [80]	$\{010\}\,\gamma \parallel \{010\}\,\alpha$	$<001>\gamma \parallel <101>\alpha$
Kurdjumov-Sachs [89]	$\{111\}\,\gamma \parallel \{110\}\,\alpha$	$<1\bar{1}0>\gamma \parallel <1\bar{1}1>\alpha$
Nishiyama-Wassermann [90] [91]	$\{111\}\,\gamma \parallel \{110\}\,\alpha$	$<0\bar{1}1>\gamma \parallel <001>\alpha$
Greninger-Troiano [92]	$\{111\}\,\gamma$ at 1°$\parallel \{110\}\,\alpha$	$<\bar{1}2\bar{1}>\gamma$ at 2°$\parallel [1\bar{1}0]\,\alpha$
Pitsch [93]:	$\{001\}\,\gamma \parallel \{\bar{1}01\}\,\alpha$,	$<110>\gamma \parallel <111>\alpha$

2.3 Constitutive Modeling of TRIP Steel

Constitutive modeling of TRIP steel can be separated into two sections: the elastic-plastic behaviour and martensite transformation. The successful coupling of these two concepts is the minimum requirement of a martensitic transformation induced plasticity model.

2.3.1 Elastic-Plastic Behaviour of TRIP Steel

Two major classifications of modeling the elastic-plastic behaviour of metals, such as TRIP steel, exist in literautre: phenomenological plasticity and crystal plasticity.

2.3.1.1 Phenomenological Plasticity

Phenomenological-based plasticity models are derived from fitting a mathematical function, called a yield function, to experimentally observed data. Yield functions can be selected based on desired their functionality and complexity These yield functions include: the simple quadratic isotropic *Von Mises* [95], quadratic anisotropic *Hill* (1948) [96], non-quadratic isotropic *Hosford* (1972) [97] and the *Barlat and co-workers* [98] [99] [100] [101]. Several common flow stress hardening models such as Power Law hardening [102], *Voce* [103] hardening law, *Cowper-Symonds* [104] rate sensitive model and the *Johnson-Cook* [105] rate sensitive and temperature sensitive model have been incorporated into phenomenological plastic to simulate TRIP steel [106] [107] [108]. The availability of various mathematical functions is capable of capturing the material behavioural trend, but they do not have to have a physical basis. Furthermore, limited phenomenological models are able to capture evolving micro-structural detail during deformation [109].

2.3.1.2 Crystal Plasticity

Another framework used to model TRIP steels is crystal plasticity, the underlying assumptions are that crystals permanently deform primarily due to the movement of atoms through dislocations. *Taylor* [44] explained this concept as shearing of different rows of atoms of a crystal, visually represented in Figure 15. These dislocations appear locally in small regions and continue to grow throughout the grains. Shear stress along the direction of the gliding plane of the dislocation, known as the resolved shear stress, supplies the driving force to cause dislocations to glide. Crystallographic slip is an anisotropic deformation where large dislocation occurs on certain planes (slip planes) in certain directions (slip directions). Dislocations usually occurs in the planes

and directions of the lattice cell with the maximum atomic density. However, this is not always true.
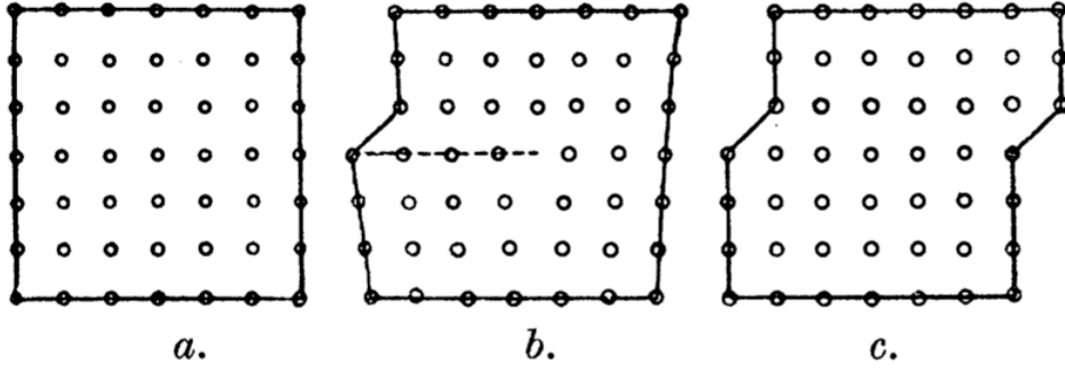
Figure 15: Dislocation slip along a row of atoms [44]

The mechanics of slip deformation is governed by the critical shear stress known as Schmid's Law [110], which serves as an initial microscopic yield criterion for single crystals. Schmid's Law states that in crystals of a given material under constant condition, extensive slip occurs when the resolved shear stress, $\tau^{(\alpha)}$, attains a critical value described as following

$$\tau^{(\alpha)} = P_{ij}^{(\alpha)}\sigma_{ij} = \tau_y^{(\alpha)}$$

(2.4)

where σ_{ij} is the stress state acting on a crystal, $\tau_y^{(\alpha)}$ is the yield strength of system α, and $P_{ij}^{(\alpha)}$, also known as the Schmid tensor is expressed as

$$P_{ij}^{(\alpha)} = \frac{1}{2}\left(s_i^{(\alpha)}m_j^{(\alpha)} + m_i^{(\alpha)}s_j^{(\alpha)}\right)$$

(2.5)

where $s_i^{(\alpha)}$ and $m_j^{(\alpha)}$ are components of slip direction vector $\boldsymbol{s}^{(\alpha)}$ and slip plane normal $\boldsymbol{m}^{(\alpha)}$, respectively of system α. From here, *Asaro and Needleman* [111] developed an elastic-plastic, rate dependent polycrystalline model accounting for deformation within the individual crystals by only crystallographic slip.

Relating the microscopic scale phenomena of single crystal plasticity to the macroscopic scale of polycrystal deformation requires a homogenization (or averaging) scheme. Assumptions are made on the stresses and strains in the polycrystal and polycrystal response that gives rise to different schemes, such as the Sachs' model, Taylor assumption, relaxed constraint model and self-

20

consistent schemes. These averaging schemes allow for efficient calculations of crystal plasticity through some assumptions.

2.3.1.2.1 Sach's Model

One of the earliest polycrystal models was the Sachs' model [112], where it was assumed that only one slip system operates in each grain. In this model, each grain is subjected to the same stress state, which is also the macroscopic stress and is taken to be a state of uniaxial tension. The model was refined by *Kochendorfer* [113] by the stipulation that each grain was subjected to the same stretch. *Bishop and Hill* [114] [115] pointed out individual grains having identical strain hardening amongst the polycrystal.

$$\frac{\sigma}{\tau} = \frac{d\gamma}{d\varepsilon} = M$$

(**2.6**)

where σ and $d\varepsilon$ are the axial stress in a grain and the macroscopic aggregate strain increment respectively, τ and $d\gamma$ are the shear strength and slip system shear strain increment, and M is the orientation factor tht depends only on geometry and in particular on the relationship between the loading axis and the crystal slip systems. The limitation of the Sachs' model, is that stress and strain continuity across grain boundary is violated. Equilibrium of the stresses cannot be established across grain boundaries and it, is not feasible to maintain compatibility amongst all grains.

2.3.1.2.2 Taylor's Model

In order to overcome the objections to Sachs' model, Taylor proposed another method of modeling polycrystals [116]. Taylor observed experimentally the micrograph of the cross section of a copper drawn wire and noticed that all the grains were elongated in the direction of extension and contracted in the two perpendicular directions. Taylor concluded that the strain field throughout the polycrystal was homogenous. The implication of this assumption is that individual grains are under the same deformation strain as the polycrystal. Stress is consistent within grains, however, can differ from other grains. As such, the Taylor assumption can have limitations in the case of multi-phase materials and non-homogeneous deformations [117]. However, this still remains an active point of contention in the scientific community [118] [119].

The Taylor assumption developed through the study of copper polycrystals under uniaxial tension can be summarized by two relationships:

a) Each grain in a polycrystal experiences the same strain as the polycrystal

$$\varepsilon_{grain} = \varepsilon_{aggre}$$

(2.7)

b) Macroscopic stress of a polycrystal is the average stresses of all single constituent crystals

$$\sigma_{aggre} = \sum_{grain=1}^{N} \frac{\sigma_{grain}}{N}$$

(2.8)

2.3.1.2.3 Relaxed Constraints Models

Honneff and Mecking [120] made modifications to the Taylor model, called a method of "relaxed constraints". Later, *Canova et al.* [121] extended this formulation to account for material texture effects. The fundamental assumption is that when grains reorient and take on distorted shapes, identified by large aspect ratios of the principal lengths, it is possible to partially relax the strict compatibility requirements imposed in the Taylor model. Non-uniform deformations are observed to occur at the grain boundaries, which accommodates the incompatibilities implied by the non-imposed strain components.

2.3.1.2.4 Self-Consistent Schemes

The self-consistent method proposed by *Kröner* [122], *Budiansky and Wu* [123], and *Hill* [124] is developed based on Eshelby's model [125]. This approach attempts to account for grain interaction by considering each grain to be an ellipsoidal inclusion embedded in an infinite homogeneous matrix. The overall moduli of the polycrystal is determined as an average of all grains. The constraint imposed by the matrix on a grain can be estimated with the aid of Eshelby's solution for an elastic inclusion.

2.3.1.2.5 Crystal Plasticity Finite Element Method (CPFEM)

Crystal Plasticity Finite Element Method (CPFEM) is first implemented as a generalized Taylor-type polycrystal constitutive model with a fully implicit time-integration scheme into a user defined material model in ABAQUS by *Kalidindi et al.* [126]. The goal of this model is to study the stress-strain response and the crystallographic texture evolution of polycrystalline FCC copper

during plane-strain forging. Subsequent development of the model into finite element was implemented. *Inal et al.* [127] used this model and studied forming of FCC polycrystalline sheets. *Rossiter et al.* [128] implemented the crystal plasticity scheme with an explicit time-integration scheme into a user defined material model in LS-DYNA. Developments of dislocation density based model [129] and mechanical twinning models [130] [131] have also been implemented into in CPFEM. *Cyr et al.* [132] incorporated the dependence of various material hardening parameters with respect to temperature into CPFEM to study aluminum alloys at elevated temperatures.

2.3.1.3   Slip Systems

In the FCC lattice structure, the symmetric structuring of the atoms results in twelve slip systems, {111}[110] family of slip systems was initially derived from studying pure Cu single crystals. The FCC lattice conforms to the close pack plane rule where all twelve slip systems are slipping on the highest atomic density planes. The available slip systems of the FCC crystal are summarized in Table 3.

Table 3: FCC slip systems

FCC Slip Systems	Plane	Direction
1		$[1\bar{1}0]$
2	$\{111\}$	$[10\bar{1}]$
3		$[0\bar{1}1]$
4		$[110]$
5	$\{\bar{1}11\}$	$[101]$
6		$[0\bar{1}1]$
7		$[110]$
8	$\{1\bar{1}1\}$	$[10\bar{1}]$
9		$[011]$
10		$[1\bar{1}0]$
11	$\{11\bar{1}\}$	$[101]$
12		$[011]$

The BCC lattice structure has a total of 48 slip systems, {110} [111], {211} [111] and {321} [111]. It is important to note that {110} [111] family of slip system has the highest atomic density plane. The concept of pencil glide is defined as any plane of the zone defined by the operating [111] slip direction might potentially act as slip plane. *Taylor and Elam* [133] initially observed that α-Fe single crystals deformed at RT with unique slip direction [111], however, there was not a single set of slip planes. Subsequently, *Gough* [134] applied alternating torsional tests

to a large α-Fe single crystal sample and showed {110} [111] is the only active slip system at low temperatures. However, upon an increase in temperature, a wavy dislocation line can be seen on the sample surface, indicating the activity of a high miller indices system. *Fahrenhorst and Schmid* [135] and *Sauerwald and Sossinka* [136] showed that slip plane families {110}, {211} and {321} could account for slip in α-Fe single crystal. The significance of these slip planes shows that for BCC materials slip does not necessarily occur only on the most densely packed planes. Dislocation glide in BCC lattice structure can occur on several slip plane families that do not have to be the most densely packed planes. Further developments show that the {321} [111] slip systems are only activated at elevated temperatures [137]. Therefore, only 24 slip systems of the BCC lattice structure are considered and summarized in Table 4.

Table 4: BCC slip systems

BCC Slip Systems	Plane	Direction	BCC Slip Systems	Plane	Direction
1	{110}	$[1\bar{1}1]$	13	{211}	$[\bar{1}11]$
2		$[1\bar{1}\bar{1}]$	14	{$\bar{2}$11}	$[111]$
3	{1$\bar{1}$0}	$[111]$	15	{2$\bar{1}$1}	$[\bar{1}\bar{1}1]$
4		$[11\bar{1}]$	16	{21$\bar{1}$}	$[\bar{1}1\bar{1}]$
5	{101}	$[11\bar{1}]$	17	{121}	$[1\bar{1}1]$
6		$[1\bar{1}\bar{1}]$	18	{$\bar{1}$21}	$[\bar{1}\bar{1}1]$
7	{10$\bar{1}$}	$[111]$	19	{1$\bar{2}$1}	$[111]$
8		$[1\bar{1}1]$	20	{12$\bar{1}$}	$[1\bar{1}\bar{1}]$
9	{011}	$[11\bar{1}]$	21	{112}	$[11\bar{1}]$
10		$[1\bar{1}1]$	22	{$\bar{1}$12}	$[\bar{1}1\bar{1}]$
11	{01$\bar{1}$}	$[111]$	23	{1$\bar{1}$2}	$[1\bar{1}\bar{1}]$
12		$[1\bar{1}\bar{1}]$	24	{11$\bar{2}$}	$[111]$

Materials consisting of both FCC and BCC microstructures will exhibit a combination of slip systems in their respective crystal lattice. Slip systems in such a material at RT are summarized in Table 5.

Table 5: FCC and BCC slip system at room temperature

Crystal Structure	Slip Planes	Slip Directions	# of Slip Systems
FCC	{111}	[110]	12
BCC	{110}	[111]	12
	{211}	[111]	12

* {321}[111] Not considered at RT [137]

2.3.2 Modeling of Martensite Transformation

Several experimental studies have been dedicated to studying stress induced martensite transformation from mechanical deformation. *Scheil et al*. [87] [138] and *Wassermann* [139] presented the first experimental studies in deformation induced martensite transformation in Fe-Ni alloy steel in the 1930s. *Porter and Rosenthal* (1959) [140] observed that martensitic transformation was proportional to the applied stress. *De Jong and Rathenau* in the same year [141] studied the irreversible length change of a loaded pure iron specimen during temperature cycling above and below $\gamma - \alpha$ transitional temperature. They also reported a linear relationship between the load stress and the irreversible elongation.

Greenwood and Johnson [142] and *Magee* [83] pioneered the first efforts to model and characterize the TRIP effect. Under control of temperature and constant deformation, the total strain during deformation induced martensite transformation was formulated as

$$\varepsilon = \varepsilon_e + \varepsilon_\theta + \varepsilon_c + \varepsilon_p \qquad (\quad 2.9 \quad)$$

where ε is the total strain, ε_e is the elastic strain, ε_θ is the thermal strain, ε_c is the transformational strain, and ε_p is the plastic strain. For elastic-plastic materials like iron based alloys, the transformational strain can be decomposed into a volumetric dilation of the product phase and an irreversible TRIP strain, ε^{TP}, such that

$$\varepsilon_c = \frac{\delta}{3} \xi I + \varepsilon^{TP} \qquad (\quad 2.10 \quad)$$

where ξ is the transformational volume change, I is the 2nd order identity tensor, δ is the volume of transformation, and the irreversible TRIP strain tensor is defined as

$$\varepsilon^{TP} = \frac{5}{6} \frac{\delta}{\sigma_y^0} \sigma \qquad (\quad 2.11 \quad)$$

with σ_y^0 being the initial yield in the parent phase. Later, *Leblond et al*. [143] [144] revisited the Magee mechanism assuming that the straining mechanism was negligible and the phases were ideally plastic. Through this study, a generalized model was proposed for all kinds of applied stresses in the case of ideal-plastic phases.

On a separate front, *Patel and Cohen* (1953) [82] noticed that variations in applied stress change the martensite transformation temperature in Fe-Ni and Fe-Ni-C alloys. Martensite transformation temperature is modified by an energy term, calculated from the applied stress on the potential habit plane of the parent phase. This energy term, U, is comprised of, $\tau\gamma_t$, the shear stress resolved along a potential habit plane times the transformation shear strain, and, $\sigma\varepsilon_t$, the normal stress resolved perpendicular to the habit plane times the normal component of the transformation strain.

$$U = \tau\gamma_t + \sigma\varepsilon_t \qquad (\quad 2.12 \quad)$$

Fischer (1990) [145] presented an analytical concept for the TRIP strain due to martensitic transformation in a specimen subjected to uniaxial stress state, and later for three-axial stress state [146]. *Berveiller and Fischer* [147] conducted a detailed mathematical treatment; however, their results seemed to overestimate the orientation effect. Further modeling development, particularly into phenomenological, micromechanics and fault band based transformation criteria for stress and strain induced TRIP effect, are described in detail.

2.3.2.1 Phenomenological Transformation Criteria

Multiple studies (i.e. *Venables* [148], *Manganon and Thomas* [149], *Lecroisey and Pineau* [77]) have identified intersections of shear-bands within austenite crystalline as the location for strain-induced martensite transformation. Using these experimental observations, *Olson and Cohen* [26] proposed a transformation model that related the volume fraction of shear band

nucleation sites to martensite phase transformation. They proposed that the volume fraction of shear band, f^{sb}, followed

$$f^{sb} = 1 - \exp\left(-\alpha\,\varepsilon_p\right)$$

(2.13)

where α is a temperature sensitive constant to describe the shear band generation rate (that is related to stacking fault energy and chemical driving force), and ε_p, is the plastic strain within the austenite crystalline. Assuming shear bands have a constant average volume, $\bar{v}^{sb}$, the number of shear bands per unit austenite volume

$$N_v^{sb} = f^{sb}/\bar{v}^{sb}$$

(2.14)

Thus, the number of shear bands increases (approximately) linearly with strain until saturation occurs. Next, the number of shear-band intersections per austenite unit volume, N_v^I, can be related to the number of shear bands using a Power Law formulation

$$N_v^I = K(N_v^{sb})^n$$

(2.15)

K and n can be obtained from quantitative stereology. The incremental increase in the number of martensitic embryos produced per unit austenite volume, $dN_v^{\alpha'}$, can be related to the incremental increase in the number of shear band intersections, dN_v^I, such that

$$dN_v^{\alpha'} = p\,dN_v^I$$

(2.16)

where, p, is the probability that the shear band intersection will generate a martensitic embryo. Finally, *Olson and Cohen* [26] propose that the volume fraction of martensite transformation, $f^{\alpha'}$, follows a similar saturation behavior law with respect to the volume fraction of shear bands

$$f^{\alpha'} = 1 - \exp\left(-\frac{\bar{v}^{\alpha'}\,p}{(\bar{v}^{sb})^n}\,K(f^{sb})^n\right)$$

(2.17)

where $\bar{v}^{\alpha'}$ is the average volume of martensite within an austenite crystalline.

Angel (1954) [34] experimentally showed that strain-induced transformation behavior of sheet AISI 304 stainless steel follows a curve representing a sigmoidal function. The importance of the sigmoidal function is that a Gaussian distribution can be used to describe the rate of transformation. *Olson and Cohen* (1975) [26] used this result to verify and explain their model.

Modeling the martensite transformation behavior using a parabolic behavior shown by *Gerberich et al.* [150], however, this method did not prove to be popular.

Stringfellow et al. [151] [152] extended the *Olson and Cohen* [26] model to include the influence of the stress triaxiality, Σ, on transformation driving force parameter, α, and the probability of shear band nucleation, $p(T, \Sigma)$. Subsequently, *Iwamoto and co-workers* [153] [154] [155] incorporated strain-rate sensitivity and higher-order thermal sensitivity, such that the transformation driving force parameter was cast as

$$\alpha = (\alpha_1 T^2 + \alpha_2 T + \alpha_3 - \alpha_4 \Sigma) \left[\frac{\dot{\varepsilon}_{(\gamma)}^{pslip}}{\dot{\varepsilon}_y} \right]^m \qquad (\quad \textbf{2.18} \quad)$$

where T is the temperature, m is the strain rate sensitivity exponent, $\alpha_1, \alpha_2, \alpha_3, \alpha_4$ are material parameters, $\dot{\varepsilon}_y$ is a reference strain rate and $\dot{\varepsilon}_{(\gamma)}^{pslip}$ is the strain rate of the austenite phase. Recently, *Kohar et al.* [156] implemented this phenomenological martensite transformation model into a commercial finite elements code LS-DYNA to study the effect of TRIP on axial crush components.

2.3.2.2   Micromechanical Transformation Criteria

A series of literature has been developed from a micromechanical perspective to model the transformation phenomenon of strain-induced martensite. *Cherkaoui et al.* [157] [158] modeled the TRIP effect in austenite single crystals with a coupled thermodynamics and micromechanics model based on the *Greenwood and Johnson* [142] and *Magee* [83] of transformation. In the current configuration shown in Figure 16, a single crystal of austenite representative volume element (RVE) with volume, V, temperature, T, and uniform stress, Σ.
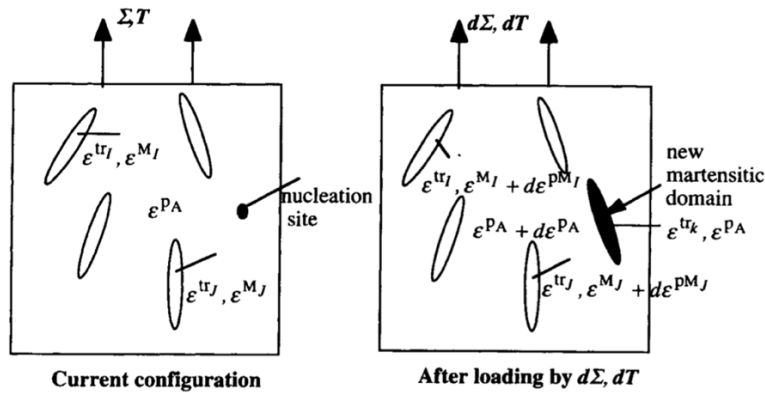
Figure 16: Schematic representation of different microscale mechanisms associated with the RVE [157]

Upon some thermo-mechanical loading, dT, and $d\Sigma$, martensite nucleation and growth of the RVE is modeled by the volume fraction rate of martensite, expressed as

$$\dot{f}^I = \frac{1}{V} \int_{S^I} w_\alpha^I \, n_\alpha^I \, dS^I \tag{2.19}$$

where $\dot{f}^I$ is the volume fraction rate, I denoting N of 24 crystallographically possible martensite variants, V, volume, S^I, boundaries, w_α^I, the velocity of the boundary and n_α^I are components of the unit normal vector of the boundary. The total volume of martensite phase, V^M is the sum of all the individual variants, V^I, of martensite

$$V^M = \sum_{I=1}^{N} V^I \tag{2.20}$$

and the volume of austenite V^A is the remainder.

$$V^A = V - V^M \tag{2.21}$$

Each variant is characterized by a habit plane normal, $\vec{N}$, direction of transformation, $\vec{M}$, and the amplitude, g, of the transformation strain considered as a material constant.

$$\varepsilon_{ij}^{tr\,I} = g \, R_{ij}^I = \frac{1}{2} g \left(M_i^I N_j^I + M_j^I N_i^I \right) \tag{2.22}$$

Total strain due to martensitic transformation is the sum of all variants of martensite.

$$\varepsilon^{tr}(r) = \sum_{I=1}^{N} \varepsilon_{ij}^{tr\,I} \theta^I(r) \tag{2.23}$$

where $\theta^I(r)$ are the Heaviside step functions for the different transformed domain defined as

$$\theta^I(r) = \begin{cases} 0 \ \ if \ r \ \notin \ V^I \\ 1 \ \ if \ r \ \in \ V^I \end{cases} \tag{2.24}$$

The mechanical driving force for martensite transformation is described by, $\bar{\sigma}^A \cdot \tilde{\varepsilon}^{tr}$.

$$\bar{\sigma}^A \cdot \tilde{\varepsilon}^{tr} = R\sqrt{3J_2}\left[1 + k\frac{J_3}{J_2^{3/2}} \right] + \frac{1}{3}\frac{\Delta V}{V} I_1 \tag{2.25}$$

where I_1 is the first invariant of the austenite stress tensor, J_2 and J_3 are the second and third invariants of the deviatoric stress tensor of austenite respectively, and $(\Delta V/V)$ is the volume change during the martensitic transformation. R, material parameter corresponding to the maximum transformation strain obtained during a loading sequence, and κ is the transformation stress state sensitivity parameter.

Thermodynamic driving forces acting on the moving boundary point between the product and the parent phase has been derived from the Eshelby's work on the energy momentum tensor. As such, the total driving force equation was assumed to follow

$$F = \bar{\sigma}^A \cdot \tilde{\varepsilon}^{tr} - B(T - T^0) - \kappa \qquad (\textbf{2.26})$$

where, B, is a material constant, T^0, is the equilibrium temperature, and κ, is the self-internal stress contribution. When the driving force exceeds the critical driving force, transformation of the domain is allowed. The critical driving force is comprised of three contributions: macroscopic contribution, F_o^c, plastic deformation and thermodynamics contribution, F_p^c, and geometric restrictions, F_f^c, such that

$$F^c = F_o^c + F_p^c + F_f^c. \qquad (\textbf{2.27})$$

Cherkaoui et al. [159] extended the model to include more explicit relations in the case of simple shear loading condition that encourages the transformation of martensite. *Kubler et al.* [160] later, incorporated a new texture evolution regime where the lattice spin of austenite grains is related with the slip rate on the slip systems of the two phases, the evolution of martensite volume fraction and the overall rotation rate of the grains. *Serri and Cherkaoui* [161] implemented the transformation framework into a commercial finite element code ABAQUS/EXPLICIT to simulate the behavior of unstable TRIP steel sheets under forming conditions.

Using advanced experimental techniques, *Choi et al.* [162] created a finite element simulation of an RVE model of commercial TRIP 800 steel that was created from a scanning electron microscopy (SEM) image. Figure 17 presents a schematic of the experimental SEM and reconstructed finite element model with individual phases. Individual phase material parameters were obtained via synchrotron-based in situ high-energy X-ray diffraction (HEXRD) experiments.

Using a similar transformation criterion as *Cherkauoi and co-workers*, *Choi et al.* [162] simulated martensite evolution and its influence on ductility during large deformation.
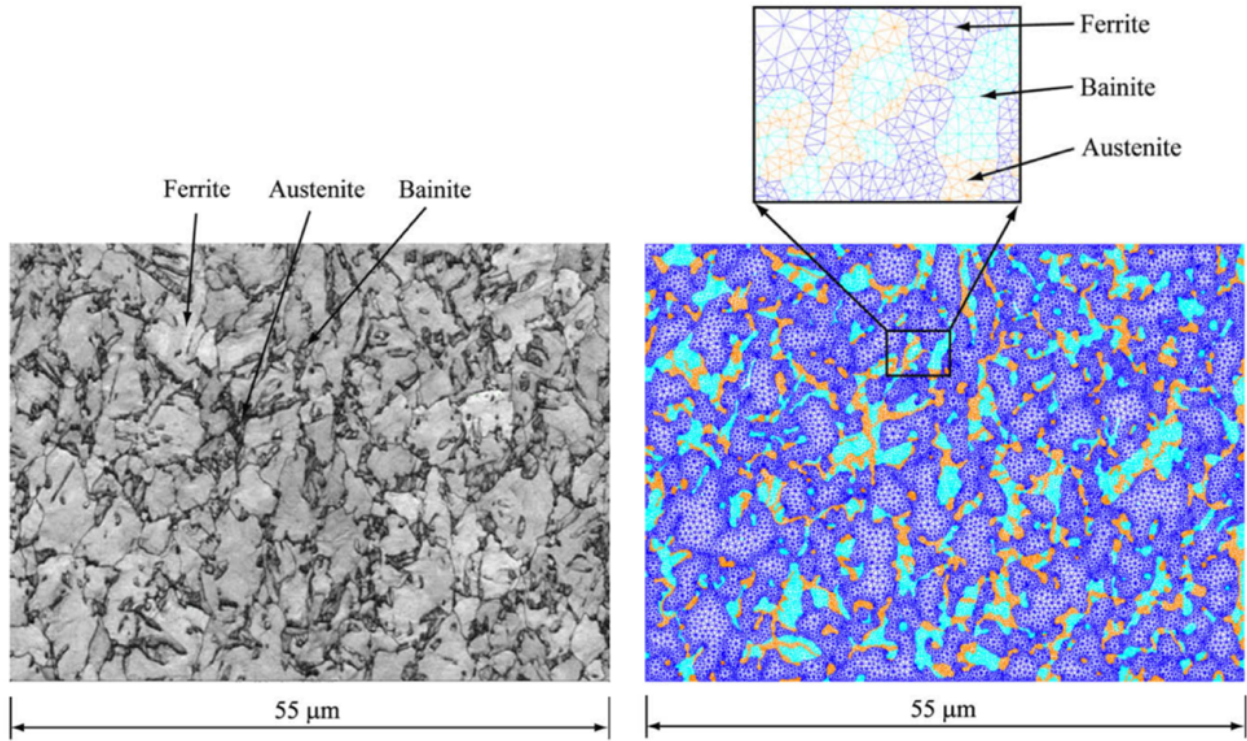
Figure 17: Scanning electron microscope image of TRIP 800 steel and the corresponding finite elements mesh [162]

2.3.2.3 Fault Band Transformation Criteria

Kim et al. [163] incorporated the fault band system approach into crystal plasticity finite element method (CPFEM) with an evolving interaction energy based transformation criterion. After every increment, a transformation threshold term, Γ^{th}, is calculated for every austenite crystal defined by

$$\Gamma^{th} = C^{th1} + C^{th2} \cdot \Gamma^{acc} \qquad\qquad (\quad\textbf{2.28}\quad)$$

where C^{th1} and C^{th2} are transformation evolution parameters, and Γ^{acc} is the accumulated shear resolved on the habit planes of an austenite crystal. The modification of the transformation threshold based on accumulated shear is credited due to the accumulation of stacking faults, increasing the barrier to transformation. The accumulated shear on the habit planes is the integration of the shear rate over time

$$\Gamma^{acc} = \int_0^t \left(\sum_\alpha \dot{\gamma}_f^\alpha \right) dt \qquad (\quad \textbf{2.29} \quad)$$

When the energy term, U_i^m, of intersecting fault bands exceed that of the $\gamma - to - \alpha'$ transformation threshold, transformation occurs. U_i^m is calculated with the normal stress, $\boldsymbol{\sigma_N}$, dilatational strain, $\boldsymbol{\delta}$, shear stress on the invariant plane, $\boldsymbol{\tau}$, and $\boldsymbol{s}$, the shear strain, such that

$$U_i^m = \boldsymbol{\sigma_N} \cdot \boldsymbol{\delta} + \boldsymbol{\tau} \cdot \boldsymbol{s} \qquad (\quad \textbf{2.30} \quad)$$

The fault band system is fixed to the crystal orientation, evolving with crystal texture under deformation, therefore capturing the dependence of transformation with respect to texture.

2.3.2.4   Summary of Transformation Criterion

Table 6 provides a summary of the models for martensite transformation as discussed in the previous sections. Although the phenomenological and micromechanics models can be applied to a crystal plasticity model, these transformation rules do not directly take into account microstructural effects in a manner as outline in the fault band model. However, the fault band model cannot be applied to a phenomenological model and requires a crystal plasticity constitutive model.

Table 6: Summary of transformation criterions

Transformation Criteria	Advantages	Disadvantages
Phenomenological Model *Iwamoto and Tsuta* [153] [154]	• Simplest formulation • Can be applied to phenomenological/crystal plasticity constitutive model	• Transformation rule does not account for microscale details
Micromechanics Model *Serri and Cherkaoui* [161]	• Thermo-mechanically coupled • Formulated from Eshelby homogenization theory • Can be applied to phenomenological/crystal plasticity constitutive model	• Transformation rule does not account for microscale details
Fault Band Model *Kim et al.* [163]	• Physics based model • Utilizes microstructure inputs • Texture evolution effects	• Computationally expensive - Requires calculations on a slip system level through crystal plasticity

2.4 Forming Limits for Sheet Metals

One method of evaluating the formability of sheet metals for use in automotive structures is the forming limit diagram (FLD). Keeler and Backofen [164] [165] and Goodwin [166] introduced the concept of the FLD to describe the onset of localization of sheet metal. The Considere Criterion, which is when the strength increase due to hardening, $\frac{d\sigma}{d\varepsilon}$, is equal to the stress due to thinning, σ, is the criterion used for necking will occur, such that

$$\frac{d\sigma}{d\varepsilon} = \sigma \qquad (\quad 2.31 \quad)$$

A forming limit curve (FLC) is a series of points that correspond to the limit strain of the material for proportional stretching that ranges between uniaxial and biaxial tension. The proportional stretching ratio, ρ, is defined as

$$\rho = \frac{D_{22}}{D_{11}} = \frac{\dot{\varepsilon}_{22}}{\dot{\varepsilon}_{11}}, \quad -0.5 \leq \rho \leq 1.0 \qquad (\quad 2.32 \quad)$$

where D_{ij} is the symmetric part of the velocity gradient (that are equal to logarithmic strain rates $\dot{\varepsilon}_{ij}$) and $\rho = -0.5$ and $\rho = 1.0$ correspond to uniaxial and equibiaxial stretching respectively.
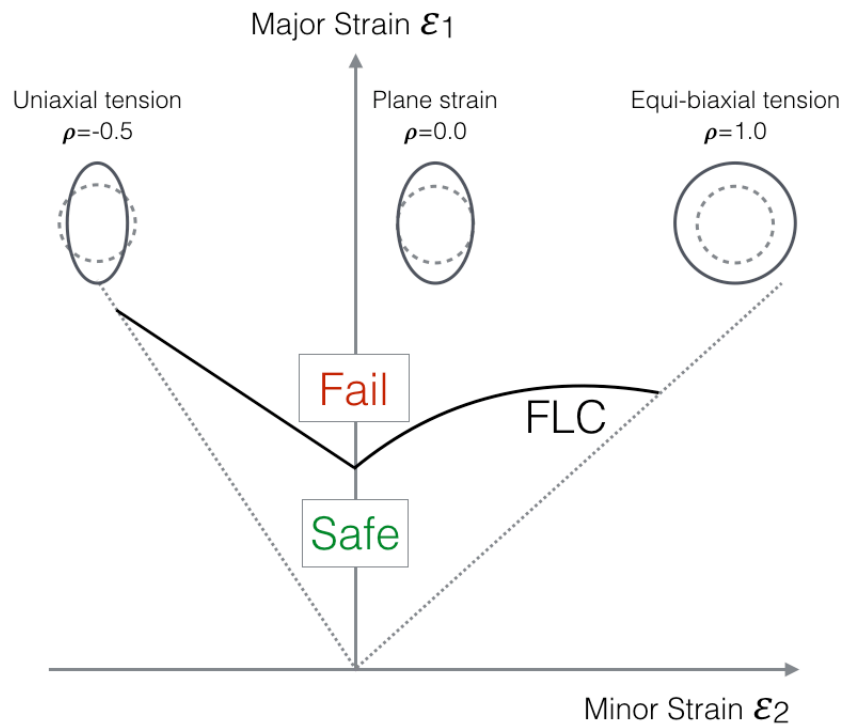
Figure 18: Sample FLD showing uniaxial tension, plane strain, and equi-biaxial tension

33
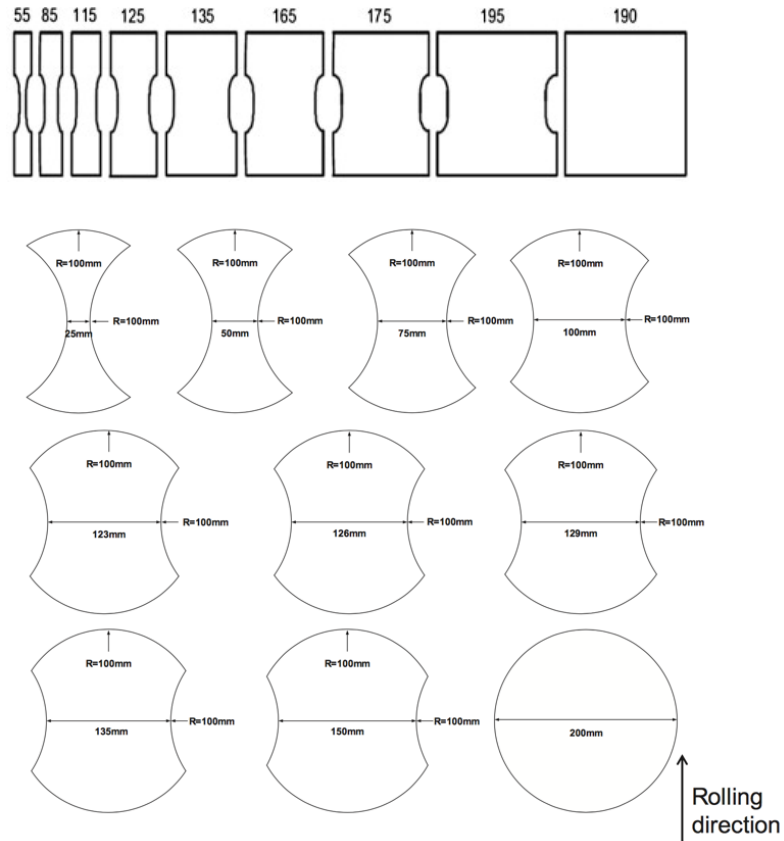
Figure 19: Specimen dimensions for FLD generation [167] [168]

Figure 18 presents the summation of the major and minor strains that form the FLC line of an FLD. Forming limit diagrams can be determined by experimentally deforming various blank/punch configurations and friction conditions to produce a range of strain states and strain paths that mimic industrial settings [169] [170]. Common experimental methods to evaluate forming limits of sheet include: *Nakazima* [171], *Marciniak* [172], and Erichsen test [173]. These testing methods use a punch to deform sheets of various dimensions and notch combinations to vary the strain path. Figure 19 presents some common sheet dimensions and combinations required for this experimental program. The strain paths obtained with this method is neither proportional nor simple. Extensive experimental forming limit work has been conducted for steels exhibiting martensite transformation [174] [175] [176] [177] [178] [179] [107]. *Talyan et al*. [180] presented a complete analysis of several austenitic stainless sheets of steel (Type 201, 301 and 304). They presented chemical compositions, stress-strain behaviors, Lankford coefficients, martensite evolution with respect to strain at different strain rates, temperature evolution and experimental FLD. Figure 20 presents a sample of their experimental results. They reported that formability of

34

these austenitic stainless steels was strongly dependent on the coupled phenomenon behaviour of martensite transformation with temperature.
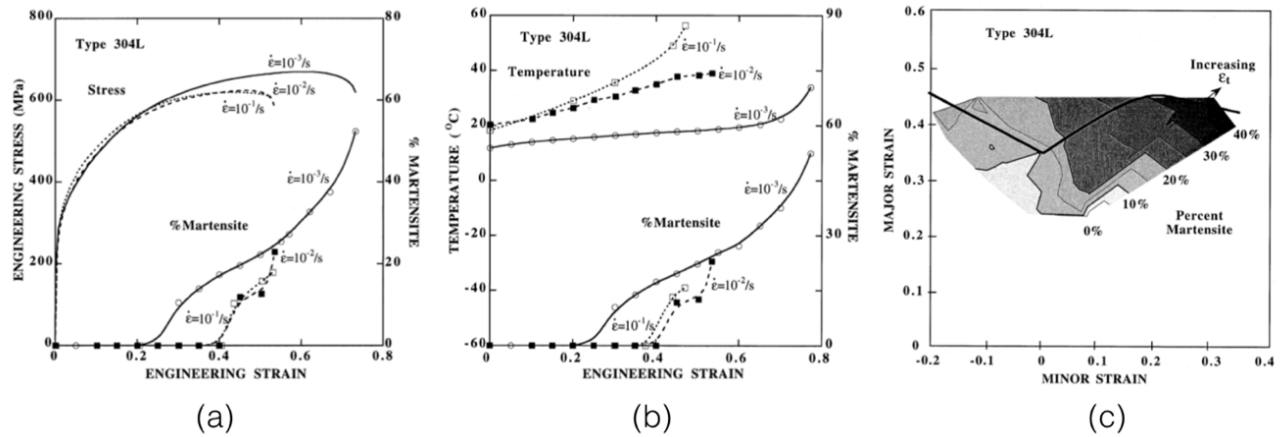
Figure 20: AISI 304L stainless steel experimental data (a) stress-strain and martensite volume fraction (b) temperature evolution and martensite volume fraction (c) FLD and martensite volume fraction [180]

2.4.1   Numerical Methods for Determining Forming Limits

Although FLDs can be generated through experimentation, they are often laborious tasks that require significant resources and care to obtain reliable results. As such, analytical and computational methods for evaluating formability is an attractive alternative to experimentation. *Swift* (1952) [181] first proposed a method for determining the onset of diffused necking in sheet metals assuming a homogenous sheet. He predicted the onset of diffused necking by developing an instability criterion based on the maximum load definition under proportional loading. He showed that the major limit strain in diffuse necking could be determined as

$$\varepsilon_1^{Limit} = \frac{2n(1 + \rho + \rho^2)}{(\rho + 1)(2\rho^2 - \rho + 2)}, \quad -0.5 \leq \rho \leq 1.0 \qquad (\quad \textbf{2.33} \quad)$$

where n corresponds to the hardening exponent of the sheet (assuming that the flow stress behavior followed a power-law hardening behavior). In the same year, *Hill* [182] developed a mathematical description of homogenous thin sheets explaining the relationship between the r value of the material and the angle between the through thickness direction for localized necking.

Several numerical approaches exist today for evaluating sheet metal formability, the *Marciniak and Kuczynski* (MK) [45] approach is simple yet effective. *Hutchinson and Neale*

(1978) [183] [184] [185] presented a series of works on sheet necking discussing the difference of deformation theory and flow theory methods for formability analysis with strain-rate and time dependence on the FLD. As such, the MK-approach, today, remains one of the most powerful and widely used methods for evaluating formability of sheet metals.

The MK-approach assumes a geometric or structural non-homogeneity (called an imperfection) that initiates and drives an asymptotic localization behavior for sheet metals. The fundamental assumption of the existence of imperfections in sheet metal from manufacturing and material inhomogeneity drives localization has been experimentally shown to mimic reality by *Azrin and Backofen* [186]. Under proportional stretching, the strain rate inside and outside of the imperfection is calculated from a constitutive model, while stress equilibrium is maintained across the imperfection. Through the use of a constitutive model, an MK-analysis can be readily extended to incorporate sophisticated deformation mechanisms that are observed in newly developed sheet metals, such as TRIP steel.

Since then, the MK analysis has received significant attention and expansion from researchers around the world to incorporate additional experimental phenomenon. *Stroen and Rice* [187] studied the effects of yield surface vertices on the FLD using the MK-approach. *Bassani et al.* [188] showed the effect of anisotropy in sheet metal forming limit analysis. *Lian et al.* [189] and *Dasappa et al.* [190] showed that the yield locus curvature greatly impacts the limit strains generated by the MK-approach.

2.4.2 *Crystal Plasticity Based Forming Limit Analysis*

The imperfection parameter is the basis of the MK analysis. However, even a slight intrinsic inhomogeneity in the load bearing capacity throughout a deforming sheet can lead to the unstable evolution of strain in the weaker regions and subsequently lead to localized necking. A significant source of inhomogeneity lies in the microstructure and texture of the material, which evolves during mechanical deformation.

Beginning with a series of *Bishop-Hill* [114, 115] yield surface calculations of polycrystals, *Bassani et al.* [188], *Barlat and co-workers* [191] [192] [193] [194] corresponded these various crystallographic textures to predict forming limits. In these preliminary works, the effect of elasticity and yield locus evolution, which is captured through crystal plasticity during

36

deformation, was not considered. Using an elastic-viscoplastic Taylor-type polycrystal plasticity model, *Tvergaard and Needleman* [195] calculated the forming limit strains for only equibiaxial and plane strain tension. *Zhou and Neale* [196] utilized a rate-dependent crystal plasticity formulation to predict FLDs for FCC annealed metal sheets using the MK-approach. Although their model incorporated the initial texture and texture evolution, elasticity was not considered, and the imperfection band was assumed to remain normal to the principal stretch direction. *Qiu et al.* [197] considered the effects of elasticity but did not consider the band angle. *Wu et al.* [198] further developed upon the rate-dependent polycrystal model to incorporate the effect of various imperfection band angles. They analyzed the effects of imperfection intensity, orientation, distribution of grain orientations, crystal elasticity, strain rate sensitivity, single slip hardening and latent hardening on FLD predictions. *Inal et al.* [118] used the elastic-viscoplastic Taylor type polycrystal model to compare the differences in forming limits of FCC and BCC slip systems. In their work, FCC and BCC aggregates with identical initial textures were calibrated to have nearly identical to uniaxial tension (through the material constants). Afterwards, an MK analysis was performed to generate FLD for each slip system configuration, and the differences were compared. Their results showed that BCC slip systems show a significant increase in formability over FCC slip systems in the biaxial stretching region. Yield potentials of both materials were calculated and compared, reinforcing the influence of yield locus shapes for the two types of polycrystals. Recently, *Cyr et al.* [199] formulated a thermo-elasto-viscoplastic crystal plasticity MK-analysis to simulate the elevated temperature (up to 300C) FLD of aluminum alloys AA3003 and AA5754. This framework varies the material hardening parameters of crystal plasticity and the material imperfection parameter with temperature, which is subsequently used to simulate the FLD. Their simulated FLD showed reasonable agreement with experimental data.

2.4.3   Formability Analysis of TRIP-assisted Steel

Attempts have been made to simulate the formability of TRIP-assisted steels. *Tourki et al.* [200] experimentally measured the volume fraction of martensite through X-Ray dispersive energy coupled with SEM analysis for temperatures of $-196°\,C$ to $22°\,C$. They presented temperature dependent model for the volume fraction of martensite, $f_{\alpha'}$, with respect to strain, such that

$$f_{\alpha'} = 1 - exp(-\beta(T)[1 - exp(-\alpha(T)\varepsilon)]^{4.5})$$

(**2.34**)

where $\beta(T)$ and $\alpha(T)$ are temperature dependent parameters. The authors went on to predict the FLD of AISI 304 stainless steel using the MK analysis. The predicted FLD showed good agreement, however, the resultant martensite volume fraction data was not confirmed to simultaneously match experiments. *Campos et al.* [201] performed a MK analysis to predict the FLD of AISI 304 stainless steel. The simple anisotropic phenomenological Hill (1948) [96] yield function without martensite transformation was used to perform their analysis. The predicted FLD showed good agreement with a limited set of experimental data. In a similar manner, *Panich et al.* [107] simulated the formability of TRIP 780 steel with the MK-approach, the Yld2000 phenomenological yield function [99] and without a model for martensite transformation. They showed significant deviations between predicted and experimentally measured FLDs. *Makkouk et al.* [202] simulated AISI 304 stainless steel behavior using a phenomenological plasticity model with the martensite transformation kinetics model developed by *Iwamoto et al.* [155] [153] [154]. They performed an MK analysis to simulate the FLD and compared with experimental measurements data obtained via the Marciniak punch test.

2.5   Deficiency in Literature

Strain induced martensitic transformation in steel has been studied extensively. Modeling TRIP steel is challenging because it requires the integration of physics, material science and numerical modeling to be successful. However, despite the vast amount of experimental and theoretical works, there still exists a need for a combination of accurate elastic-plastic behavior with the TRIP effect for use in a constitutive model.

Beyond this need, little knowledge is available in the literature that contributes to the understanding of TRIP steel formability. The MK method offers an efficient framework for the calculation of FLDs. Yet, as of late, many formability analyses using the MK approach do not account for the physics of martensite transformation or martensite transformation in general, let alone the differences due to the microstructural phenomenon. *Connolly et al.* [203] recently investigated the effects of martensite transformation on the formability of TRIP 800 steel. However, their study used a phenomenological constitutive model. Even with all the advancements in computational performance and experimentation, there still exists a need for a framework to quickly and efficiently simulate forming limits diagrams that accounts for the micromechanics of TRIP-assisted steels.

3   SCOPE AND RESEARCH OBJECTIVE

The scope of this thesis is to develop a crystal plasticity constitutive model that incorporates martensitic transformation to simulate FLDs. In order to employ a micromechanics based transformation criterion, a rate-dependent elastic viscoplastic polycrystal framework will be developed that incorporates the individual slip systems of FCC and BCC crystals, for a duplex stainless TRIP assisted steel. The proposed model will be calibrated using the initial texture supplied by *Kim et al.* [163], experimentally measured martensite volume fractions and stress-strain response during uniaxial tension for the selected material. The calibrated model will then be analyzed under different strain paths. Furthermore, the proposed model will be incorporated into the MK framework to explore the formability aspect of a TRIP-assisted steel and the effects of transformation control parameters. Thus, the main objectives of the current research are to:

1. Couple an elastic-viscoplastic crystal plasticity model to a micromechanical dependent transformation model to capture the effects of martensite transformation.
2. Calibrate the crystal plasticity model using DSS initial texture, along with volume fraction evolution and uniaxial stress-strain response.
3. Discuss results of multi-axial loading as well as the microstructure evolution.
4. Identify favorable austenite crystal orientations that promote transformation.
5. Simulate FLDs using the calibrated material parameters in an MK framework.
6. Evaluate the sensitivity of martensite transformation parameters on formability.

3.1   *Limitations of Modeling Formulation Used in Current Study*

Several assumptions are made during the formulation of the model framework. From a material science perspective, ferrite and martensite are assumed to be of a BCC structure [63], while austenite is assumed to be a FCC structure. The BCC crystalline is assumed to have 24 slip systems active and that slip system activity is independent of temperature. This naturally imposes a limitation where additional slip systems are active at elevated temperatures [137]. The orientation relationship between parent phase and transformed martensite is assumed to follow a single variant of the Bain relationship.

From a modeling perspective, the framework uses a Taylor-type polycrystal plasticity model for simulating an RVE. The transformation criterion is inspired by that of *Kim et al.* [163], however it has been modified as a stress based transformation criterion to suit the nature of a Taylor-type model. The transformation from austenite to martensite is assumed to occur instantaneously, and that accumulated slip during austenite deformation has no effect on martensite deformation. From an experimental data perspective, the microstructure, stress strain curve and the volume fraction data are provided by *Kim et al.* [163]. It is also assumed that the experiments were carried out in isothermal conditions, such that little to no heat generation from plastic work or latent heating occurs; therefore, thermal effects are not considered.

4 CONSTITUTIVE MODELING

In this thesis, the crystal plasticity constitutive formulation developed by *Asaro and Needleman* [111] and used by *Inal et al*. [127] is employed with power law hardening to model the polycrystalline behaviour of distinct steel microstructures.

4.1 Single Crystal Plasticity Model

The deformation gradient tensor, $\boldsymbol{F}$, is defined as

$$F_{ij} = \frac{dx_i}{dX_j}$$

(4.1)

where x_i is the current material point location in space and X_j is the initial material point location in space. Deformation of the crystal are caused by crystallographic slip, through dislocation motion on active slip systems, and elastic lattice distortion and rigid body rotations of the lattice. As such these deformations can be obtained through polar decomposition of the deformation gradient

$$\boldsymbol{F} = \boldsymbol{F}^* \boldsymbol{F}^P$$

(4.2)

where $\boldsymbol{F}^P$, accounts for crystallographic slip and $\boldsymbol{F}^*$, accounts for rigid body rotations and elastic deformation. The graphical representation of the total deformation gradient decomposition is shown in Figure 21.
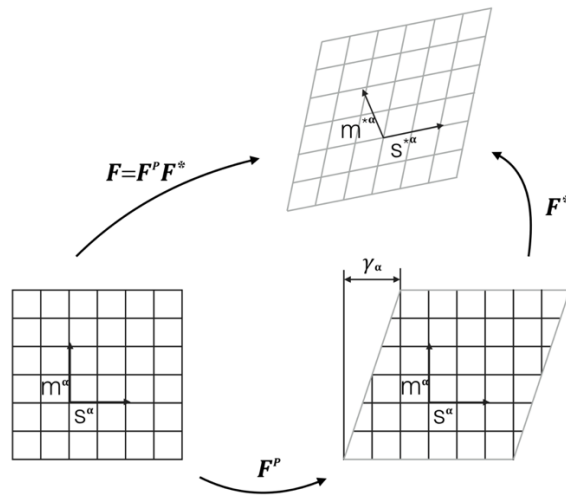
Figure 21: Decomposition of the total deformation tensor F

The vectors $s^{(\alpha)}$ and $m^{(\alpha)}$ are regarded as lattice vectors such that they stretch and rotate by

$$s^{*\,(\alpha)} = F^* s^{(\alpha)}, \qquad m^{*\,(\alpha)} = m^{(\alpha)} F^{*-1} \qquad (\ \ 4.3\ \ )$$

The spatial gradient of velocity L is written as

$$L = \dot{F} F^{-1} = L^* + L^P \qquad (\ \ 4.4\ \ )$$

where L^P, accounts for crystallographic slip and component L^*, accounts for rigid body rotations and elastic deformation. Each component is respectively defined as

$$L^* = \dot{F}^* F^{*-1}, \qquad L^P = F^*(\dot{F}^P F^{P-1}) F^{*-1} \qquad (\ \ 4.5\ \ )$$

The symmetric strain rate tensor, D, and skew symmetric spin tensor, W, can be obtained from the velocity gradient

$$L = D + W \qquad (\ \ 4.6\ \ )$$

where

$$D = \frac{1}{2}(L + L^T), \qquad W = \frac{1}{2}(L - L^T) \qquad (\ \ 4.7\ \ )$$

Isolation of the elastic and plastic components produces the following

$$D = D^* + D^P, \qquad W = W^* + W^P \qquad (\ \ 4.8\ \ )$$

The plastic component of the strain-rate and spin for the crystal can be respectively written as

$$D^P = \sum_\alpha P^{(\alpha)} \dot{\gamma}^{(\alpha)}, \quad W^P = \sum_\alpha W^{(\alpha)} \dot{\gamma}^{(\alpha)} \qquad (\ \ 4.9\ \ )$$

where $\dot{\gamma}^{(\alpha)}$ is the shear rate on each slip system α. The expansion of the symmetric and skew-symmetric tensors for each slip system α are written as

$$P^{(\alpha)} = \frac{1}{2}\left[s^{*\,(\alpha)} \otimes m^{*\,(\alpha)} + m^{*\,(\alpha)} \otimes s^{*\,(\alpha)}\right] \qquad (\ \ 4.10\ \ )$$

$$W^{(\alpha)} = \frac{1}{2}\left[s^{*\,(\alpha)} \otimes m^{*\,(\alpha)} - m^{*\,(\alpha)} \otimes s^{*\,(\alpha)}\right] \qquad (\ \ 4.11\ \ )$$

The rate dependent elastic constitutive equation for a crystal is formulated as

$$\overset{\triangledown}{\tau^*} = \dot{\tau} - W^* \tau + \tau W^* = \mathbb{L}^{el} D^* \qquad (\quad \textbf{4.12} \quad)$$

where τ is the Kirchoff Stress, $\overset{\triangledown}{\tau^*}$ is the Jaumann rate of Kirchoff Stress on the crystal lattice coordinate system, and $\mathbb{L}^{el}$ is the rotated elastic moduli tensor. $\mathbb{L}^{el}$ is rotated from the 4th order elastic moduli tensor $\mathbb{L}$ by the crystal orientation.

$$\mathbb{L}^{el} = Q \, Q \, \mathbb{L} \, Q^T Q^T \qquad (\quad \textbf{4.13} \quad)$$

Cauchy stress can be related to Kirchoff stress through

$$\sigma = \det(F)^{-1} \tau \qquad (\quad \textbf{4.14} \quad)$$

The constitutive Equation 4.12 can be rewritten in terms of the Jaumann rate of Cauchy stress through

$$\overset{\triangledown}{\sigma} = \mathbb{L}^{el} D - \dot{\sigma}^0 - \sigma tr D \qquad (\quad \textbf{4.15} \quad)$$

where $\dot{\sigma}^0$ is the visco-plastic stress rate which is defined as

$$\dot{\sigma}^0 = \sum_\alpha R^{(\alpha)} \dot{\gamma}^{(\alpha)} \qquad (\quad \textbf{4.16} \quad)$$

based on the continuum slip $W^{(\alpha)}$, a second-order tensor $R^{(\alpha)}$ for each slip system is defined as follows

$$R^{(\alpha)} = \mathbb{L}^{el} P^{(\alpha)} + W^{(\alpha)} \sigma - \sigma W^{(\alpha)} \qquad (\quad \textbf{4.17} \quad)$$

The slip rates are used as inputs to equation 4.12 which are formulated in the framework of the power-law relation show below

$$\dot{\gamma}^{(\alpha)} = \dot{\gamma}_0 sgn(\tau^{(\alpha)}) \left| \frac{\tau^{(\alpha)}}{g^{(\alpha)}} \right|^{\frac{1}{m}} \qquad (\quad \textbf{4.18} \quad)$$

$\dot{\gamma}_0$ is a reference shear rate (taken to be the same for all the slip systems), m is the strain-rate sensitivity exponent, $\tau^{(\alpha)}$ is the resolved shear stresses and $g^{(\alpha)}$ is the hardness of each slip system. The resolved shear stresses on each slip system $\tau^{(\alpha)}$, is calculated using Schmid's Law [110].

$$\tau^{(\alpha)} = P^{(\alpha)} : \sigma \qquad (\quad \textbf{4.19} \quad)$$

The rate of hardness increase of a crystal evolves based on $\dot{g}^{(\alpha)}$ which is defined by the hardening law

$$\dot{g}^{(\alpha)} = \sum_{\beta} h_{(\alpha\beta)} |\dot{\gamma}^{(\beta)}|$$

(4.20)

where $h_{(\alpha\beta)}$ are the hardening moduli. *Asaro and Needleman* [111] proposed that the hardening moduli be defined as

$$h_{(\alpha\beta)} = q_{(\alpha\beta)} h_{(\beta)} \quad \text{(no sum on } \beta)$$

(4.21)

where $h_{(\beta)}$ is the hardening rate on a single slip system, and $q_{(\alpha\beta)}$ is a matrix that relates the latent hardening matrix of a slip system to the self-hardening rate. For a FCC crystal, the latent hardening matrix, $q_{(\alpha\beta)}^{FCC}$, is defined as

$$q_{(\alpha\beta)}^{FCC} = \begin{bmatrix} A & qA & qA & qA \\ qA & A & qA & qA \\ qA & qA & A & qA \\ qA & qA & qA & A \end{bmatrix}$$

(4.22)

A is a 3 x 3 unity matrix, and q is the latent hardening coefficient. In the above, slip systems {1,2,3} are coplanar, as are systems {4,5,6}, {7,8,9}, and {10,11,12}. Thus, the ratio of the latent-hardening rate to the self-hardening rate for coplanar systems are taken as unity. For a BCC crystal, the slip systems {1,2}, {3,4}, {5,6}, {7,8}, {9,10}, and {11,12} are coplanar while, slip systems 13-24 are of independent slip planes. Thus, the latent hardening matrix for a BCC crystal, $q_{(\alpha\beta)}^{BCC}$, is defined as

$$q_{(\alpha\beta)}^{BCC} = \begin{bmatrix} B & qB & qB & qB & qB & qB & \cdots & \\ qB & B & qB & qB & qB & qB & & \\ qB & qB & B & qB & qB & qB & & \\ qB & qB & qB & B & qB & qB & & qC \\ qB & qB & qB & qB & B & qB & & \\ qB & qB & qB & qB & qB & B & & \\ \cdots & & & & & & \cdots & \\ & & & qC & & & & C \end{bmatrix}$$

(4.23)

where B is a 2 x 2 unity matrix and C is a 12 x 12 unity matrix.

Many single crystal hardening models exist in literature, such as the models proposed by *Peirce et al.* [204], *Anand et al.* [205] [126], *Chang-Asaro* [206] and *Bassani and Wu* [207]. In this work, the power law hardening model [126] is used to describe the polycrystalline behaviour because of its accepted practice in modeling iron based crystals. The power law hardening model is

$$h_{(\beta)} = h_0 \left(\frac{h_0 \gamma_a}{\tau_0 n} + 1 \right)^{n-1} \qquad (\quad 4.24 \quad)$$

where h_0 is the initial hardening rate of the system, τ_0 is the initial critically resolved shear stress, n is the crystal hardening exponent and γ_a is the total accumulated slip defined by

$$\gamma_a = \int_0^t \sum_\alpha \left| \dot{\gamma}^{(\alpha)} \right| dt \qquad (\quad 4.25 \quad)$$

4.2 Transformation Criteria

Martensite transformation is modeled to occur at the intersection of shear fault bands, the method is similar to that employed by *Kim et al.* [163], however instead of using an energy based term, the fault band shear stress triggers the proposed transformation criterion. An instance of transformation occurs when the resolved shear stress on two or more of the twelve habit plane systems exceeds the transformation threshold, Γ^{th}, defined as

$$\Gamma^{th} = C_{t1} + C_{t2} \cdot \Gamma^{acc} \qquad (\quad 4.26 \quad)$$

where C_{t1}, C_{t2} are material parameters, and Γ^{acc} is the accumulated shear of the crystal. The accumulated slip Γ^{acc}, is the integration of the summation of the shear rates over time

$$\Gamma^{acc} = \int_0^t \left(\sum_\alpha^N \dot{\gamma}^{(\alpha)} \right) dt \qquad (\quad 4.27 \quad)$$

Similarly, the resolved shear stress is calculated on each of the fault band systems, α, using Schmid's Law (equation 4.19) for every austenite crystal.

$$\tau^{HP\,(\alpha)} = \boldsymbol{P}^{HP\,(\alpha)} : \boldsymbol{\sigma} \qquad (\quad 4.28 \quad)$$

where $\boldsymbol{P}^{HP\,(\alpha)}$ is calculated on the habit plane indices. When two or more components of $\tau^{HP\,(\alpha)}$ exceeds that of Γth transformation is modelled to take place.

4.3   Numerical Implementation

This chapter presents the numerical integration scheme of the crystal plasticity framework with martensitic transformation. The tangent modulus for rate dependent solids, known as the rate-tangent modulus method, developed by *Peirce et al.* [208] [209] is used for integrating the accumulated shear strain for every single crystal. A first order forward Euler method is used for stress integration of each crystal with Taylor-averaging for the polycrystal response. The formulation assumes planar loading conditions ($\dot{\sigma}_{33} = \Delta\sigma_{33} = 0$) and prescribed proportional in-plane strain increments ($\rho = \Delta D_{22}/\Delta D_{11}$). By solving a system of equations for mixed boundary conditions, the through thickness strain increment, ΔD_{33}, is determined at each iteration. After calculating stress for each crystal, FCC austenite crystals that satisfy the transformation criteria are transformed and mapped to a single BCC martensite crystals. The following presents the details for this implementation.

4.3.1   Rate Tangent Formulation

The slip system shear strain increment, $\Delta\gamma_t^{(\alpha)}$, on an individual slip system, α, at time t is given by

$$\Delta\gamma_t^{(\alpha)} = \gamma_{t+1}^{(\alpha)} - \gamma_t^{(\alpha)} \qquad (\quad 4.29\quad)$$

and a linear interpolation is employed within the time increment to give

$$\Delta\gamma_t^{(\alpha)} = \left[(1-\theta)\dot{\gamma}_t^{(\alpha)} + \theta\dot{\gamma}_{t+1}^{(\alpha)}\right]\Delta t \qquad (\quad 4.30\quad)$$

where Δt is the time increment, $\theta \in [0,1]$ such that $\theta = 0$ corresponds to Euler's first order forward method, $\theta = 1$ corresponds to Euler's first order backwards method, and $\theta = 0.5$ corresponds to a second order semi-implicit method. The instantaneous slip rate, $\dot{\gamma}_t^{(\alpha)}$, is calculated as

$$\dot{\gamma}_t^{(\alpha)} = \dot{\gamma}_0 sgn\left(\tau_t^{(\alpha)}\right)\left|\frac{\tau_t^{(\alpha)}}{g_t^{(\alpha)}}\right|^{1/m} \qquad (\quad 4.31\quad)$$

Using a first order Taylor series expansion, the instantaneous slip rate at the next time increment, $\dot{\gamma}_{t+\Delta t}^{(\alpha)}$

$$\dot{\gamma}_{t+1}^{(\alpha)} = \dot{\gamma}_t^{(\alpha)} + \left.\frac{\partial\dot{\gamma}^{(\alpha)}}{\partial\tau^{(\alpha)}}\right|_t \Delta\tau_t^{(\alpha)} + \left.\frac{\partial\dot{\gamma}^{(\alpha)}}{\partial g^{(\alpha)}}\right|_t \Delta g_t^{(\alpha)} \tag{4.32}$$

where $\Delta\tau_t^{(\alpha)} = \dot{\tau}_t^{(\alpha)}\Delta t$ and $\Delta g_t^{(\alpha)} = \dot{g}_t^{(\alpha)}\Delta t$. Substituting the constitutive equations and Equations 4.31 - 4.32 into equation 4.30, the slip system shear strain increment, $\Delta\gamma_t^{(\alpha)}$ can be expressed as

$$\Delta\gamma_t^{(\alpha)} = \left(\dot{f}^{(\alpha)} + \mathrm{F}_t^{(\alpha)} : \boldsymbol{D}\right)\Delta t \tag{4.33}$$

where

$$\dot{f}_t^{(\alpha)} = \sum_\beta \mathbb{M}_{\alpha\beta}\dot{\gamma}_t^{(\alpha)}, \quad \mathrm{F}_t^{(\alpha)} = \sum_\beta \mathbb{M}_{\alpha\beta}\boldsymbol{Q}_t^{(\alpha)}, \quad \boldsymbol{Q}_t^{(\alpha)} = \left(\frac{\theta\,\Delta t\,\dot{\gamma}_t^{(\alpha)}}{m\tau_t^{(\alpha)}}\right)\boldsymbol{R}_t^{(\alpha)} \tag{4.34}$$

where β indexes over the number of slip systems. Here, $\mathbb{M}$ is the inverse of $\mathbb{N}$ formulated as

$$\mathbb{N}_{\alpha\beta} = \delta_{\alpha\beta} + \frac{\theta\Delta t\,\dot{\gamma}_t^{(\alpha)}}{m}\left[\frac{\boldsymbol{R}_t^{(\alpha)}:\boldsymbol{P}_t^{(\alpha)}}{\tau_t^{(\alpha)}} + sgn\left(\tau_t^{(\alpha)}\right)\frac{h_{t\,(\alpha\beta)}}{g_t^{(\alpha)}}\right] \tag{4.35}$$

where $\boldsymbol{\delta}$ is the identity matrix and $h_{t\,(\alpha\beta)}$ is the hardening matrix at time, t. Thus, the elastic-plastic tangent modulus, $\mathbb{L}_t^{ep}$, can be calculated as

$$\mathbb{L}_t^{ep} = \mathbb{L}_t^{el} - \sum_\alpha \boldsymbol{R}_t^{(\alpha)} \otimes \mathrm{F}_t^{(\alpha)} \tag{4.36}$$

and the increment in viscoplastic stress, $\Delta\boldsymbol{\sigma}_t^0$, is

$$\Delta\boldsymbol{\sigma}_t^0 = \sum_\alpha \boldsymbol{R}_t^{(\alpha)}\,\dot{f}_t^{(\alpha)}\Delta t \tag{4.37}$$

4.3.2 Polycrystal Taylor Averaging, Stress Formulation and Boundary Conditions

The macroscopic strain of the polycrystal is imposed on the microscale onto every individual crystal. The strain tensor is dependent on the imposed loading condition.

$$\varepsilon^{(k)} = \varepsilon \rightarrow \Delta\boldsymbol{D}_{t+1}^{(k)} = \Delta\boldsymbol{D}_{t+1} \tag{4.38}$$

where k is an individual crystal. The stress of the polycrystal aggregate, $\bar{\boldsymbol{\sigma}}_t$, is the average of all individual crystal stresses

$$\overline{\sigma}_t = \frac{1}{N} \sum_{k=1}^{N} \sigma_t^{(k)} \qquad (\quad 4.39 \quad)$$

Similarly, the polycrystal aggregated viscoplastic stress increment, $\Delta\overline{\sigma}_t^0$

$$\Delta\overline{\sigma}_t^0 = \frac{1}{N} \sum_{k=1}^{N} \Delta\sigma_t^{0\,(k)} \qquad (\quad 4.40 \quad)$$

and the aggregated elastic-plastic tangent modulus, $\overline{\mathbb{L}}_t^{ep}$

$$\overline{\mathbb{L}}_t^{ep} = \frac{1}{N} \sum_{k=1}^{N} \overline{\mathbb{L}}_t^{ep\,(k)} \qquad (\quad 4.41 \quad)$$

The formulation assumes incremental planar loading conditions ($\Delta\overline{\sigma}_{33} = 0$) and prescribed proportional in-plane strain increments ($\rho = \Delta D_{22}/\Delta D_{11}$) on the aggregated polycrystal. Transverse shear strains are also constrained ($\Delta D_{13} = \Delta D_{23} = 0$). By solving a system of equations for mixed boundary conditions, the through thickness strain increment, ΔD_{33}, is determined at each iteration. Using a forward Euler scheme, the Cauchy stress state of the aggregated polycrystal is calculated at the next increment in time as

$$\begin{aligned}
\Delta\overline{\sigma}_t &= \overline{\sigma}_{t+1} - \overline{\sigma}_t \\
&= \overline{\mathbb{L}}_t^{ep}:\Delta D_{t+1} - \Delta\overline{\sigma}_t^0 + (\Delta W_{t+1}:\overline{\sigma}_t - \overline{\sigma}_t:\Delta W_{t+1}) - \overline{\sigma}_t\mathrm{tr}(\Delta D_{t+1})
\end{aligned} \qquad (\quad 4.42 \quad)$$

For a plane stress formulation, $\dot{\sigma}_{33} = \Delta\sigma_{33} = 0$, can be expressed as

$$\Delta\overline{\sigma}_{33,t} = \overline{\mathbb{L}}_{33kl,t}^{ep}:\Delta D_{kl,t+1} - \Delta\overline{\sigma}_{33,t}^0 = 0 \qquad (\quad 4.43 \quad)$$

leading to

$$\Delta D_{33,t+1} = \frac{\Delta\overline{\sigma}_{33,t}^0}{\overline{\mathbb{L}}_{3333,t}^{ep}} - \frac{\overline{\mathbb{L}}_{3311,t}^{ep}}{\overline{\mathbb{L}}_{3333,t}^{ep}}\Delta D_{11,t+1} - \frac{\overline{\mathbb{L}}_{3322,t}^{ep}}{\overline{\mathbb{L}}_{3333,t}^{ep}}\Delta D_{22,t+1} - 2\frac{\overline{\mathbb{L}}_{3312,t}^{ep}}{\overline{\mathbb{L}}_{3333,t}^{ep}}\Delta D_{12,t+1} \qquad (\quad 4.44 \quad)$$

The increment of stress for each crystal is then calculated as

$$\begin{aligned}
\Delta\sigma_t^{(k)} &= \mathbb{L}_t^{ep\,(k)}:\Delta D_{t+1} - \Delta\sigma_t^{0\,(k)} + \left(\Delta W_{t+1}:\sigma_t^{(k)} - \sigma_t^{(k)}:\Delta W_{t+1}\right) \\
&\quad - \sigma_t^{(k)}\mathrm{tr}(\Delta D_{t+1})
\end{aligned} \qquad (\quad 4.45 \quad)$$

and the stress of each crystal at the next time increment is

$$\sigma_{t+1}^{(k)} = \sigma_t^{(k)} + \Delta\sigma_t^{(k)} \tag{4.46}$$

4.3.3 Orientation Update for a Crystal

The orientation tensor, $\boldsymbol{Q}_t^{(k)}$, is initialized by three Bunge Euler angles (ϕ_1, Φ, ϕ_2). A first order incremental scheme is used to update the slip normal and vectors, spin tensor, orientation tensor of the crystal. The increment in plastic spin, $\Delta\boldsymbol{W}_{t+1}^P$, is calculated as

$$\Delta\boldsymbol{W}_{t+1}^P = \sum_\alpha \boldsymbol{W}_t^{(\alpha)} \, \Delta\gamma_t^{(\alpha)} \tag{4.47}$$

The increment in elastic spin, $\Delta\boldsymbol{W}_{t+1}^*$, is used to calculate the new orientation matrix

$$\Delta\boldsymbol{W}_{t+1}^* = \Delta\boldsymbol{W}_{t+1} - \Delta\boldsymbol{W}_{t+1}^P \tag{4.48}$$

where the orientation is updated accordingly

$$\boldsymbol{Q}_{t+1} = (\boldsymbol{I} + \Delta\boldsymbol{W}_{t+1}^*)\boldsymbol{Q}_t \tag{4.49}$$

Similarly, a first order incremental scheme is used to update the slip system normal and vectors. The increment in the plastic deformation gradient is calculated as

$$\Delta\boldsymbol{F}_{t+1}^P = \boldsymbol{I} + \sum_\alpha \left(\boldsymbol{P}_t^{(\alpha)} + \boldsymbol{W}_t^{(\alpha)}\right) \Delta\gamma_t^{(\alpha)} \tag{4.50}$$

and the increment in the elastic deformation is

$$\Delta\boldsymbol{F}_{t+1}^* = \boldsymbol{I} + (\Delta\boldsymbol{D}_{t+1} + \Delta\boldsymbol{W}_{t+1}) - \sum_\alpha \left(\boldsymbol{P}_t^{(\alpha)} + \boldsymbol{W}_t^{(\alpha)}\right) \Delta\gamma_t^{(\alpha)} \tag{4.51}$$

Finally, the crystal slip planes and slip vectors are updated

$$\boldsymbol{s}_{t+1}^{*\,(\alpha)} = \Delta\boldsymbol{F}_{t+1}^* \boldsymbol{s}_t^{*\,(\alpha)}, \quad \boldsymbol{m}_{t+1}^{*\,(\alpha)} = \boldsymbol{m}_t^{*\,(\alpha)}\Delta\boldsymbol{F}_{t+1}^{*-1} \tag{4.52}$$

4.3.4   Transformation Criteria

The transformation threshold is calculated at the end of each increment for each FCC austenite crystal

$$\Gamma_{t+1}^{th} = C_{t1} + C_{t2} \cdot \Gamma_{t+1}^{acc} \tag{4.53}$$

where the total accumulated slip

$$\Gamma_{t+1}^{acc} = \sum_{\alpha} \left| \gamma_{t+1}^{(\alpha)} \right| \tag{4.54}$$

The resolved shear stress on the 12-fault band normal and vectors are calculated using the current stress state where

$$P_{t+1}^{HP\,(\alpha)} = \frac{1}{2} \left[s_{t+1}^{HP\,(\alpha)} \otimes m_{t+1}^{HP\,(\alpha)} + m_{t+1}^{HP\,(\alpha)} \otimes s_{t+1}^{HP\,(\alpha)} \right] \tag{4.55}$$

and

$$\tau_{t+1}^{HP\,(\alpha)} = P_{t+1}^{HP\,(\alpha)} : \sigma_{t+1} \tag{4.56}$$

In a similar manner to updating the crystal lattice, the fault band normal and vectors are updated as

$$s_{t+1}^{HP\,(\alpha)} = \Delta F_{t+1}^* s_t^{HP\,(\alpha)}, \quad m_{t+1}^{HP\,(\alpha)} = m_t^{HP\,(\alpha)} \Delta F_{t+1}^{*-1} \tag{4.57}$$

When two or more fault bands exceed the transformation threshold (representing an intersection of fault bands)

$$\tau_{t+1}^{HP\,(\alpha)} \geq \Gamma_{t+1}^{th} \tag{4.58}$$

the austenite crystal is transformed to martensite. Following the Bain orientation relationship, the newly formed BCC crystal lattice is rotated about the $< 001 >$ crystal axis by $45°$ that follows the single variant Bain relationship, such that

$$Q^{trans} = Q_{t+1}(\phi_1 + 45°, \Phi, \phi_2) \tag{4.59}$$

and the orientation of the BCC slip systems s_0^{BCC} replace the FCC slip systems, $s_{t+1}^{*\,FCC}$ such that

$$s^*_{t+1} = Q^{trans} s^{BCC}_0 \qquad (\quad 4.60 \quad)$$

Finally, the power-law hardening parameters of martensite are mapped over to replace the austenite parameters $\left(h^\gamma_0, \tau^\gamma_0, n^\gamma \to h^{\alpha'}_0, \tau^{\alpha'}_0, n^{\alpha'}\right)$ and the accumulated shear on each slip is reinitialized

$$\gamma^{(\alpha)}_{t+1} = 0 \qquad (\quad 4.61 \quad)$$

4.3.5 Polycrystal Stress Integration Algorithm with Transformation Effects

The steps in the integration of stress for the polycrystal response with transformation effects are as follows:

(1) Subroutine entry of polycrystal with known values of $\overline{\boldsymbol{\sigma}}_t, \boldsymbol{\sigma}^{(k)}_t, \boldsymbol{s}^{*\,(k)}_t, \boldsymbol{m}^{*\,(k)}_t, \boldsymbol{\gamma}^{(k)}_t, \boldsymbol{g}^{(k)}_t,$
$\boldsymbol{Q}^{(k)}_t, \Delta D_{11,t+1}, \Delta D_{22,t+1}, \Delta D_{12,t+1}, \Delta W_{t+1}, \Delta t_{t+1}, \boldsymbol{s}^{HP\,(\alpha)}_t$ and $\boldsymbol{m}^{HP\,(\alpha)}_{t+1}$ (if applicable)

(2) Calculate the crystal elastic-plastic and viscoplastic stress tensors for all crystals

    i.   Initialize index for grains $k = 1$

    ii.   Calculate the rotated crystal elasticity tensor for the crystal

$$\mathbb{L}^{el}_t = \boldsymbol{Q}^{(k)}_t \boldsymbol{Q}^{(k)}_t \mathbb{L}\, \boldsymbol{Q}^{T\,(k)}_t \boldsymbol{Q}^{T\,(k)}_t$$

    iii.   Calculate the symmetric and anti-symmetric plastic slip tensors

$$\boldsymbol{P}^{(\alpha)}_t = \frac{1}{2}\left(\boldsymbol{s}^{*\,(k,\alpha)}_t \otimes \boldsymbol{m}^{*\,(k,\alpha)}_t + \boldsymbol{m}^{*\,(k,\alpha)}_t \otimes \boldsymbol{s}^{*\,(k,\alpha)}_t\right) \qquad \text{Symmetric Slip Tensor}$$

$$\boldsymbol{W}^{(\alpha)}_t = \frac{1}{2}\left(\boldsymbol{s}^{*\,(k,\alpha)}_t \otimes \boldsymbol{m}^{*\,(k,\alpha)}_t + \boldsymbol{m}^{*\,(k,\alpha)}_t \otimes \boldsymbol{s}^{*\,(k,\alpha)}_t\right) \qquad \text{Anti-symmetric Slip Tensor}$$

    iv.   Calculate resolved shear stress on each slip system

$$\tau^{(\alpha)}_t = \boldsymbol{P}^{(\alpha)}_t : \boldsymbol{\sigma}^{(k)}_t$$

    v.   Calculate the instantaneous shear rate

$$\dot{\gamma}^{(\alpha)}_t = \dot{\gamma}_0 sgn\left(\tau^{(\alpha)}_t\right)\left|\frac{\tau^{(\alpha)}_t}{g^{(k,\alpha)}_t}\right|^{1/m}$$

    vi.   Calculate the second order tensor, $\boldsymbol{R}^{(\alpha)}_t$

$$R_t^{(\alpha)} = \mathbb{L}_t^{el} : P_t^{(\alpha)} + W_t^{(\alpha)} \sigma_t^{(k)} - \sigma_t^{(k)} W_t^{(\alpha)}$$

vii. Calculate the hardening modulus matrix based on the crystal structure

$$h_{(\beta)} = h_0 \left(\frac{h_0 \gamma_t^{(\beta,k)}}{\tau_0 n} + 1 \right)^{n-1}$$

$$h_{t\,(\alpha\beta)}^{(k)} = q_{(\alpha\beta)} h_{(\beta)}$$

viii. Calculate the rate-tangent modulus matrices

$$\mathbb{N}_{\alpha\beta} = \delta_{\alpha\beta} + \frac{\theta \Delta t \, \dot{\gamma}_t^{(\alpha)}}{m} \left[\frac{R_t^{(\alpha)} : P_t^{(\alpha)}}{\tau_t^{(\alpha)}} + sgn\left(\tau_t^{(\alpha)} \right) \frac{h_{t\,(\alpha\beta)}^{(k)}}{g_t^{(\alpha)}} \right]$$

$$\mathbb{N} = \mathbb{M}^{-1}$$

$$Q_t^{(\alpha)} = \left(\frac{\theta \Delta t \, \dot{\gamma}_t^{(\alpha)}}{m \tau_t^{(\alpha)}} \right) R_t^{(\alpha)}$$

$$\dot{f}_t^{(k,\alpha)} = \sum_{\beta} \mathbb{M}_{\alpha\beta} \dot{\gamma}_t^{(\alpha)}$$

$$F_t^{(k,\alpha)} = \sum_{\beta} \mathbb{M}_{\alpha\beta} Q_t^{(\alpha)}$$

ix. Calculate the elastic-plastic and viscoplastic stress tensors

$$\mathbb{L}_t^{ep\,(k)} = \mathbb{L}_t^{el} - \sum_{\alpha} R_t^{(\alpha)} \otimes F_t^{(\alpha)} \qquad \text{Elastic-plastic tensor}$$

$$\Delta\sigma_t^{0\,(k)} = \sum_{\alpha} R_t^{(\alpha)} \dot{f}_t^{(\alpha)} \Delta t_{t+1} \qquad \text{Viscoplastic stress tensor}$$

x. IF $k <$ number of grains, $k = k + 1$ and GO TO Step ii

(3) Solve the boundary conditions for plane stress condition

i. Calculate the aggregated elastic-plastic stress increment

$$\overline{\mathbb{L}}_t^{ep} = \frac{1}{N} \sum_{k=1}^{N} \overline{\mathbb{L}}_t^{ep\,(k)}$$

ii. Calculate the aggregated viscoplastic stress increment

$$\Delta\bar{\sigma}_t^0 = \frac{1}{N}\sum_{k=1}^{N}\Delta\sigma_t^{0\,(k)}$$

iii.   Calculate the through thickness strain increment

$$\Delta D_{33,t+1} = \frac{\Delta\bar{\sigma}_{33,t}^0}{\overline{\mathbb{L}}_{3333,t}^{ep}} - \frac{\overline{\mathbb{L}}_{3311,t}^{ep}}{\overline{\mathbb{L}}_{3333,t}^{ep}}\Delta D_{11,t+1} - \frac{\overline{\mathbb{L}}_{3322,t}^{ep}}{\overline{\mathbb{L}}_{3333,t}^{ep}}\Delta D_{22,t+1} - 2\frac{\overline{\mathbb{L}}_{3312,t}^{ep}}{\overline{\mathbb{L}}_{3333,t}^{ep}}\Delta D_{12,t+1}$$

(4) Update the stress, orientation and accumulated slip of each crystal

i.   Initialize index for grains $k = 1$

ii.   Calculate the slip on each slip system for the next increment

$$\Delta\gamma_t^{(k,\alpha)} = \dot{f}_t^{(k,\alpha)}\Delta t_{t+1} + \mathrm{F}_t^{(k,\alpha)}:\Delta\boldsymbol{D}_{t+1}$$

$$\gamma_{t+1}^{(k,\alpha)} = \gamma_t^{(k,\alpha)} + \Delta\gamma_t^{(k,\alpha)}$$

iii.   Calculate the hardness of each slip system for the next increment

$$\Delta g_t^{(k,\alpha)} = \sum_{\beta} h_{t\,(\alpha\beta)}^{(k)}\,\Delta\gamma_t^{(k,\beta)}$$

$$g_{t+1}^{(k,\alpha)} = g_t^{(k,\alpha)} + \Delta g_t^{(k,\alpha)}$$

iv.   Compute the orientation matrix for the next increment

$$\Delta\boldsymbol{W}_{t+1}^P = \sum_{\alpha}\boldsymbol{W}_t^{(\alpha)}\,\Delta\gamma_t^{(k,\alpha)}\qquad\text{Plastic spin increment}$$

$$\Delta\boldsymbol{W}_{t+1}^* = \Delta\boldsymbol{W}_{t+1} - \Delta\boldsymbol{W}_{t+1}^P\qquad\text{Elastic spin increment}$$

$$\boldsymbol{Q}_{t+1}^{(k)} = (\boldsymbol{I} + \Delta\boldsymbol{W}_{t+1}^*)\boldsymbol{Q}_t^{(k)}$$

v.   Update the crystal lattice slip normal and vectors

$$\Delta\boldsymbol{F}_{t+1}^{P\,(k)} = \boldsymbol{I} + \sum_{\alpha}\left(\boldsymbol{P}_t^{(k,\alpha)} + \boldsymbol{W}_t^{(k,\alpha)}\right)\Delta\gamma_t^{(k,\alpha)}\qquad\text{Plastic deformation increment}$$

$$\Delta\boldsymbol{F}_{t+1}^{*(k)} = \boldsymbol{I} + (\Delta\boldsymbol{D}_{t+1} + \Delta\boldsymbol{W}_{t+1})$$
$$-\sum_{\alpha}\left(\boldsymbol{P}_t^{(k,\alpha)} + \boldsymbol{W}_t^{(k,\alpha)}\right)\Delta\gamma_t^{(k,\alpha)}\qquad\text{Elastic deformation increment}$$

$$\boldsymbol{s}_{t+1}^{*\,(k)} = \Delta\boldsymbol{F}_{t+1}^{*(k)}\boldsymbol{s}_t^{*\,(k)}$$

$$\boldsymbol{m}_{t+1}^{*\,(k)} = \boldsymbol{m}_t^{*\,(k)}\left(\Delta\boldsymbol{F}_{t+1}^{*(k)}\right)^{-1}$$

vi.   Update the stress for each crystal

$$\Delta\boldsymbol{\sigma}_t^{(k)} = \mathbb{L}_t^{ep\,(k)} : \Delta\boldsymbol{D}_{t+1} - \Delta\boldsymbol{\sigma}_t^{0\,(k)} + \left(\Delta\boldsymbol{W}_{t+1} : \boldsymbol{\sigma}_t^{(k)} - \boldsymbol{\sigma}_t^{(k)} : \Delta\boldsymbol{W}_{t+1}\right) - \boldsymbol{\sigma}_t^{(k)} \mathrm{tr}(\Delta\boldsymbol{D}_{t+1})$$

$$\boldsymbol{\sigma}_{t+1}^{(k)} = \boldsymbol{\sigma}_t^{(k)} + \Delta\boldsymbol{\sigma}_t^{(k)}$$

vii.   IF $k <$ number of grains, $k = k + 1$ and GO TO Step ii

(5) Apply transformation criteria to austenite crystals

    i.   Initialize index for grains $k = 1$

    ii.   IF NOT AN AUSTENITE CRYSTAL, GO TO Step viii

    iii.   Update the habit plane slip normal and vectors

$$\boldsymbol{s}_{t+1}^{HP\,(k,\alpha)} = \Delta\boldsymbol{F}_{t+1}^{*(k)} \boldsymbol{s}_t^{HP\,(k,\alpha)}$$

$$\boldsymbol{m}_{t+1}^{HP\,(k,\alpha)} = \boldsymbol{m}_t^{HP\,(k)} \left(\Delta\boldsymbol{F}_{t+1}^{*(k,\alpha)}\right)^{-1}$$

    iv.   Calculate the resolved shear stress on the habit planes

$$\boldsymbol{\tau}_{t+1}^{HP\,(k,\alpha)} = \boldsymbol{P}_{t+1}^{HP\,(k,\alpha)} : \boldsymbol{\sigma}_{t+1}^{(k)}$$

    v.   Calculate the transformation criteria

$$\Gamma_{t+1}^{acc\,(k)} = \sum_\alpha \left|\gamma_{t+1}^{(k,\alpha)}\right| \qquad\qquad \text{The accumulated slip on all slip systems}$$

$$\Gamma_{t+1}^{th\,(k)} = C_{t1} + C_{t2} \cdot \Gamma_{t+1}^{acc\,(k)}$$

    vi.   IF two habit planes satisfy $\boldsymbol{\tau}_{t+1}^{HP\,(k,\alpha)} \geq \Gamma_{t+1}^{th\,(k)}$ CONTINUE

                ELSE GO TO Step viii

    vii.   Transform austenite crystal to martensite crystal

$$\boldsymbol{Q}_{t+1} = \boldsymbol{Q}^{trans} = \boldsymbol{Q}_{t+1}(\phi_1 + 45°, \Phi, \phi_2) \quad$$ Rotate crystal according to Bain orientation

$$\boldsymbol{s}_{t+1}^* = \boldsymbol{Q}_{t+1} \boldsymbol{s}_0^{BCC} \qquad\qquad\qquad\qquad$$ Map orientation to BCC crystal

$$h_0^\gamma, \tau_0^\gamma, n^\gamma \rightarrow h_0^{\alpha'}, \tau_0^{\alpha'}, n^{\alpha'} \qquad\qquad$$ Change hardening parameters

$$\gamma_{t+1}^{(k,\alpha)} = 0 \qquad\qquad\qquad\qquad\qquad$$ Reset accumulated shear on slip systems

    viii.   IF $k <$ number of grains, $k = k + 1$ and GO TO Step ii

(6) Update the aggregated stress of the polycrystal

$$\overline{\boldsymbol{\sigma}}_{t+1} = \frac{1}{N} \sum_{k=1}^{N} \boldsymbol{\sigma}_{t+1}^{(k)}$$

5 FORMING LIMIT CALCULATIONS

The framework for crystal plasticity MK analysis is developed by *Wu et al.* [198], and used by *Inal et al.* [118] is employed in this thesis. Figure 22 presents a schematic of the theoretical model used in the MK framework. The theoretical model assumes a smooth continuous variation in the thickness region of sheet material called a band, "b". This band is oriented at an angle, Ψ_0, concerning the principal axis with an initial thickness, t_0^b. The region outside of the band, known hereon as region, "a", is assumed to have initial uniform thickness, t_0^a.
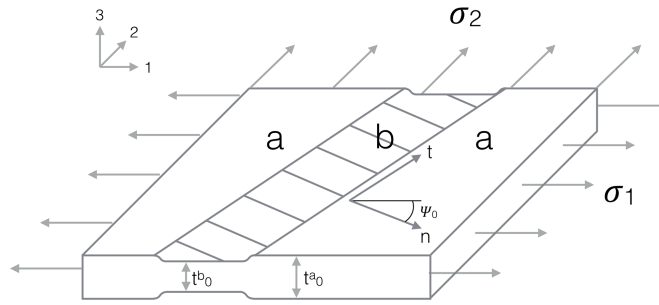
Figure 22: Geometrical model of the Marciniak-Kuczynski theory [45]

The initial imperfection parameter, f, which is known as the coefficient of geometrical non-homogeneity, is the ratio of band thickness $(\ )^b$ and the bulk material $(\ )^a$ is defined

$$f = \frac{t_0^b}{t_0^a} \qquad (\quad 5.1 \quad)$$

Deformation is imposed on the edges of the sheet, such that

$$\frac{D_{22}}{D_{11}} = \frac{\dot{\varepsilon}_{22}}{\dot{\varepsilon}_{11}} = \rho = const, D_{12} = 0, \ W_{12} = 0, \qquad (\quad 5.2 \quad)$$

where $\dot{\varepsilon}_{22} \equiv D_{22}$ and $\dot{\varepsilon}_{11} \equiv D_{11}$ are the principal logarithmic strain rates, ρ is the strain proportionality constant and W_{ij} are components of the spin tensor. Additionally, $D_{13} = D_{23} = W_{13} = W_{23} = 0$ is assumed, while D_{33} is determined by the plane stress condition ($\dot{\sigma}_{33} = 0$). The evolution of the current groove orientation, Ψ, is given by

$$\tan \Psi = \exp[(1 - \rho)\varepsilon_{11}] \tan \Psi_0 \qquad (\quad 5.3 \quad)$$

Apart from the necessary conditions at the band interface, uniform deformations are assumed both inside and outside the band, equilibrium and compatibility inside and outside the band are

automatically satisfied. Following *Hutchinson and Neale* [184] [185], the compatibility condition at the band interface is given in terms of the velocity gradient differences inside and outside the band are defined as

$$\mathbf{L}_{\alpha\beta}^b = \mathbf{L}_{\alpha\beta} + \dot{c}_\alpha n_\beta \qquad (\text{ 5.4 })$$

with the symmetric and skew-symmetric components of the velocity gradient in the band are

$$D_{\alpha\beta}^b = D_{\alpha\beta} + \frac{1}{2}\left(\dot{c}_\alpha n_\beta + n_\alpha \dot{c}_\beta\right), \qquad W_{\alpha\beta}^b = W_{\alpha\beta} + \frac{1}{2}\left(\dot{c}_\alpha n_\beta - n_\alpha \dot{c}_\beta\right) \qquad (\text{ 5.5 })$$

where $\dot{c}_\alpha$ values are the parameters to be determined, and n_α are components of the unit normal vectors to the band orientation given as

$$n_1 = \cos \Psi, \qquad n_2 = \sin \Psi \qquad (\text{ 5.6 })$$

Force equilibrium is established inside and outside of the band by

$$n_\alpha^b \sigma_{\alpha\beta}^b t^b = n_\alpha^a \sigma_{\alpha\beta}^a t^a \qquad (\text{ 5.7 })$$

As outlined in Wu et al. [198], substituting the incremental form of the constitutive relation (Section 4) into the incremental form of the force equilibrium (Equation 4.35) with plane stress ($\dot{\sigma}_{33} = 0$) leads to three algebraic equations for solving $\dot{c}_1$, $\dot{c}_2$ and D_{33}^b. The elastic-viscoplastic crystal plasticity formulation is then used to calculate the corresponding moduli, $\mathbb{L}$, and viscoplastic stress rates, $\dot{\sigma}^0$ inside and outside the band. Henceforth, the rates $\dot{c}_\alpha$, or $D_{\alpha\beta}^b$ and D_{33}^b inside the band are directly calculated by solving the three above-mentioned algebraic equations. Finally, the sheet thickness inside and outside the band are updated according to

$$\dot{t}^a = D_{33}t^a, \qquad \dot{t}^b = D_{33}^b t^b \qquad (\text{ 5.8 })$$

The next increment in time is established by the implementation of a one-step explicit rate-tangent method outlined in Section 4.3. Furthermore, the method of adaptive time-stepping developed by *Van der Giessen and Neale* [210] is incorporated for computational efficiency. According to *Hutchinson and Neale* [184], the onset of localized sheet necking is defined by the ratio of the in-band and out-of-band region exceeding $\dot{\varepsilon}_{33}^b/\dot{\varepsilon}_{33} \geq 10^4$.

6 MATERIAL CHARACTERIZATION & CALIBRATION

The proposed crystallographic transformation model is calibrated to experimental measurements presented in *Kim et al.* [163] of a duplex stainless TRIP assisted steel. Table 7 presents the chemical composition of the DSS used in this study. This particular alloy was developed to provide stress corrosion cracking resistance and high strength, achieved by a microstructure phase combination of austenite, ferrite and TRIP effect. The DSS consists of 65% ferrite and 35% retained austenite by volume.

Table 7: TR-DSS Chemical Composition [163]

C	Si	Mn	Cr	Ni	Mo	Cu	N	Fe
0.03	0.6	1.8	21.9	2.5	0.6	0.5	0.17	Remainder

6.1 Texture Measurement

The material's initial microstructure (as presented in *Kim et al.* [163]) that is employed in this study was provided by Professor Shi-Hoon Choi from Sunchun National University in the Republic of Korea. Electron backscatter diffraction (EBSD) was used to obtain the crystal orientation and microstructure phase identification for the material for three sections: the rolling direction (RD), transverse direction (TD), and normal direction (ND). Figure 23 presents a 3D representation of the crystal orientations obtained from the EBSD of the different sections. Figure 23 also presents the phase composition of the material. Figure 24 presents the corresponding orientation distribution function (ODF) for each EBSD section as presented in *Kim et al.* [163].
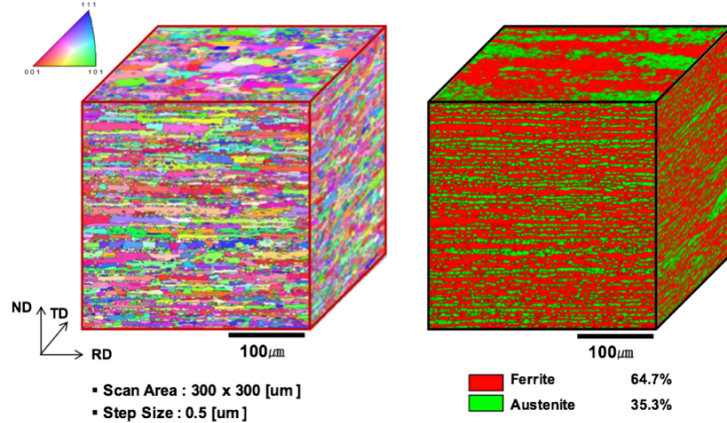
Figure 23: EBSD scans of rolling direction, transverse direction and normal direction of crystal orientations and individual phase identification [163]
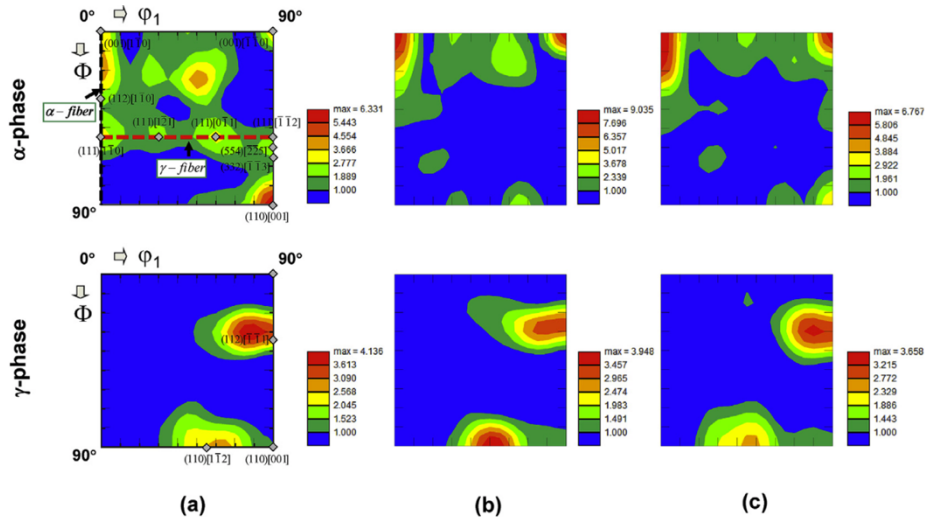
Figure 24: $\psi_2 = 45°$ Orientation Distribution Functions (ODF) for ferrite and austenite phases of a). ND Section b). TD Section and c). RD Section [163]

The provided crystal orientations were analyzed using TSL software [211] and MATLAB MTEX 4.5.0 analysis software [212] and compared with the original plots presented by *Kim et al*. [163]. It should be mentioned that the ODF plots presented by *Kim et al*. [163] utilized the TSL software. Figure 25 presents a comparison of the original ODF; the resampled ODF plotted by TSL and MTEX with good visual comparison. Minor differences in intensity and coloration are due to differences in software calculations of distribution functions necessary for approximation. The major texture components of the γ- austenite phase can be identified as Copper ($\{112\} < 11\bar{1} >$) and Brass ($\{110\} < 1\bar{1}2 >$). The texture components of the α- ferrite phase is that of Rotated Cube ($\{100\} < 1\bar{1}0 >$) and Goss ($\{110\} < 001 >$).

58
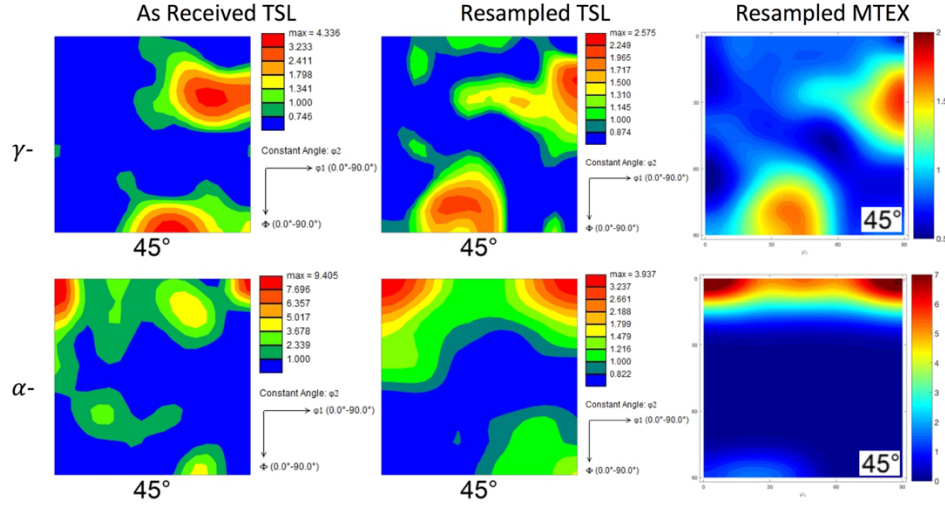
Figure 25: ODF generated by TSL vs resampled ODF generated by TSL vs resampled ODF generated by MTEX

6.2 Model Calibration

Table 8 presents a summary of the elasticity constants of α- ferrite and γ- austenite used in the model as presented in *Fréour et al.* [213]. α'- Martensite uses the same elasticity constants as that of α- ferrite, due to crystal similarities. The calibration of the uniaxial tension data was treated as an error minimization exercise. Initially, transformation was turned off and ferrite and austenite response were fit to reduce the number of material parameter. This exclusion of the martensite elastic-plastic behavior focused on the elastic-plastic behavior of ferrite and austenite during the first 10% of deformation. Upon obtaining an initial reasonable fit (seen in Figure 26), the complete overall response with transformation was calibrated for the martensite elastic-plastic behavior and transformation parameters. The experimental stress strain curve was simultaneously fit with the volume fraction data to obtain martensite parameters and transformation parameters. Figure 27 presents the resulting of the experimental and calibrated stress-strain curves. Table 9 summarizes the calibrated individual phase parameters. Table 10 summarizes the transformation criteria parameters. The experimental stress strain curve showed a maximum deviation of 32 MPa between 20-30% strain, an relative error of 3.6%. The experimental volume fraction of austenite and martensite also showed deviation of a maximum of 4% volume fraction to the calibrated curve at strain of 10%. However, subsequent experimental volume fraction data showed good agreement to the calibrated curve.

Table 8: Elastic properties of individual phases [213]

Phase	C_{11} (GPa)	C_{12} (GPa)	C_{44} (GPa)
Ferrite, α	231.4	134.7	116.4
Martensite, α'	231.4	134.7	116.4
Austenite, γ	197.5	124.5	122

Table 9: Crystal plasticity material parameters for individual phases

Phase	h_0	m	τ_0	q	n
Ferrite, α	132	0.05	128	1.00	0.15
Martensite, α'	1000	0.05	230	1.00	0.22
Austenite, γ	95	0.05	95	1.00	0.16

Table 10: Transformation criteria parameters

C_{t1}	C_{t2}
300	24
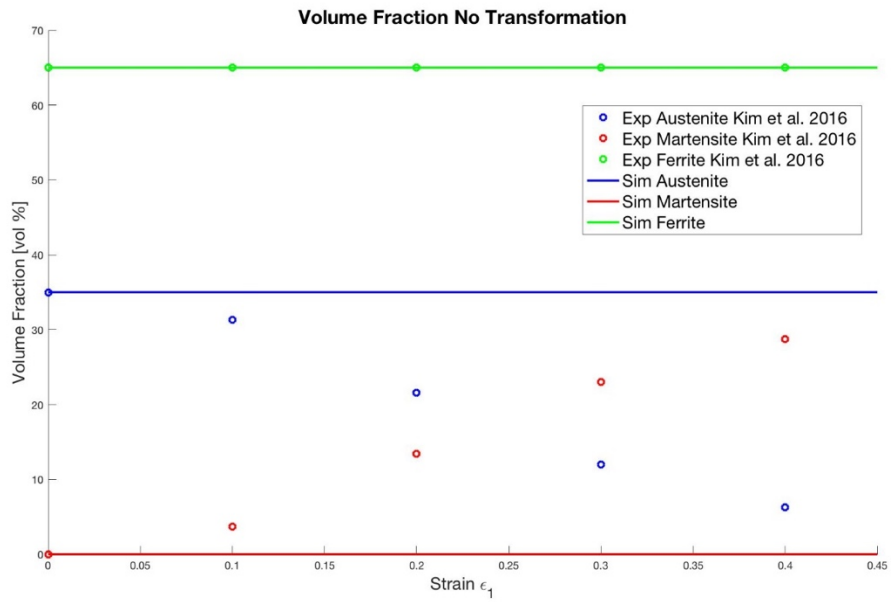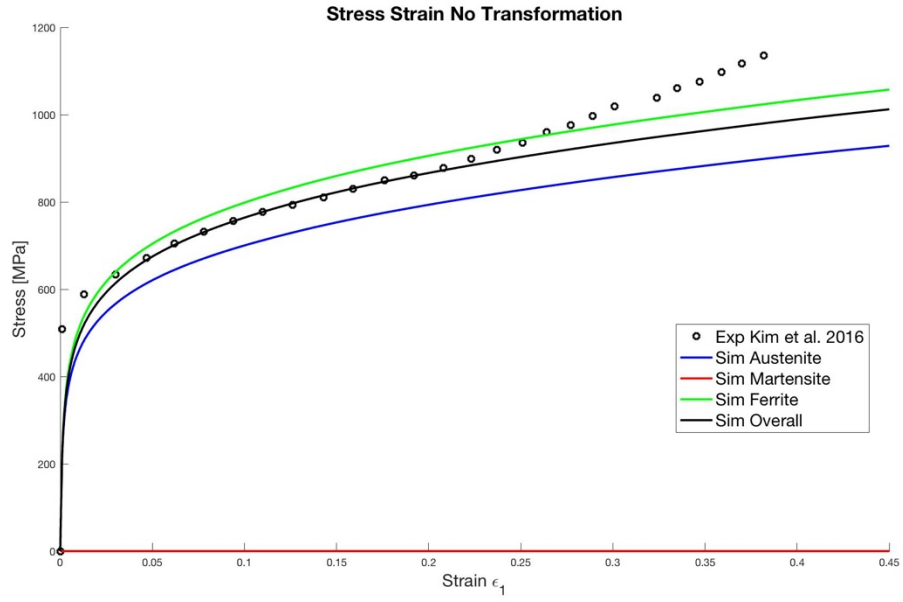
Figure 26: Experimental and calibrated uniaxial stress-strain curve and phase volume fractions without transformation
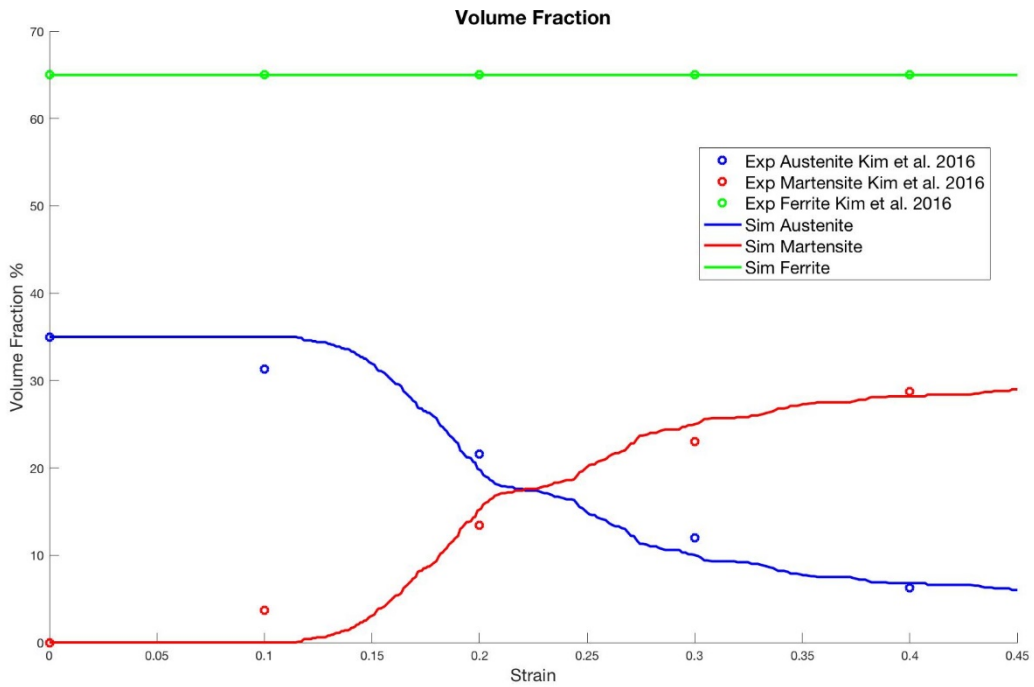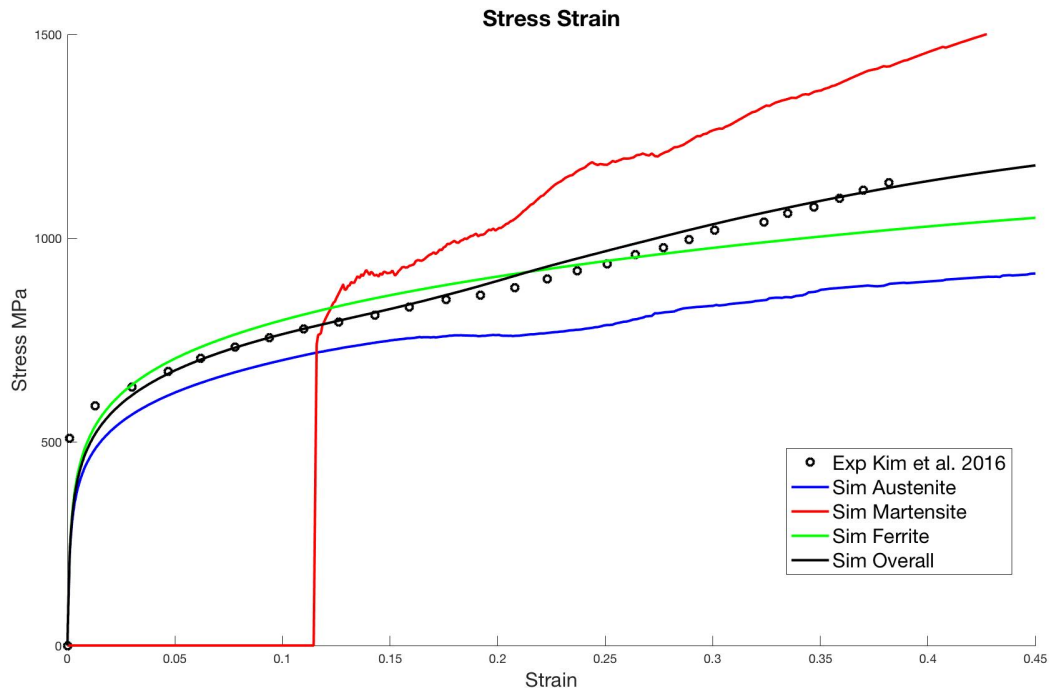
Figure 27: Experimental and calibrated uniaxial stress-strain curve and phase volume fractions with transformation

7   RESULTS & DISCUSSION

This chapter presents the simulation results of single crystal, polycrystal, and forming limit diagrams for the TRIP-assisted DSS studied. A study on microstructure evolution and preferred transformation orientations is presented and discussed for various strain paths. Using the MK analysis with the proposed transformation framework, forming limit diagrams are simulated for the studied material. Lastly, the effect of transformation criterion on FLD is explored and discussed through a parametric study of C_{t1} and C_{t2}.

7.1   Single Crystal Model

To demonstrate the capability of the proposed crystal plasticity transformation framework, simulations of single crystals are performed under uniaxial tension along the RD.   Three simulations were performed and are outlined as follows:

1) A non-transforming FCC crystal denoted as "FCC".
2) A non-transforming BCC crystal denoted as "BCC".
3) A transforming FCC to BCC crystal denoted as "Transform".

The FCC single crystal simulation used the material parameters (Table 9) for γ- austenite, while the BCC single crystal used the material parameters for α'- martensite. A random orientation ($\varphi_1 = -98.26°$, $\Phi = 40.47°$, $\varphi_2 = 86.37°$) is used for each simulation. Figure 28 presents the stress-strain curves of the single crystal simulations to highlight the effect of TRIP at a single crystal level. A significant difference is observed in the strength and hardening between the FCC and BCC crystal without transformation because of the difference in properties of the soft γ- austenite and hard α'- martensite phase. Figure 28 also presents the {100} pole figure of the single crystal and the corresponding evolution of φ_1. The orientation of the non-transforming FCC and transforming FCC to BCC crystals are represented by blue and red lines respectively. The transforming FCC single crystal behaviour follows the FCC crystal behaviour, until a strain of 0.20 is reached where the stress-based transformation criteria is satisfied. Once satisfied, an instanteous rotation of the crystal occurs according to the single variant Bain orientation. The orientation slip systems and hardening parameters are changed from a FCC (anustenite) crystal to the BCC (martensite) crystal, and the accumulated shear is reset to zero. This transformation can be seen in two ways: First,

there is a crystal rotation of $\varphi_1 + 45°$ at 0.20 strain. Secondly, there is an initial elastic loading of the newly formed BCC crystal that converges to the stress level of a non-transforming BCC crystal upon further deformation.
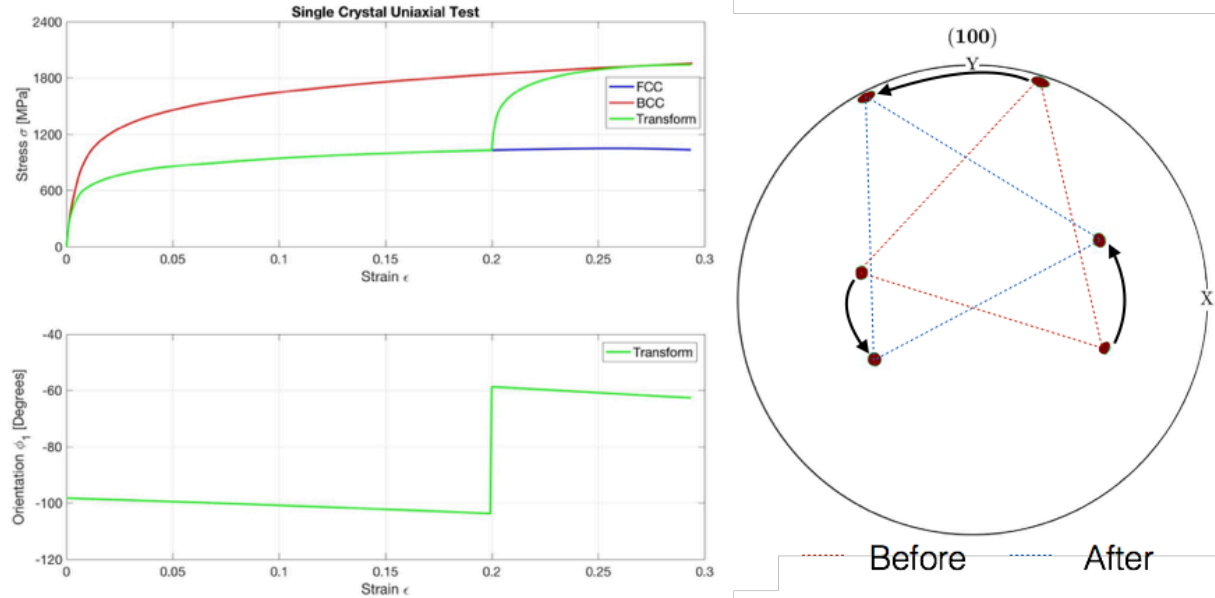
Figure 28: Uniaxial tension stress strain and texture evolution of a single crystal FCC, BCC and FCC>BCC transformation simulation

7.2 Polycrystalline Model

Polycrystalline simulations were performed using the DSS crystal texture, material parameters for individual phases and transformation criterion parameters presented in Chapter 6. Simulations of uniaxial tension, plane strain tension, and equi-biaxial tension and the resulting orientation distribution are presented and discussed.

7.2.1 Uniaxial Tension ($\rho = -0.5$)

Two studies are performed to investigate the sensitivity of transformation due to the initial sheet orientation: uniaxial tension along the rolling direction (RD) and transverse direction.

7.2.1.1 Uniaxial Tension along the Rolling Direction

Table 11 - Table 13 presents the simulated texture evolution of α- ferrite, γ- austenite and α'- martensite phases respectively at various strain level (0%, 10%, 20%, 30% and 40%) along the RD. It should be mentioned that no figures are presented for 0% and 10% strain for martensite

because little to no martensite was generated at that time. Table 11 - Table 13 also presents the corresponding phase volume fraction at the different strain levels. The corresponding uniaxial tensile (UA) stress-strain response of the DSS in the RD was presented above in Figure 27. The α- ferrite phase initially began with a noticeable rotated cube ($\varphi_1 = 0°, \Phi = 0°, \varphi_2 = 45°$) texture. However, during deformation, the texture further strengthens to a rotated cube texture. At 40% strain, an additional weak pole began to evolve at ($\varphi_1 = 0°, \Phi = 70°, \varphi_2 = 45°$).

The $\gamma-$ austenite phase shows a weak texture of brass ($\varphi_1 = 35°, \Phi = 45°, \varphi_2 = 0°$) and copper ($\varphi_1 = 0°, \Phi = 35°, \varphi_2 = 45°$) initially. Before transformation occurs (~10% strain), γ-austenite still exhibits a weak texture with the highest intensity at ($\varphi_1 = 45°, \Phi = 90°, \varphi_2 = 45°$) due to texture evolution. Once transformation occurs, the $\gamma-$ austenite and α'- martensite crystal volume content decreased and increased respectively during the deformation process due to transformation. As such, each ODF figure was plotted with a different number of crystal orientations. After 20% strain, a significant strengthening in orientation intensity (i.e. the number of crystals occurring at that orientation) is observed at ($\varphi_1 = 50°, \Phi = 45°, \varphi_2 = 0°$) and ($\varphi_1 = 40°, \Phi = 90°, \varphi_2 = 45°$) for the austenite phase (Table 12). This phenomenon continues for the entirety of the deformation (up to 40% strain). With the volume fraction of austenite decreasing as a function deformation, these orientations can represent a set of orientations that do not promote transformation for the given microstructure and slip hardening rates of DSS.

Table 11: Uniaxial tension $\rho = -0.5$ along RD α- ferrite texture at a) 0% b) 10% c) 20% d) 30% e) 40% effective strain

Effective Strain	$\alpha -$Phase Texture				
a). 0% Strain Volume Fraction 65%					
b). 10% Strain Volume Fraction 65%					
c). 20% Strain Volume Fraction 65%					
d). 30% Strain Volume Fraction 65%					
e). 40% Strain Volume Fraction 65%					
Φ φ_2	$\varphi_2 = 0°$	$\varphi_2 = 30°$	$\varphi_2 = 45°$	$\varphi_2 = 60°$	
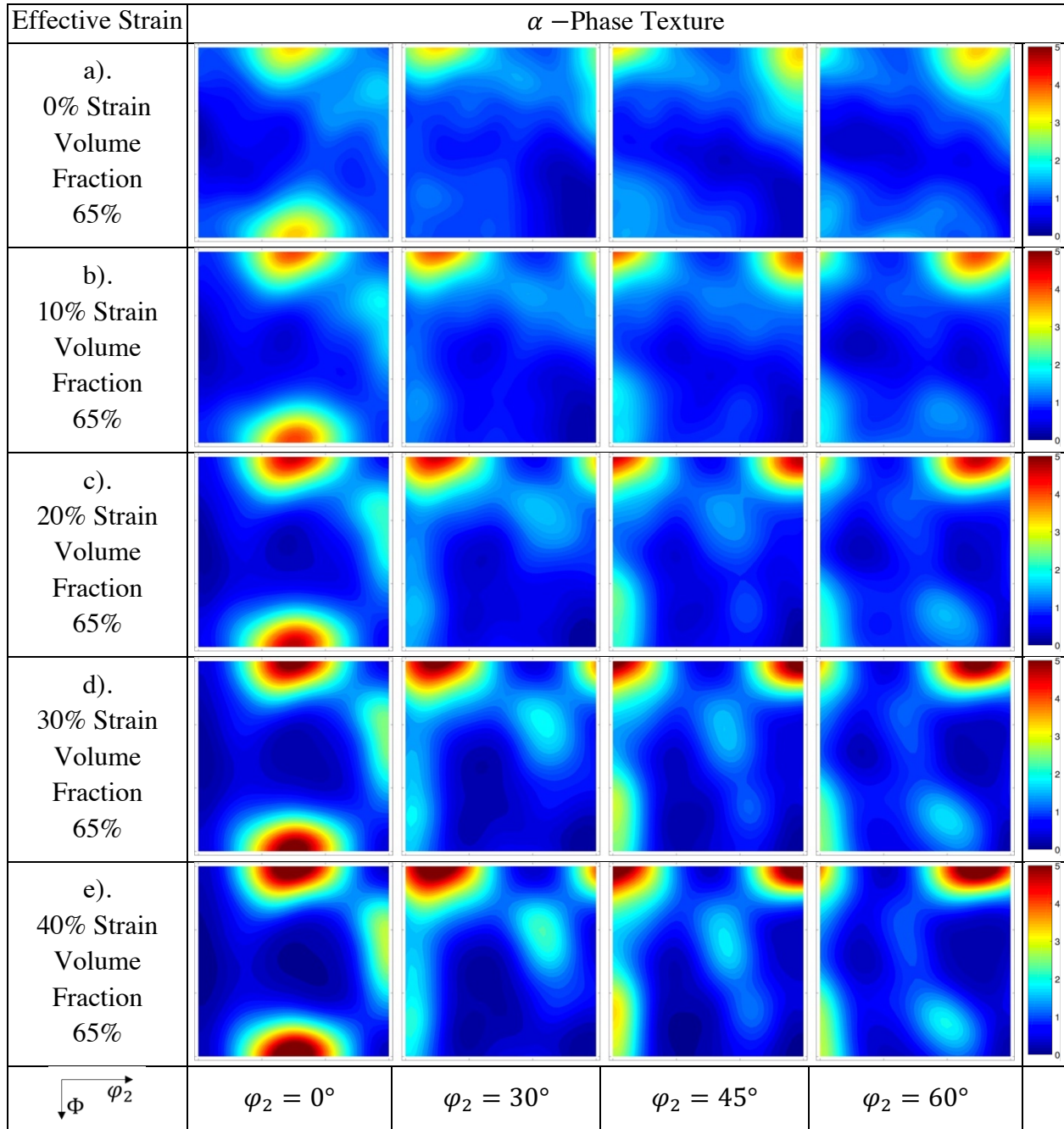
Table 12: Uniaxial tension $\rho = -0.5$ along RD γ- austenite texture at a) 0% b) 10% c) 20% d) 30% e) 40% effective strain
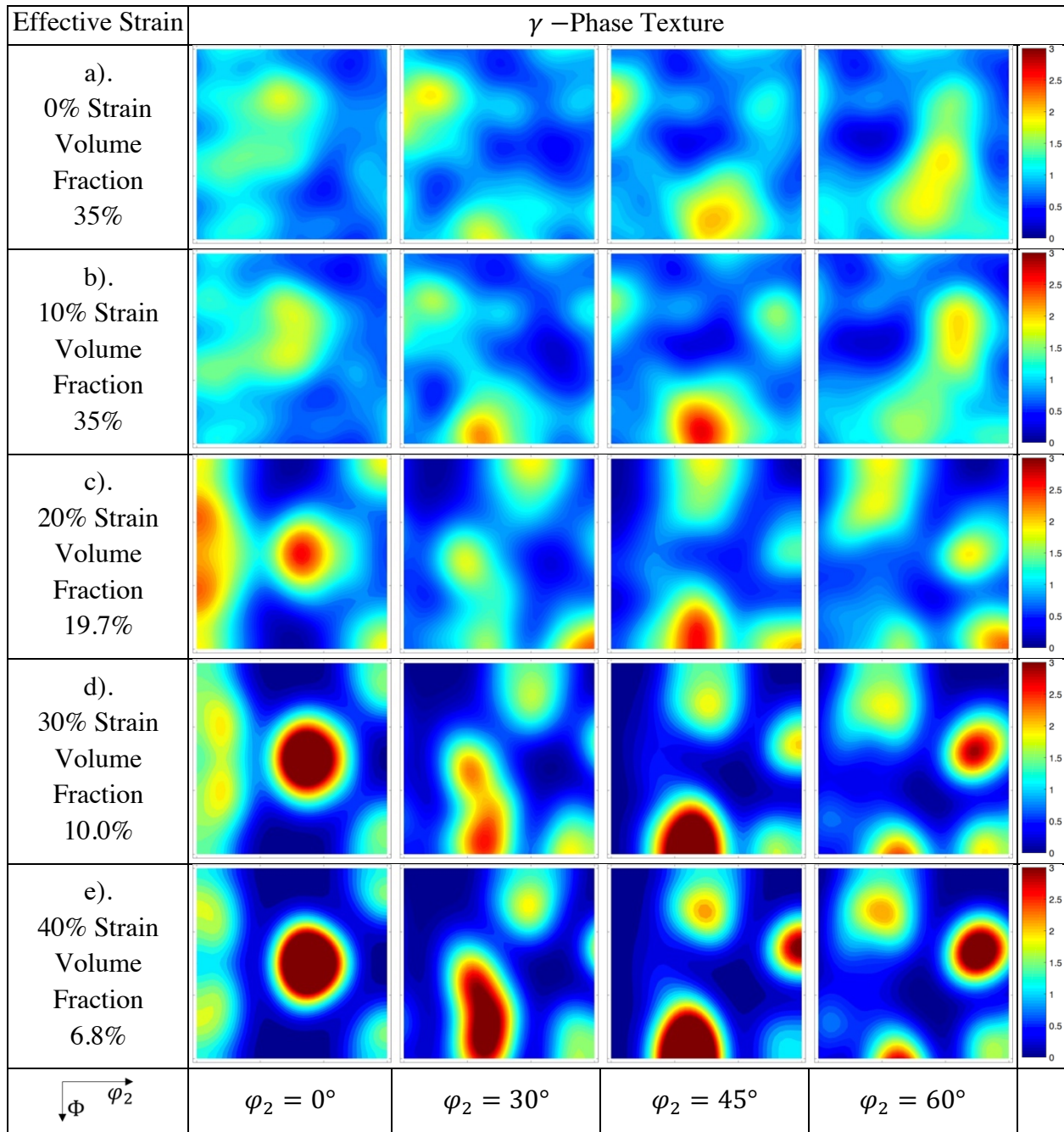
Effective Strain	γ −Phase Texture			
a). 0% Strain Volume Fraction 35%				
b). 10% Strain Volume Fraction 35%				
c). 20% Strain Volume Fraction 19.7%				
d). 30% Strain Volume Fraction 10.0%				
e). 40% Strain Volume Fraction 6.8%				
Φ φ_2	$\varphi_2 = 0°$	$\varphi_2 = 30°$	$\varphi_2 = 45°$	$\varphi_2 = 60°$

Table 13: Uniaxial tension $\rho = -0.5$ along RD α'- martensite texture at a) 20% b) 30% c) 40% effective strain

Effective Strain	α' −Phase Texture				
a). 20% Strain Volume Fraction 15.3%					
b). 30% Strain Volume Fraction 25.0%					
c). 40% Strain Volume Fraction 28.2%					
Φ φ_2	$\varphi_2 = 0°$	$\varphi_2 = 30°$	$\varphi_2 = 45°$	$\varphi_2 = 60°$	
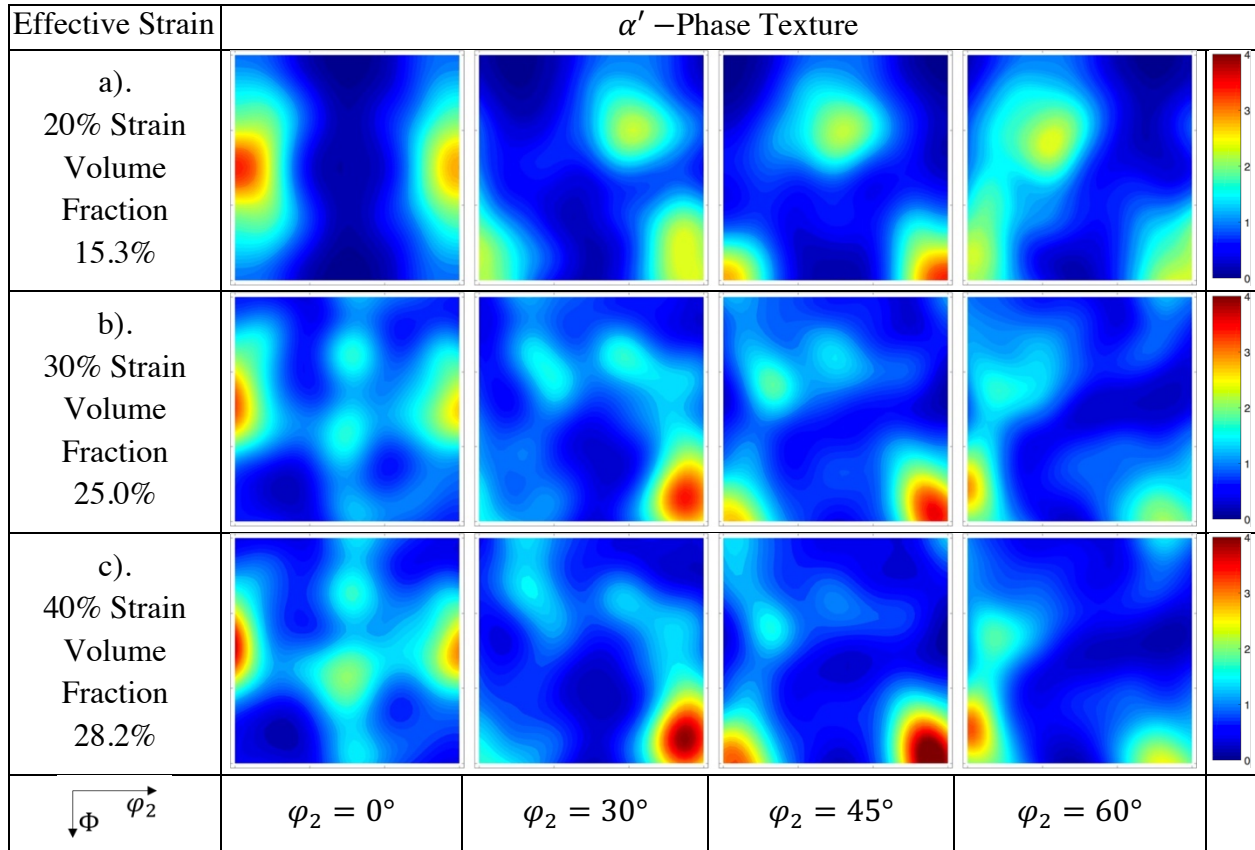
7.2.1.2 Schmid Factor Analysis of Uniaxial Tension in Rolling Direction

In literature, it has been reported that grains that exhibit high Schmid factor (SF) are favourable for transformation. Schmid factor is a scalar term that determines a crystal planes resistance to dislocation slip for a given applied stress tensor, such that

$$SF = \boldsymbol{P}:\boldsymbol{\sigma} = P_{ij}\sigma_{ij} \qquad\qquad (\quad 7.1 \quad)$$

where $\boldsymbol{\sigma}$ is the applied stress tensor that is normalized along the major direction. A high Schmid factor corresponds to an orientation that is favourable for slip (i.e. lower deformation to induce plastic slip). As a result, lower Schmid factor crystals will have high magnitudes of stress due to elastic loading. *Seo et al.* [214] performed experimental EBSD measurements and analyzed the Schmid factor of austenite crystals that transformed to martensite in a duplex steel. They reported that the majority of austenite crystals that transformed to martensite during uniaxial tension had a Schmid factor of greater than 0.46 at 20% strain.

With this observation in mind, a Schmid factor analysis was performed to identify key characteristics of transformation that is related to texture. Three Schmid factor analyses were performed:

1) Highest Schmid Factor amongst austenite crystal slip systems: $P_{ij} = \frac{1}{2} s_i m_j + \frac{1}{2} m_i s_j$

2) Highest Schmid Factor amongst austenite habit plane systems: $P_{ij} = \frac{1}{2} s_i^{HP} m_j^{HP} + m_i^{HP} s_j^{HP}$

3) Second highest Schmid Factor amongst austenite habit planes systems

The transformation criteria required that the stress on two fault bands must exceed the transformation threshold, Γ^{th}. Thus, the second highest Schmid factor of each austenite crystal is of interest. In each study, all crystals are binned within 0.01 increments of their initial Schmid factor. Although the Schmid factor can evolve with deformation, many aspects of the texture studied strengthened rather than rotated during uniaxial tension. Thus, the initial Schmid factor is assumed to be comparable to the final Schmid factor; however, this is not generally true. All transformed crystals are tracked and the strain at which they transform are also binned accordingly to determine when transformation occurred. Figure 29 - Figure 31 presents a histogram of the Schmid factor analysis for the three factors studied. It is important to note that ~30% of the total austenite phase (85% of all austenite crystals) have a Schmid factor greater than 0.44 in this material. In agreement with literature, a significant volume fraction of austenite crystals with a Schmid factor greater than 0.44 transformed. However, a significant proportion of these crystals transformed at ~20% strain. Furthermore, the percentage of austenite crystals with a lower Schmid factor (less than 0.40) transformed was higher, such that most crystals (if not all within the bin) transformed. In addition, austenite crystals with a low Schmid factor generally transformed the earliest. This is a result of the transformation criteria being stress-based where austenite crystals with a lower Schmid factor generate higher stress that is needed to transform. Functionally, the Schmid factor and resolved shear stress are functionally similar (comparing Equation 4.28 and 7.1). This means that higher Schmid factor habit planes should be favourable for transformation earlier in deformation. Yet, the Schmid factor of the first and second highest habit planes show similar trends where lower Schmid factor habit planes transformed the earliest; the second highest Schmid factor showed concentrations of values between 0.33 and 0.40. Thus, there exists a competition between the stress projected on the habit plane and the total stress developed within

the crystal. It should be mentioned that the austenite crystal group with the highest Schmid factor had the highest proportion of crystals that did not transform. Other experimental studies have observed that high SF crystals do not necessarily transform at all due to the influence of shape and morphology on austenite stability [215].
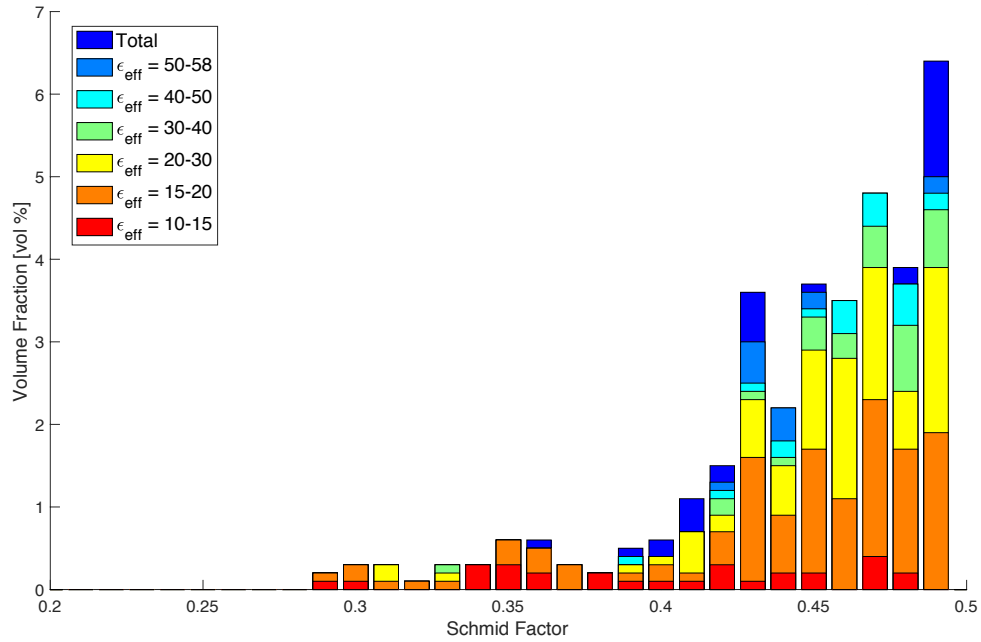
Figure 29: Highest Schmid factor for dislocation slip systems of γ-austenite crystals under uniaxial tension in RD
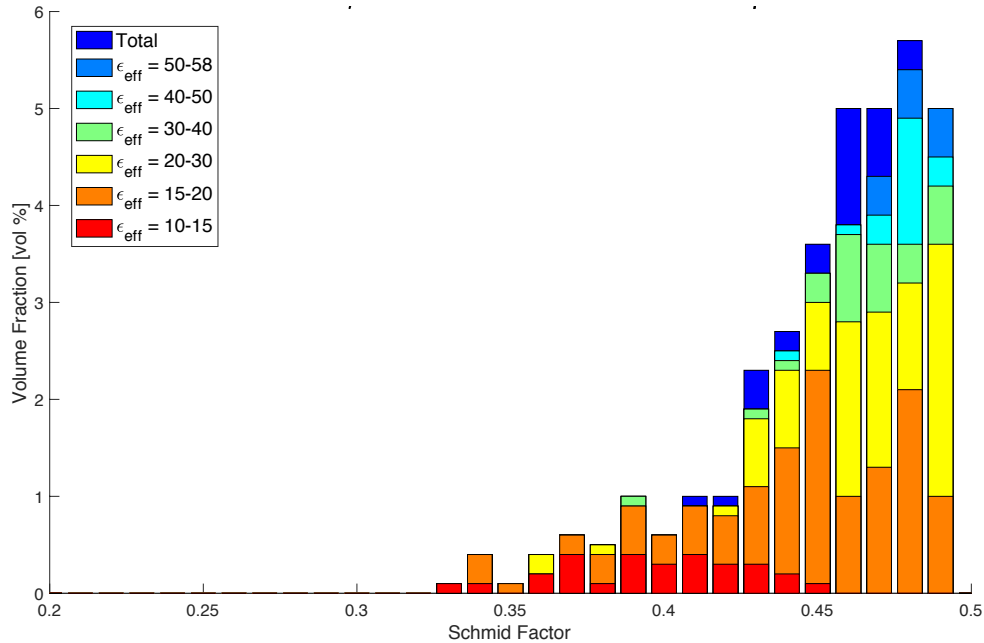
Figure 30: Highest Schmid factor for Habit Planes of γ-austenite crystals under uniaxial tension in RD
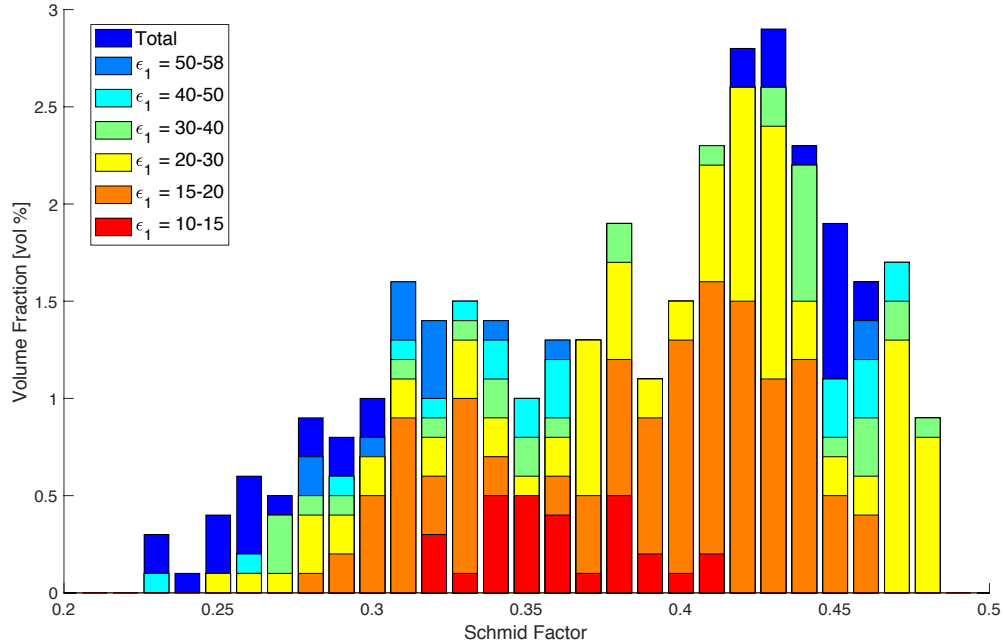
Figure 31: Second Highest Schmid factor for Habit Planes of γ-austenite crystals under uniaxial tension in RD

As mentioned above, crystals with generally low Schmid factor on the dislocation planes exhibited earlier transformation while some did not transform at all. Furthermore, many of the austenite crystals that transformed earliest had a Schmid factor between 0.33 and 0.40 on the second highest habit plane. To gain additional insight into why some crystals transform earlier than others, the resolved shear stress evolution is studied four austenite crystals during uniaxial tension in the RD. Table 14 summarizes these four crystals and were selected as follows:

1) An austenite crystal with a Schmid factor between 0.33 and 0.40 on the second highest habit plane that transformed early (< 15% strain)
2) An austenite crystal with a Schmid factor between 0.33 and 0.40 on the second highest habit plane that transformed later (> 40% strain)
3) An austenite crystal with a low Schmid factor (< 0.30) on the second highest habit plane
4) An austenite crystal with a high Schmid factor (> 0.40) on the second highest habit plane

Table 14: Austenite Crystals Analyzed for Critical Shear Stress on Habit Planes for Transformation

Crystal Number	Schmid Factor (2nd Largest on HP)	φ_1 [°]	Φ [°]	φ_2 [°]	Strain at Transformation
1	0.359	-71.5	32.5	103.0	0.13
2	0.363	91.4	39.2	-107.0	0.56
3	0.253	85.0	44.0	-112.2	N/A
4	0.463	117.2	22.5	-120.5	N/A

Figure 32 presents the shear stress and transformation threshold evolution on the habit planes with respect to strain for the four crystals studied. Crystal #1 had a Schmid factor of 0.359 that transformed at ~13% strain. The resolved shear stress on the fault band system loaded up elastically; this generated a rapid increase in stress that was necessary for transformation. However, Crystal #2 had a similar Schmid factor (0.363), yet transformed at ~56% strain. As the shear stress on the fault band begins to increase, plastic flow begins to dominate the deformation and reduces further building of stress on the habit planes. At 22% strain, the hardening saturates and began to soften due to texture rotation. As the crystal rotates, the habit planes also rotate away from a favorable position. Eventually, a new fault band becomes more active at a strain of 34% where the shear stress begins to increase until transforming at 56% strain. This is an excellent example highlighting that although some crystals may be primed for transformation, texture evolution can influence whether a crystal transforms. However, if the transformation threshold had been lowered by ~13 MPa, this crystal would have transformed at 22% strain; this leads to an abrupt change that is discontinuous in the strain at which crystals transform due to transformation threshold. Crystal #3 and #4 had a Schmid factor of 0.253 and 0.463 respectively. Neither crystal reached the critical threshold that was necessary for transformation. Again, this can be caused a soft crystal orientation causing the stress tensor to saturate at a low stress level from plastic slip.
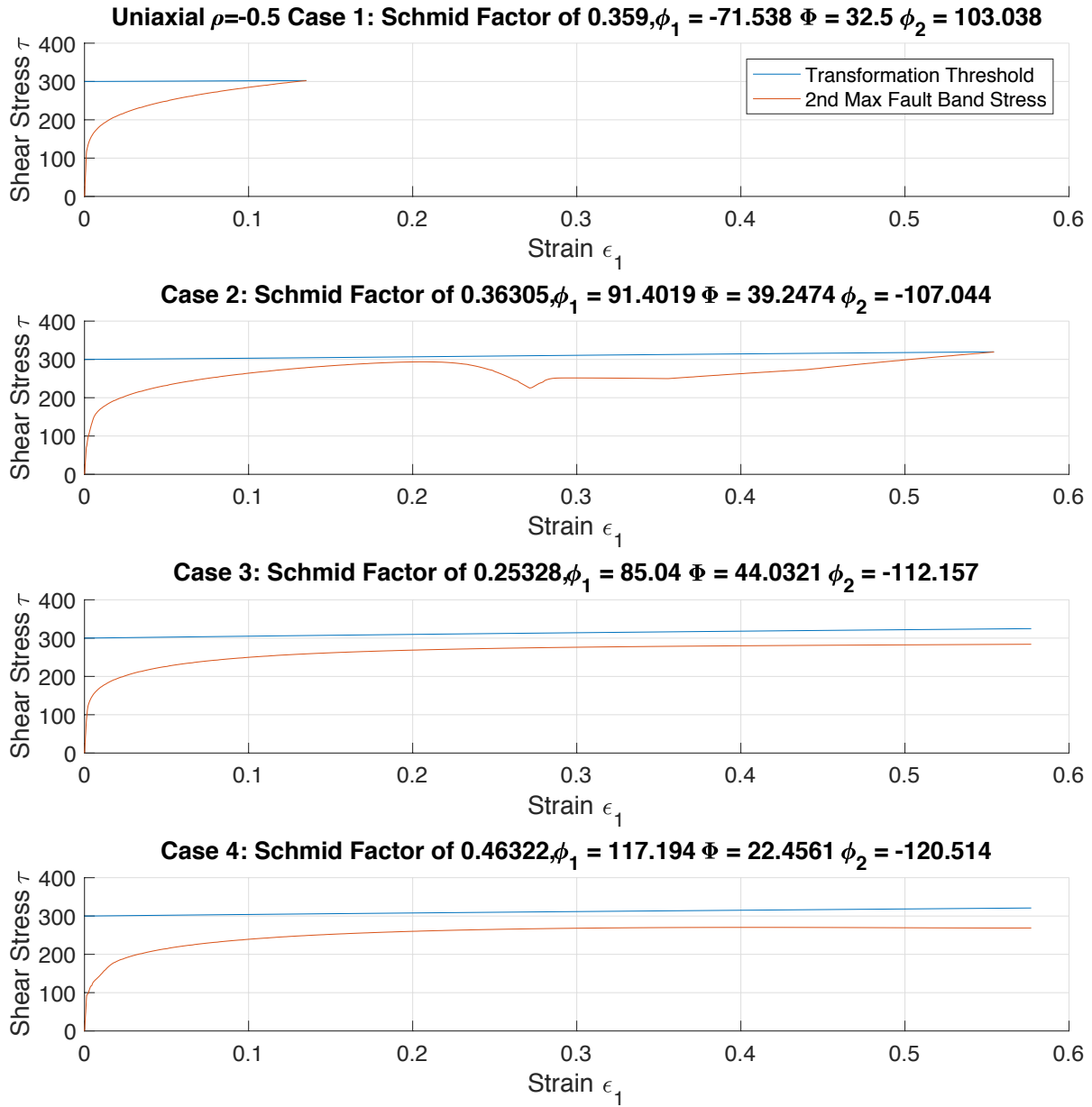
Figure 32: Plot of fault band shear stress and transformation threshold with respect to strain for the four crystals

7.2.1.3   Uniaxial Tension along the Transverse Direction

To investigate the influence of texture on martensite, simulations are performed where the loading direction is along the transverse direction. This is accomplished by rotating the crystal texture by 90° ($\varphi_1 = \varphi_1 + 90°$) about the normal direction (ND). Table 15 and Table 16 presents the simulated texture and volume fraction evolution of γ- austenite and α'- martensite phases respectively. The rotated texture of the γ–austenite shows a similar weak texture of brass ($\varphi_1 = 35°, \Phi = 45°, \varphi_2 = 0°$) and copper ($\varphi_1 = 90°, \Phi = 35°, \varphi_2 = 45°$) initially as compared to the RD texture. As a result, the resultant texture of UA in the TD for both γ– austenite at 40% strain shows remarkable similarity to that of UA in the RD; High intensity texture components formed and strengthened at nearly identical locations at ($\varphi_1 = 50°, \Phi = 45°, \varphi_2 = 0°$) and ($\varphi_1 = 40°, \Phi = 90°, \varphi_2 = 45°$) for the austenite phase. Although the final textures are similar, the final martensite volume fraction was 6.8% at 40% strain deformation in the TD (compared to 8.6% in RD). This highlights that other texture variants have become more favourable for transformation due to directional changes, yet the concentrated rotated brass ($\varphi_1 = 50°, \Phi = 45°, \varphi_2 = 40°$), copper ($\varphi_1 = 90°, \Phi = 35°, \varphi_2 = 45°$) and minor cube texture components remain. *Gey et al.* [216] showed that the rate of transformation with respect to crystal orientation, where they noted that cube- and Goss- oriented γ grains transformed less in 304 stainless steel at low temperatures for their material.

Table 15: Uniaxial tension $\rho = -0.5$ along TD γ- austenite texture at a) 0% b) 10% c) 20% d) 30% e) 40% effective strain

c). 20% Strain Volume Fraction 22.0%				
d). 30% Strain Volume Fraction 12.4%				
e). 40% Strain Volume Fraction 8.6%				
Φ φ_2	$\varphi_2 = 0°$	$\varphi_2 = 30°$	$\varphi_2 = 45°$	$\varphi_2 = 60°$
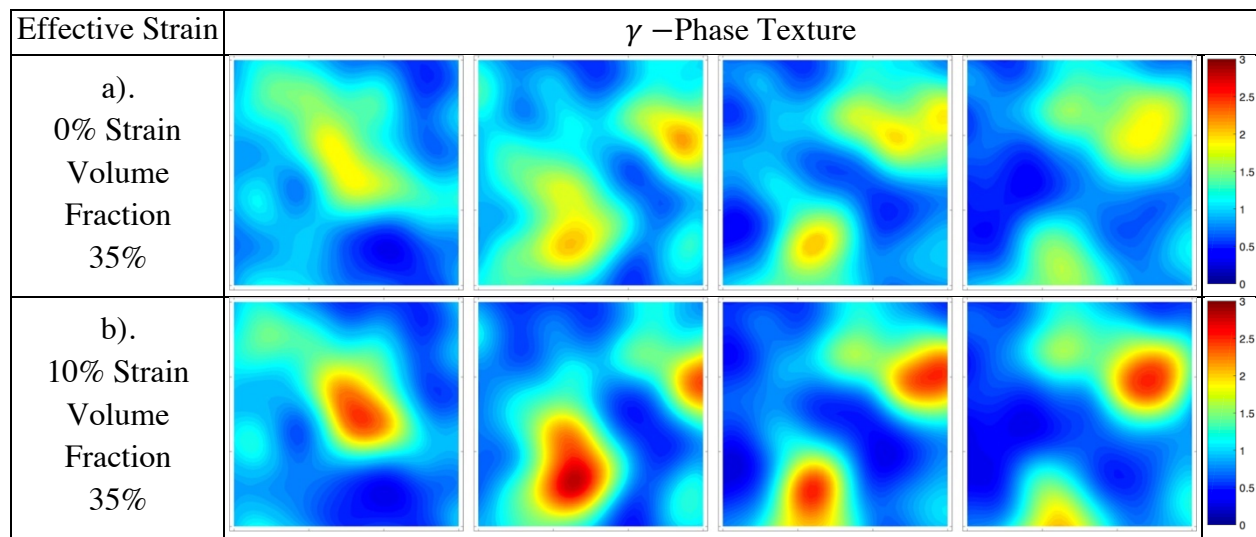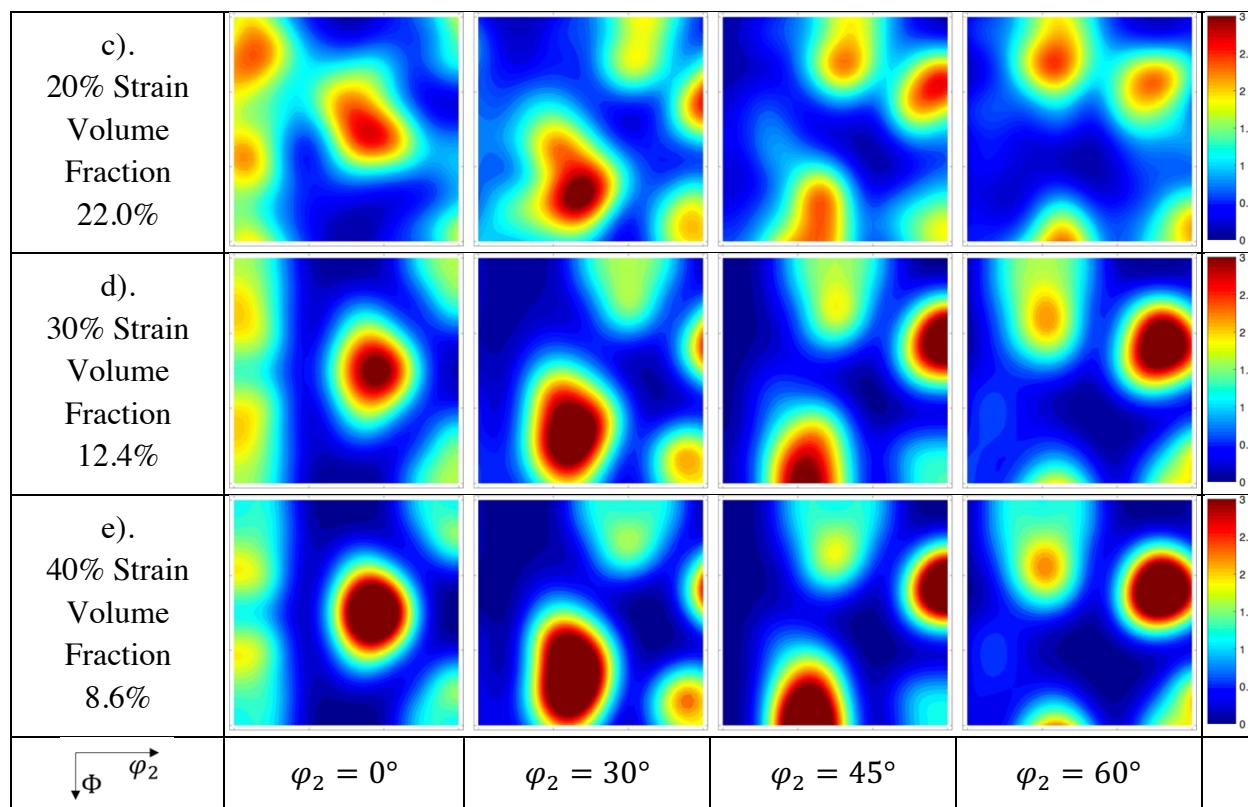
Table 16: Uniaxial tension $\rho = -0.5$ along TD α'- martensite texture at a). 20% b). 30% c). 40% effective strain

Effective Strain	$\alpha'-$Phase Texture			
a). 20% Strain Volume Fraction 15.3%				
b). 30% Strain Volume Fraction 25.0%				

75

c). 40% Strain Volume Fraction 28.2%					
Φ φ_2	$\varphi_2 = 0°$	$\varphi_2 = 30°$	$\varphi_2 = 45°$	$\varphi_2 = 60°$	
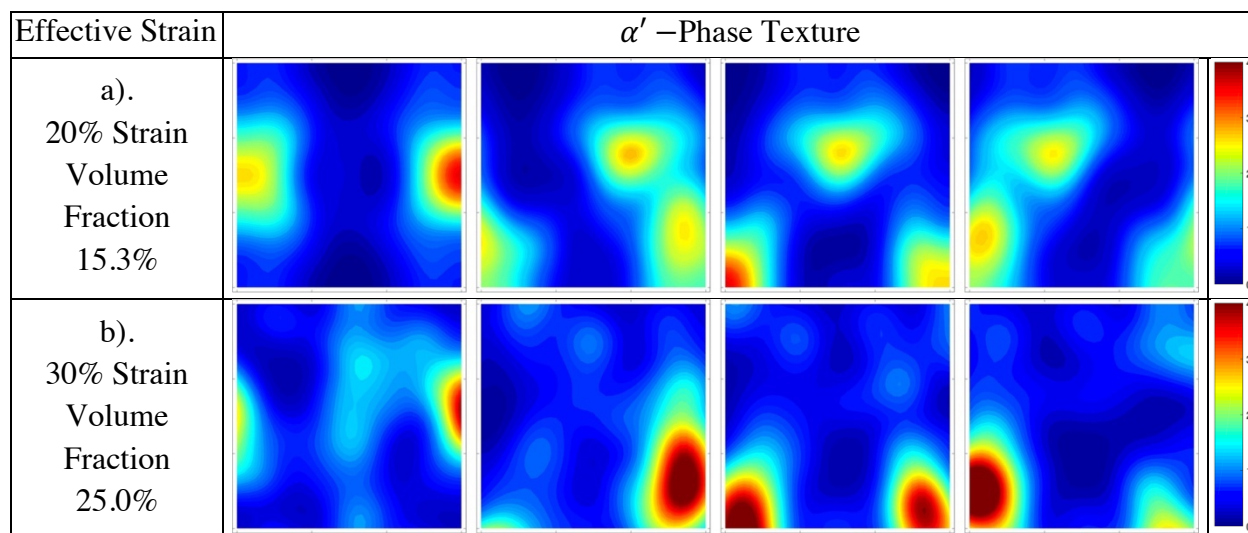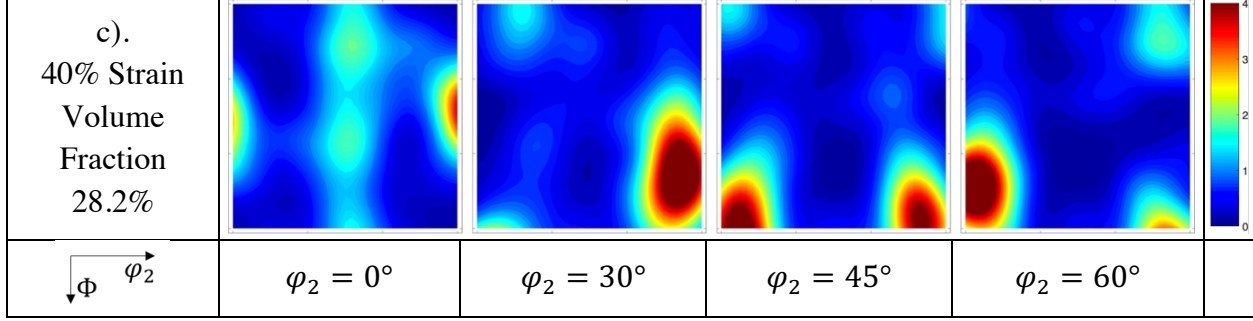
7.2.2   *Plane Strain* ($\rho = 0.0$) *and Biaxial Stretching* ($\rho = 1.0$)

It has been shown that the volume fraction evolution of austenite to martensite has a notable sensitivity to changing stress triaxiality [217] [218] [219] [220] [221], such that martensite evolution increases with an increase in triaxiality, Σ. Therefore, two additional strain paths are simulated and studied: in-plane strain tension ($\rho = 0.0, \Sigma = 0.58$) and biaxial stretching ($\rho = 1.0, \Sigma = 0.66$). These strain paths are also critical strain paths for evaluating formability. To compare the evolution of martensite with respect to deformation for different strain paths, the effective strain, ε_{eff}, is defined as

$$\varepsilon_{eff} = \sqrt{\frac{2}{3}\varepsilon'_{ij}\varepsilon'_{ij}}$$

(7.2)

where ε'_{ij} is the deviatoric strain defined as $\varepsilon'_{ij} = \varepsilon_{ij} - \frac{1}{3}\varepsilon_{kk}\delta_{ij}$. Figure 33 presents the volume fraction evolution of martensite with respect to effective strain for plane strain and biaxial tension. The martensite evolution during uniaxial tension ($\Sigma = 0.33$) is also presented for comparison. Simulations show a positive trend of triaxiality on martensite volume fraction evolution that agrees with observations in literature. This difference in volume fraction evolution is captured by the rate of accumulated shear strain on all slip systems (Equation 4.27).
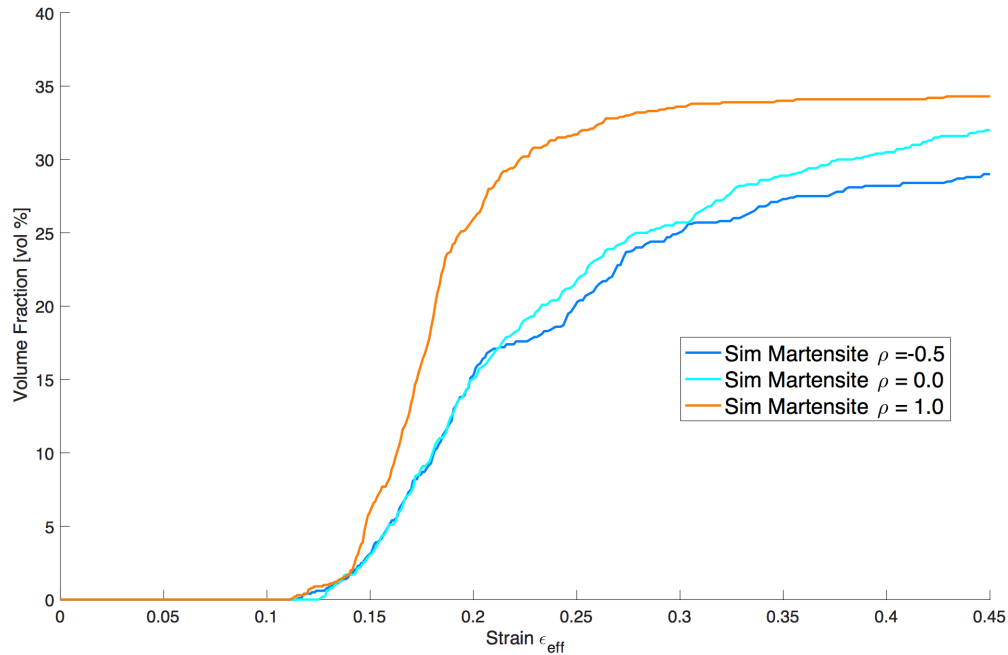
Figure 33: Martensite volume fraction vs effective strain for different loading conditions

Table 17 presents the resultant textures of plane strain and biaxial loading for γ- austenite at 40% effective strain. The resulting ODF for uniaxial tension is also presented for comparison. For the complete texture evolution history, please refer to APPENDIX A.1-A.2. For γ- austenite at 40% effective strain, different loading conditions produced varying austenite crystal volume fractions from 6.8% to 0.9%. It should be noted that each ODF is unremarkable, such that only minor similar in clustering of orientation intensity was observed. Table 18 presents a summary of the remaining high intensity orientations that did not promote transformation.

Table 17: Comparing different loading condition at 40% effective strain of γ-austenite texture

Effective Strain	γ −Phase Texture			
Initial Texture 0% Strain Volume Fraction 35%				

Uniaxial RD $\rho = -0.5$ 40% Strain Volume Fraction 6.8%				
Plane Strain $\rho = 0.0$ 40% Strain Volume Fraction 4.2%				
Equi-biaxial $\rho = 1.0$ 40% Strain Volume Fraction 0.9%				
Φ φ_2	$\varphi_2 = 0°$	$\varphi_2 = 30°$	$\varphi_2 = 45°$	$\varphi_2 = 60°$
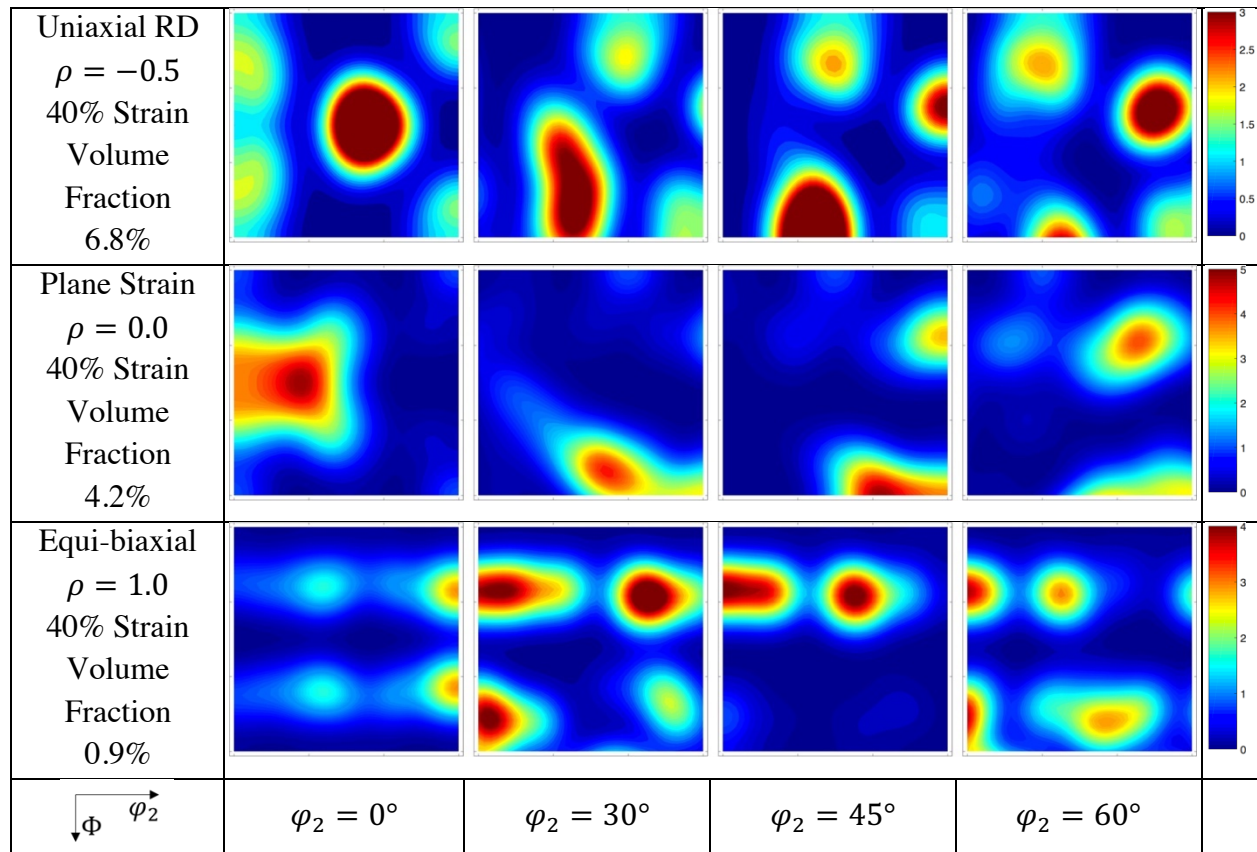
Table 18: Summary of remaining high intensity orientations that did not promote transformation in austenite

Uniaxial Tension $\rho = -0.5$	Plane Strain Tension $\rho = 0.0$	Equi-biaxial Tension $\rho = 1.0$
$\varphi_1 = 50°, \Phi = 45°, \varphi_2 = 0°$	$\varphi_1 = 30°, \Phi = 30°, \varphi_2 = 0°$	
$\varphi_1 = 40°, \Phi = 90°, \varphi_2 = 45°$	$\varphi_1 = 60°, \Phi = 90°, \varphi_2 = 45°$	$\varphi_1 = 50°, \Phi = 45°, \varphi_2 = 30° - 60°$
$\varphi_1 = 40°, \Phi = 75°, \varphi_2 = 60°$	$\varphi_1 = 40°, \Phi = 75°, \varphi_2 = 60°$	

Table 19 presents the resultant textures of plane strain and biaxial loading for α'- martensite at 40% effective strain. The resulting ODF for uniaxial tension is also presented for comparison. For the complete texture evolution history, please refer to APPENDIX A.1-A.2. Interestingly, the ODF of α'- martensite at 40% effective strain shows similar common texture components for all strain paths studied; even though the parent γ- austenite texture had vastly different resulting ODFs. Martensite showed common orientations at ($\varphi_1 = 0°/90°, \Phi = 45°, \varphi_2 = 0°$) and ($\varphi_1 = 80°, \Phi = 45°, \varphi_2 = 0°$) with the spread and intensities showing some deviation.

Table 19: Comparing different loading condition at 40% effective strain of α'- martensite texture

Effective Strain	$\alpha'-$Phase Texture				
Uniaxial RD $\rho = -0.5$ 40% Strain Volume Fraction 28.2%					
Plane Strain $\rho = 0.0$ 40% Strain Volume Fraction 30.8%					
Equi-biaxial $\rho = 1.0$ 40% Strain Volume Fraction 34.1%					
Φ φ_2	$\varphi_2 = 0°$	$\varphi_2 = 30°$	$\varphi_2 = 45°$	$\varphi_2 = 60°$	
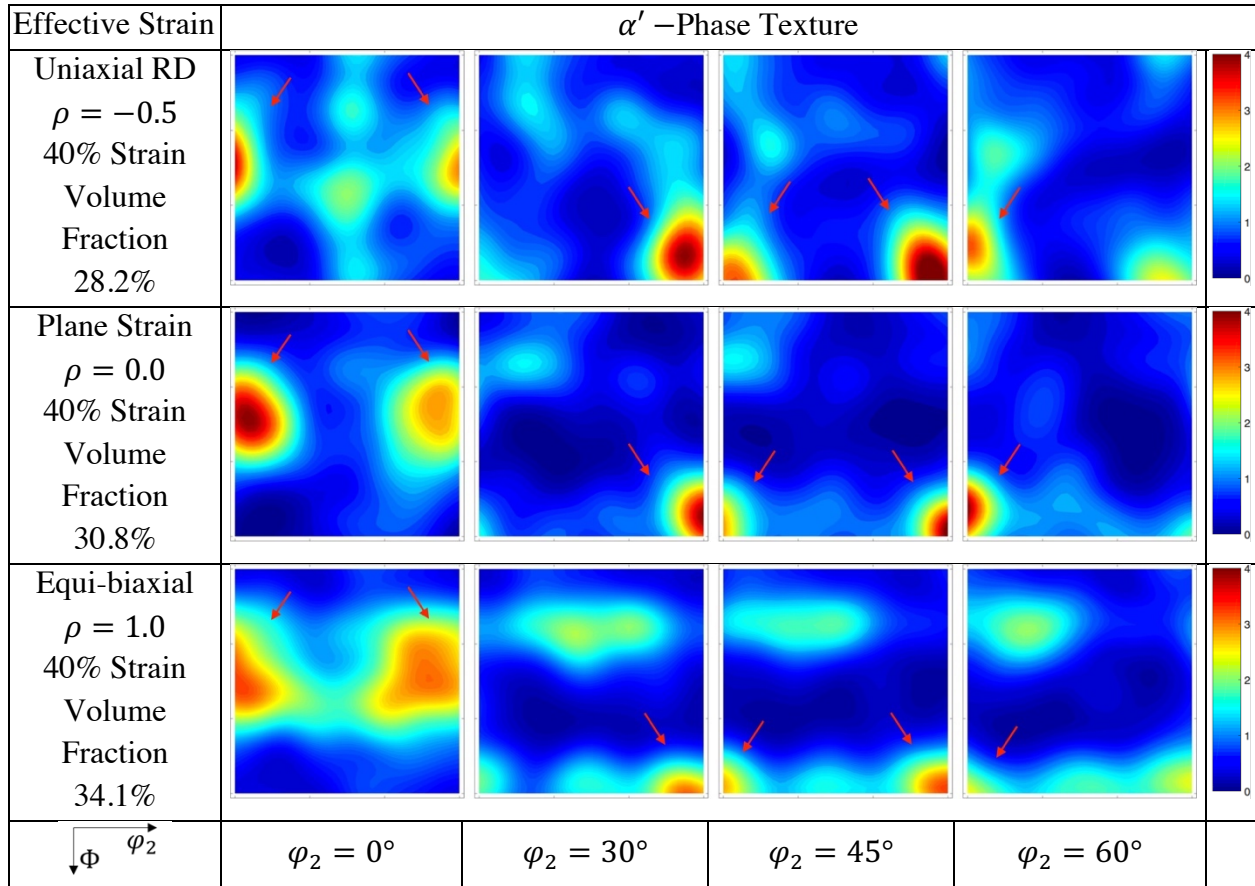
7.2.2.1 Schmid Factor Analysis of Plane Strain and Biaxial Strain Paths

Similar to the method presented earlier, a Schmid factor analysis was performed for plane strain with $\rho = 0.0$ and equi-biaxial tension with $\rho = 1.0$. The stress tensor was calculated from each simulation and normalized for each Schmid factor calculation. Figure 34 - Figure 39 presents the highest Schmid factor for dislocation, first and second highest Schmid factor on the fault band habit planes during plane strain and equi-biaxial tension respectively.

For plane strain, all the austenite crystals that transformed between 10-15% effective strain had a SF of 0.30 or less. Similarly, the majority of crystals with the lowest relative Schmid factor transformed before 15% strain during biaxial loading. Comparing the spread of initial Schmid factor for plane strain ($\rho = 0.0$) and equi-biaxial tension with ($\rho = 1.0$), the distribution of SF shift towards higher SF as ρ increases. This indicates that more habit planes are favourable for

79

transformation, which was observed previously in the volume fraction evolution of martensite (Figure 33).
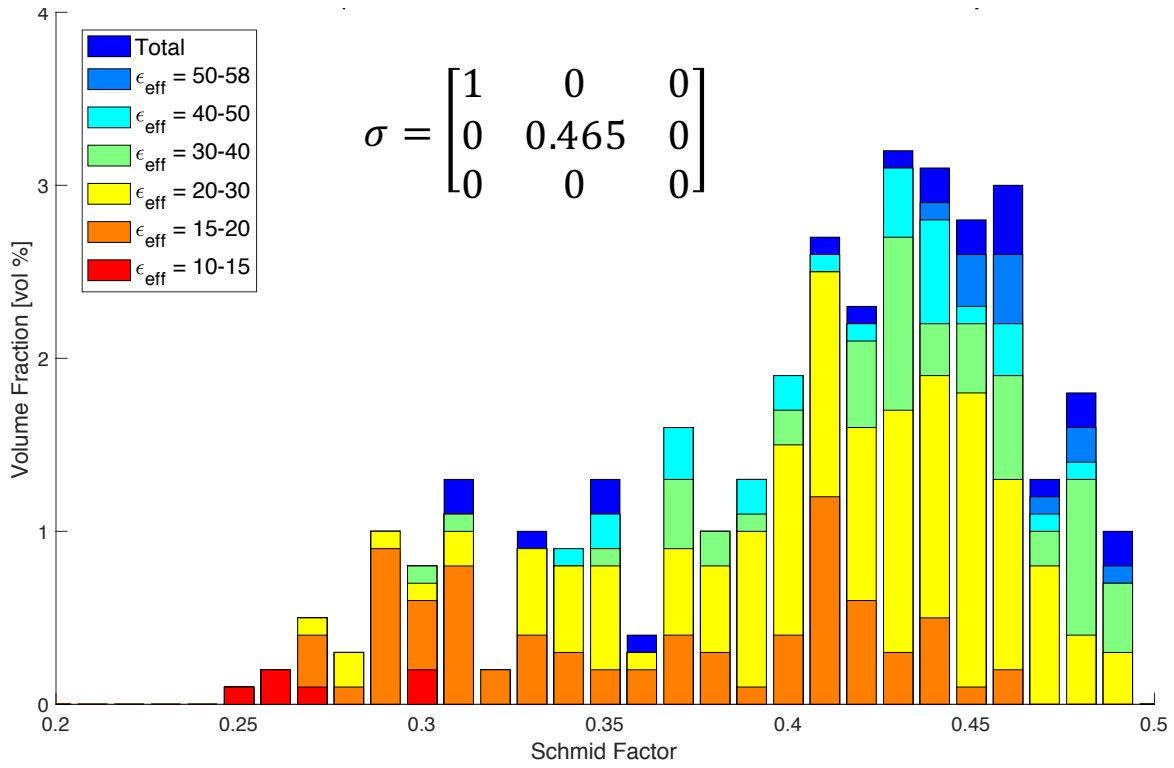
Figure 34: Highest Schmid factor for dislocation slip systems of γ-austenite crystals under plane strain tension in RD
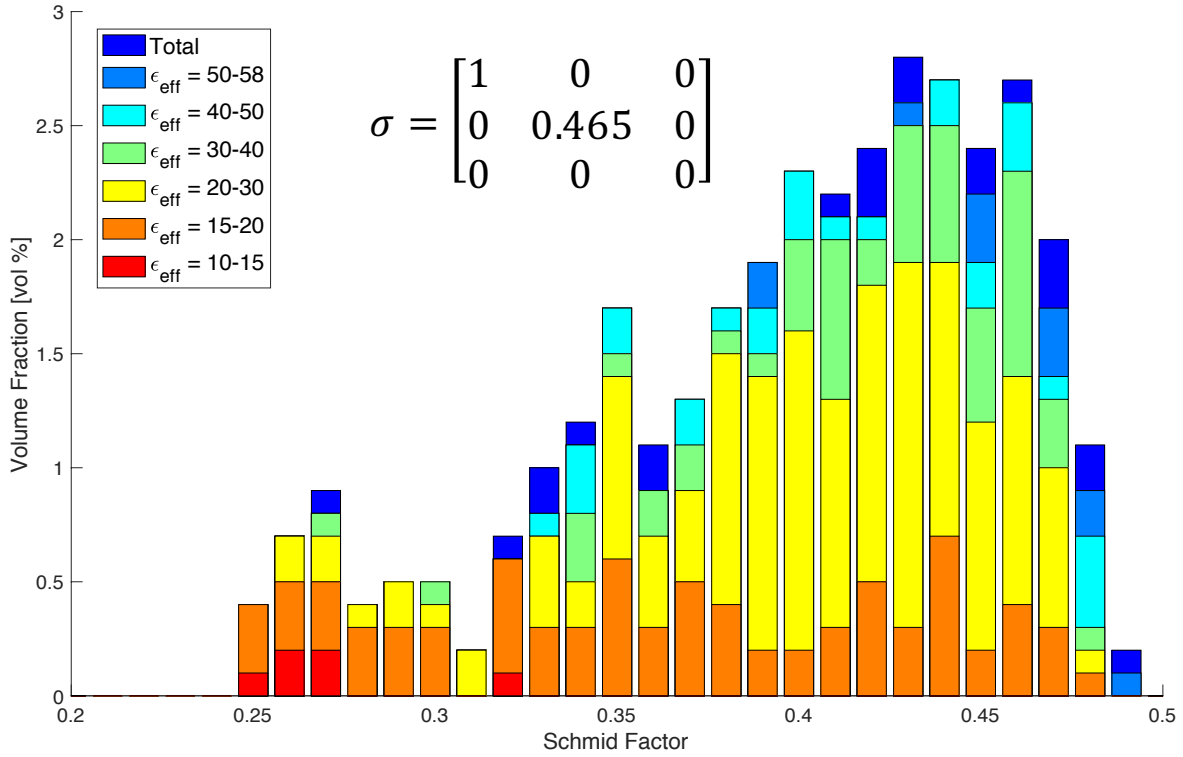
Figure 35: Highest Schmid factor for Habit Planes of γ-austenite crystals under plane strain tension in RD
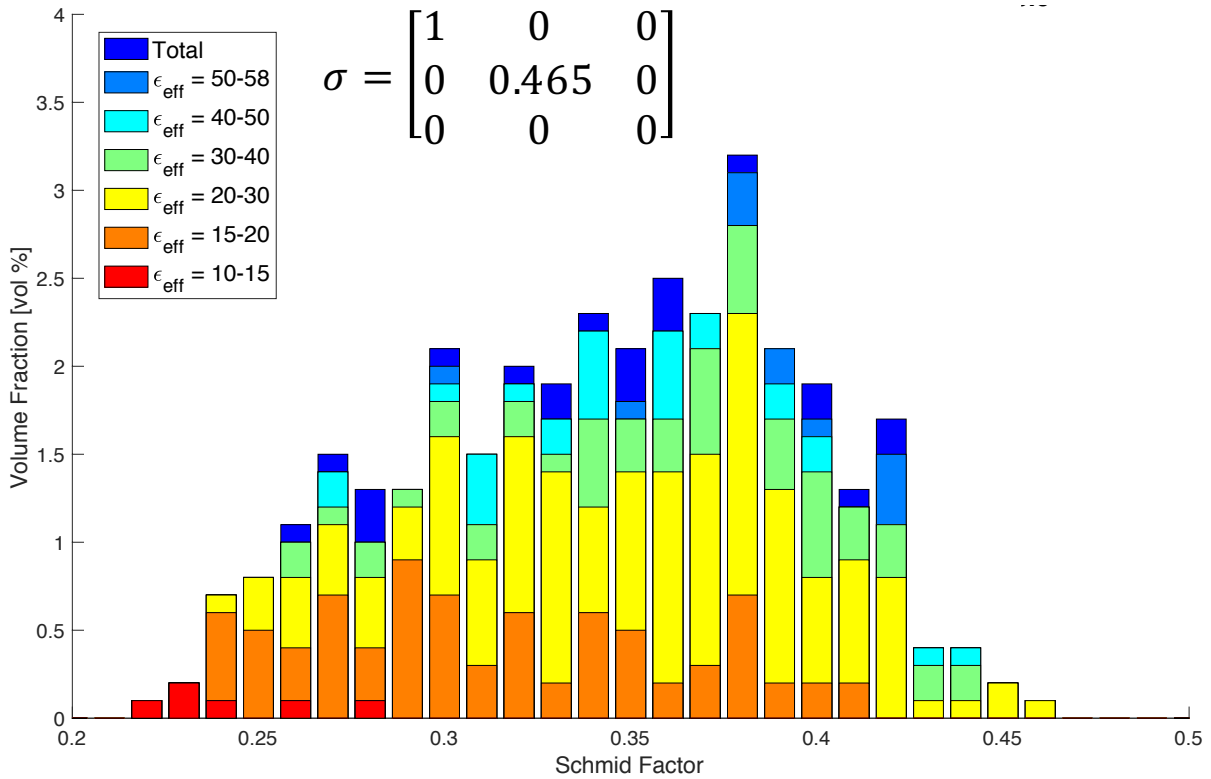
Figure 36: Second highest Schmid factor for Habit Planes of γ-austenite crystals under plane strain tension in RD
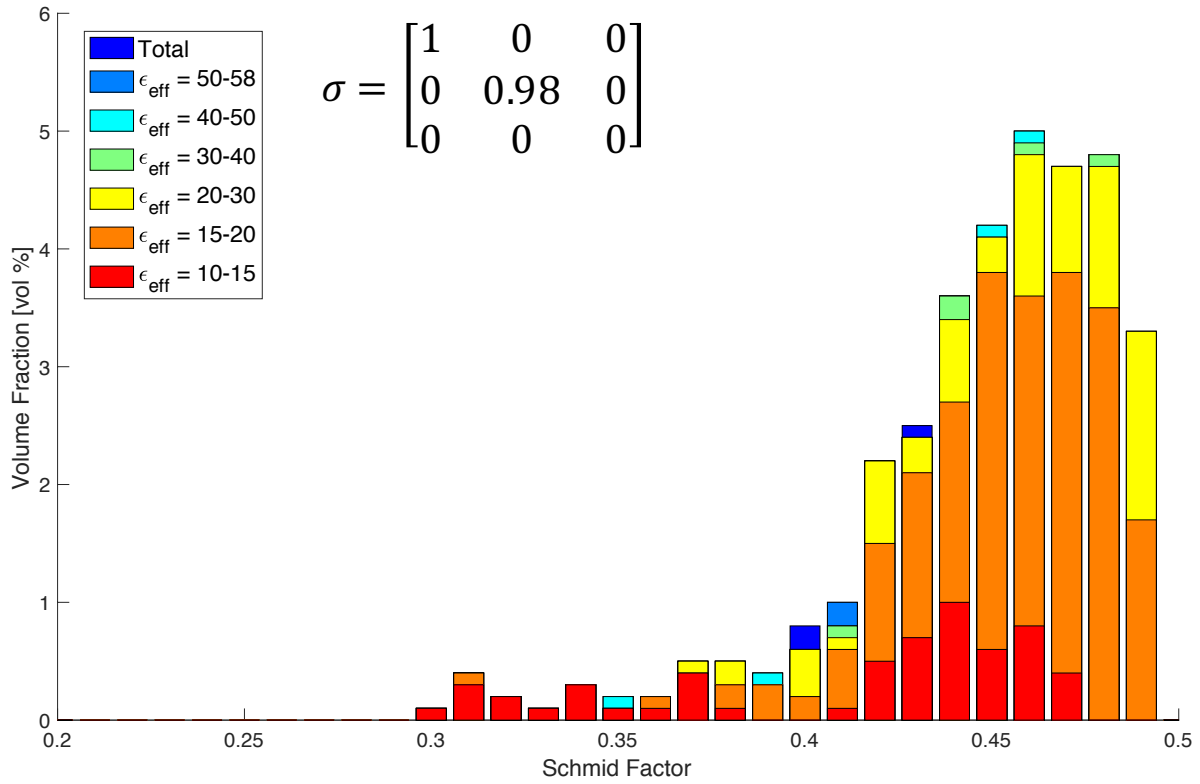
Figure 37: Highest Schmid factor for dislocation slip systems of γ-austenite crystals under biaxial tension in RD

$$\sigma = \begin{bmatrix} 1 & 0 & 0 \\ 0 & 0.98 & 0 \\ 0 & 0 & 0 \end{bmatrix}$$
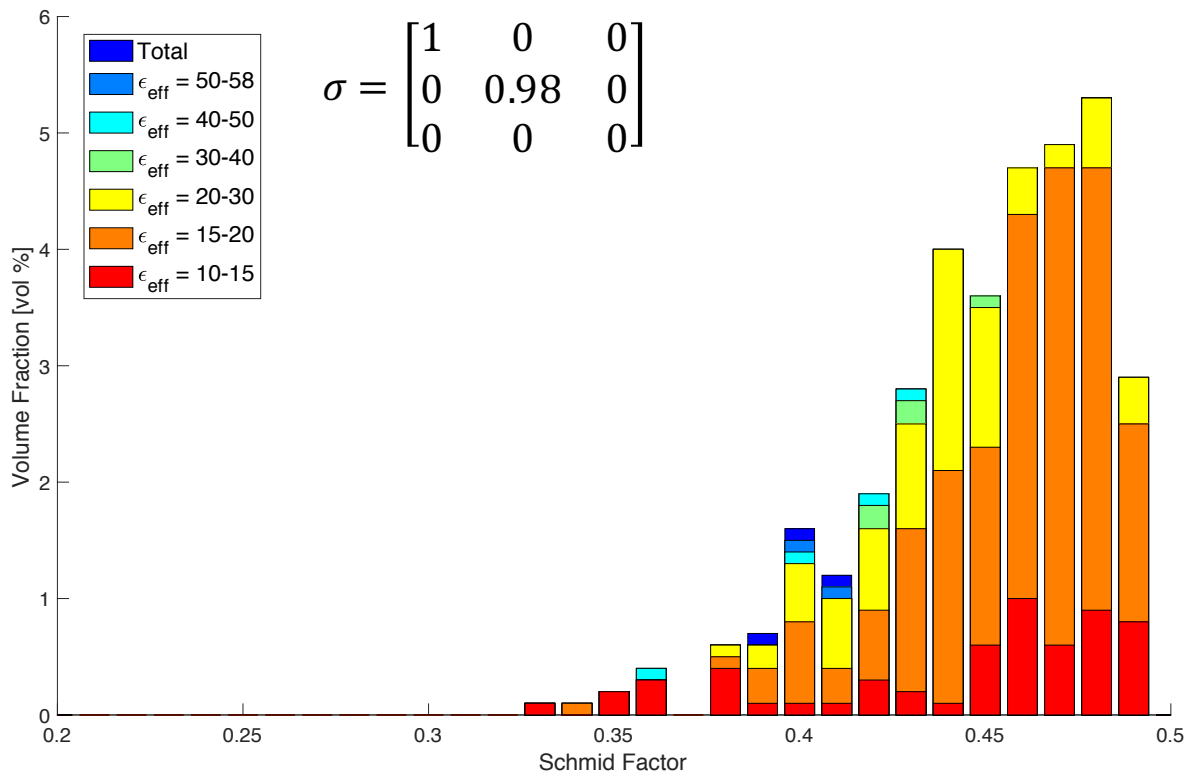
Figure 38: Highest Schmid factor for Habit Planes of γ-austenite crystals under biaxial tension in RD

$$\sigma = \begin{bmatrix} 1 & 0 & 0 \\ 0 & 0.98 & 0 \\ 0 & 0 & 0 \end{bmatrix}$$
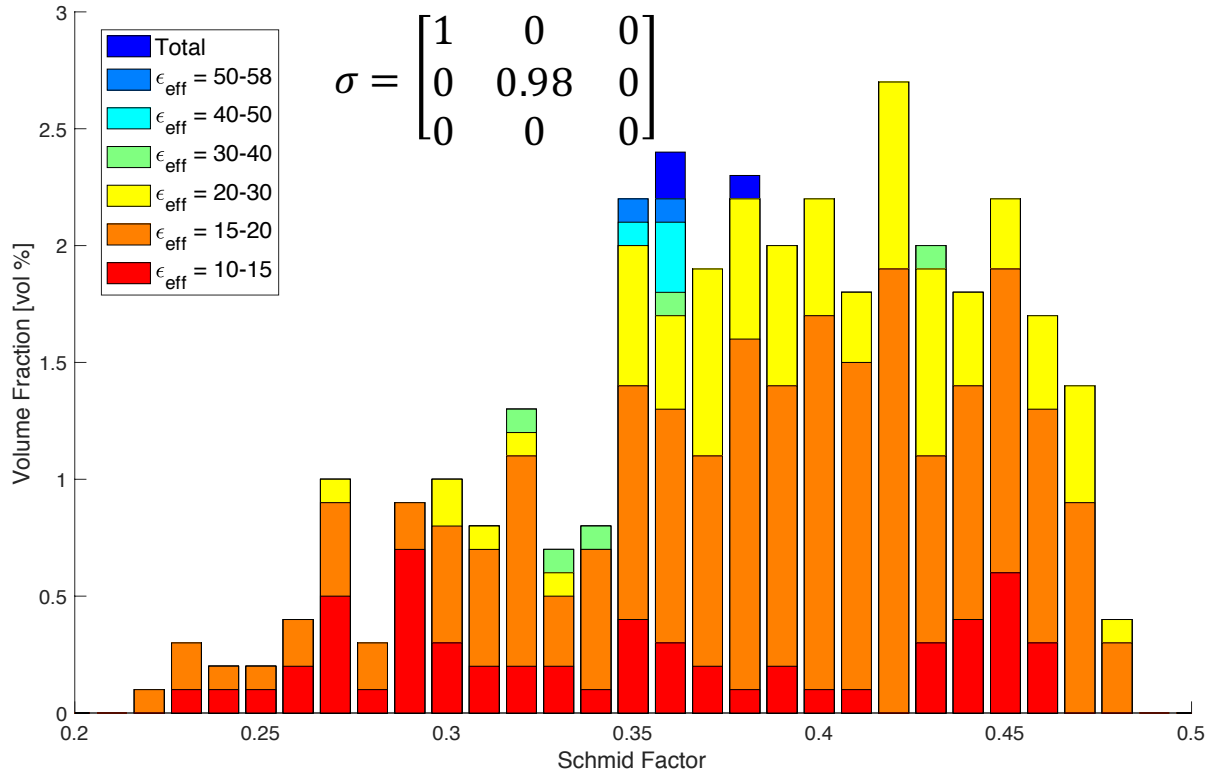
Figure 39: Second highest Schmid factor for Habit Planes of γ-austenite crystals under biaxial tension in RD

7.3 Forming Limit Analysis

The Taylor type TRIP crystal plasticity model was implemented into the MK FLD analysis proposed by *Wu et al.* [198] to calculate the FLDs. Two formability studies are presented to demonstrate the effect of transformation induced plasticity on the FLD through the mechanical response of DSS:

1) The effects of the constitutive and transformation model kinetics on formability
2) The effects of transformation threshold criteria parameters on formability

Each formability study was conducted with a macroscopic strain rate of $D_{11} = 1.0 \times 10^{-3} s^{-1}$, in-plane strain proportionality constant of $-0.5 \leq \rho \leq 1.0$, in $\Delta\rho = 0.1$ increments, and initial band angle $0° \leq \Psi_0 \leq 20°$, in $\Delta\Psi_0 = 5°$ increments. A range of imperfection parameters used in MK analysis has been seen in literature depending on the formulation, various incorporated effects and material, anything from $0.9027 \leq f \leq 0.99995$ are observed [178] [202] [222]. This coefficient is typically calibrated to the onset of localization observed in a plane-strain tension experiment. However, due to the lack of experimental FLD for the TRIP assisted DSS, the simulated FLDs in

this section are explored using an imperfection parameter of $f = 0.99$ [178] [202] [222]. Thus, the potential shape and effects of transformation on the FLD are studied in-depth. The first study presents the influence of incorporating the transformation induced plasticity criterion into a crystal plasticity MK-framework with the calibrated material parameters and transformation criterion parameters shown in Chapter 6. The second study analyzes the effect of varying the transformation coefficients in a parametric study on C_{t1} and C_{t2} from Equation 4.26. This will give insight into how timing martensite generation can influence the forming limit.

7.3.1 Effects of Martensite Transformation Kinetics on Crystal Plasticity Formability Analysis

In this section, forming limit diagrams of the calibrated material presented are simulated and discussed. The importance of various transformation kinetics on formability was studied by disabling the constitutive model feature (setting constants to extremely large or small values). Table 20 presents the test matrix that was used to conduct this study. A total of 4 formability studies were created by simulating the complete TRIP response of DSS, disabling the single variant Bain orientation, disabling transformation kinetics (dual-phase ferrite and austenitic steel), and setting all austenite properties to martensite (dual-phase ferrite and martensite steel).

Table 20: Test Matrix of Transformation Kinetics Study

Simulation	Simulation Type	Modifications
1	Full Model of DSS	None
2	No Bain Rotation	$\varphi_1 = \varphi_1 + 45° \rightarrow \varphi_1 = \varphi_1 + 0°$
3	No Martensite Transformation	$C_{t1} = C_{t2} = 10^5$
4	No Austenite Phase	• Set all FCC austenite crystal properties to BCC martensite

7.3.1.1 Analysis of Forming Limit for Duplex Stainless Steel

Figure 40 and presents the simulated FLD and resulting band angles for the DSS. The FLD shows limit strains of 0.776, 0.507, and 0.422 for uniaxial tension, plane strain, and equibiaxial tension respectively. Similar experimental forming limits of a silicon TRIP steel (with a volume fraction of retained austenite is at ~13%) shows similar curvature and shape [223]. Another remarkable result is the location of the lowest limit strain. Generally, the plane strain formability

has the lowest limit strain. In the studied material, the simulated lowest limit strain of 0.397 occurred at a proportionality ratio of $\rho = 0.5$. This characteristic shape is a result of the stress-strain response post necking. *Mohammadi et al.* [224] showed the importance of accurately capturing the post necking behavior of the material on FLDs. In their study, simulations of FLDs with approximately linear hardening in the post necking region produced a similarly shaped FLD where the limit strain was lowest in the biaxial stretching regime. Figure 41 presents the resulting band angle evolution as a function of the proportionality straining constant highlighting some rotation of the band. Furthermore, it is important to note that no simulation reached a final band angle of $+20°$.
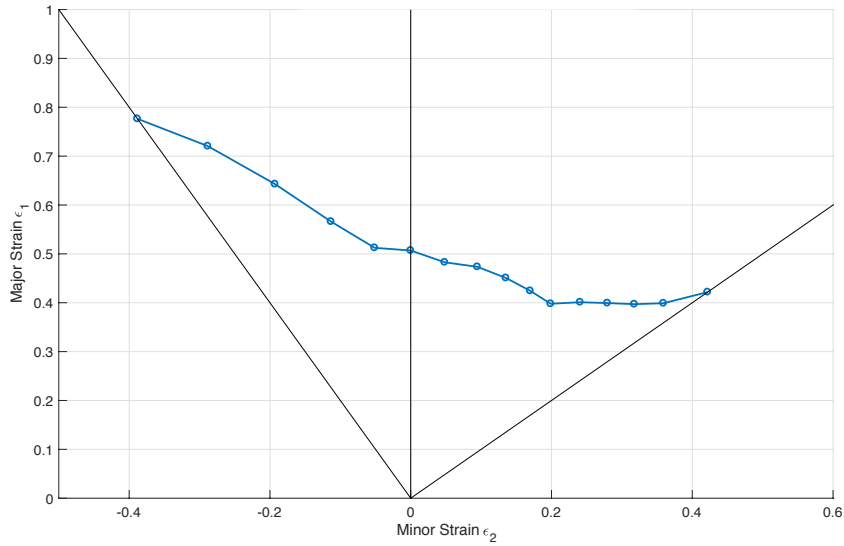
Figure 40: Forming limit diagram with calibrated material parameters of DSS
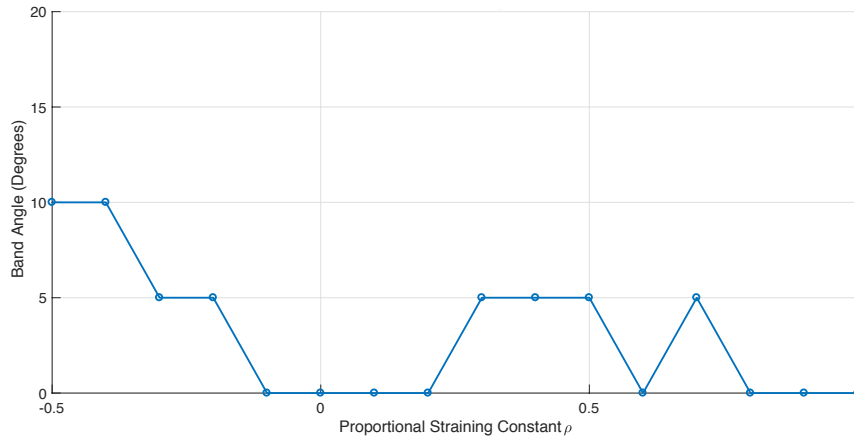
Figure 41: Forming limit diagram band angles with calibrated material parameters

Table 21 - Table 23 presents crystallographic textures at the lowest limit strains inside and outside of the band of α-ferrite, α'-martensite and γ-austenite respectively. It should be noted that no in-band austenite texture plots are presented due to complete transformation during localization. Similarities in texture are highlighted in red circle and arrows in Table 22 and Table 23. Texture components outside of the band show similarities to those presented earlier in this chapter, but with higher intensities due to a higher strain levels. Due to the mechanics of localization, all strain paths inside the band eventually converge to plane strain before failure; therefore, all in-band texture plots show similarities to the plane strain textures as expected.

Table 21: Comparing different loading condition at limit strain of γ- austenite texture

Effective Strain	γ −Phase Texture				
Uniaxial Out of Band $\rho = -0.5$					
Plane Strain Out of Band $\rho = 0.0$					
Equi-biaxial Out of Band $\rho = 1.0$					
Φ φ_2	$\varphi_2 = 0°$	$\varphi_2 = 30°$	$\varphi_2 = 45°$	$\varphi_2 = 60°$	
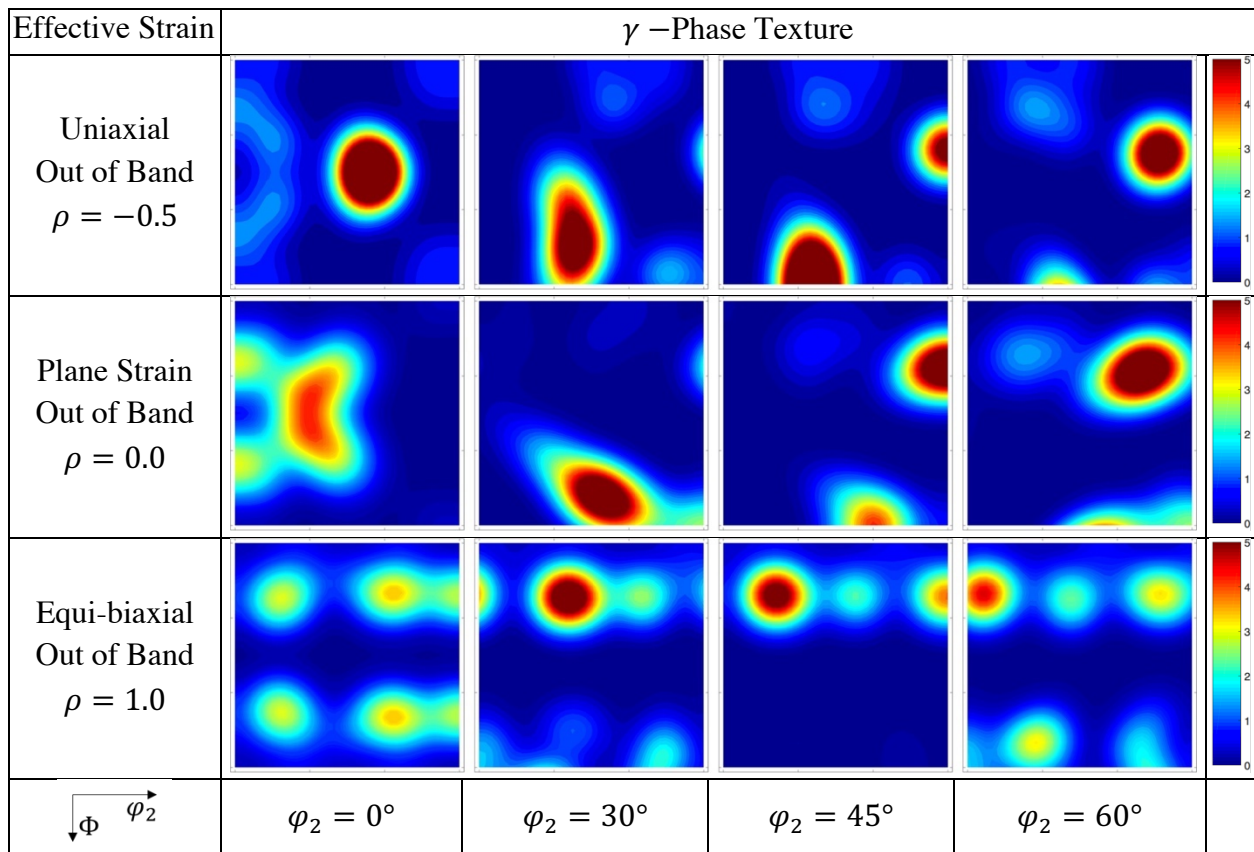
Table 22: Comparing different loading condition at limit strain of α- ferrite texture

Effective Strain	α −Phase Texture				
Uniaxial Out of Band $\rho = -0.5$					
Uniaxial In Band $\rho = -0.5$					
Plane Strain Out of Band $\rho = 0.0$					
Plane Strain In Band $\rho = 0.0$					
Equi-biaxial Out of Band $\rho = 1.0$					
Equi-biaxial In Band $\rho = 1.0$					
Φ φ_2	$\varphi_2 = 0°$	$\varphi_2 = 30°$	$\varphi_2 = 45°$	$\varphi_2 = 60°$	
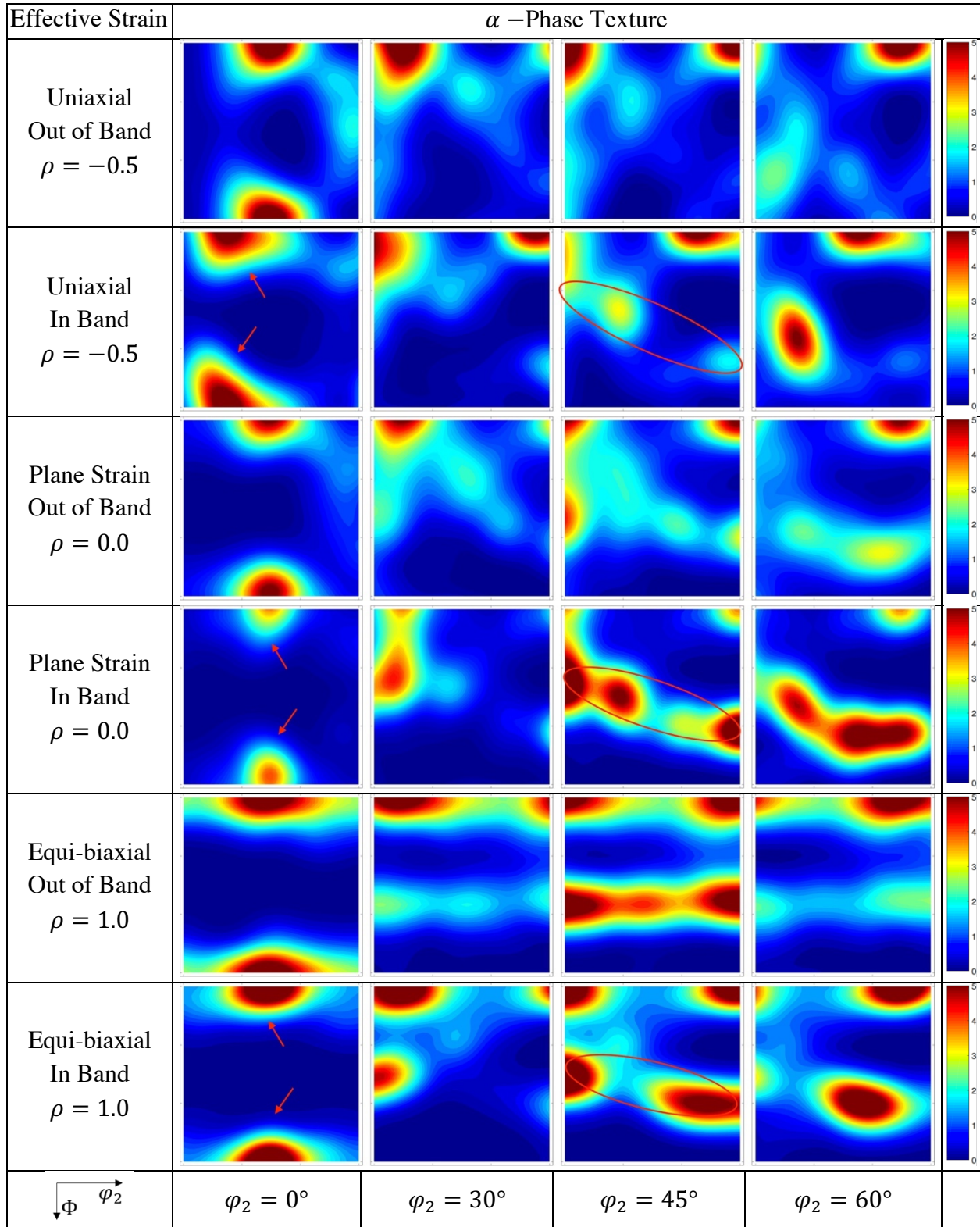
Table 23: Comparing different loading condition at limit strain of α′- martensite texture

Effective Strain	α' −Phase Texture				
Uniaxial Out of Band $\rho = -0.5$					
Uniaxial In Band $\rho = -0.5$					
Plane Strain Out of Band $\rho = 0.0$					
Plane Strain In Band $\rho = 0.0$					
Equi-biaxial Out of Band $\rho = 1.0$					
Equi-biaxial In Band $\rho = 1.0$					
Φ φ_2	$\varphi_2 = 0°$	$\varphi_2 = 30°$	$\varphi_2 = 45°$	$\varphi_2 = 60°$	
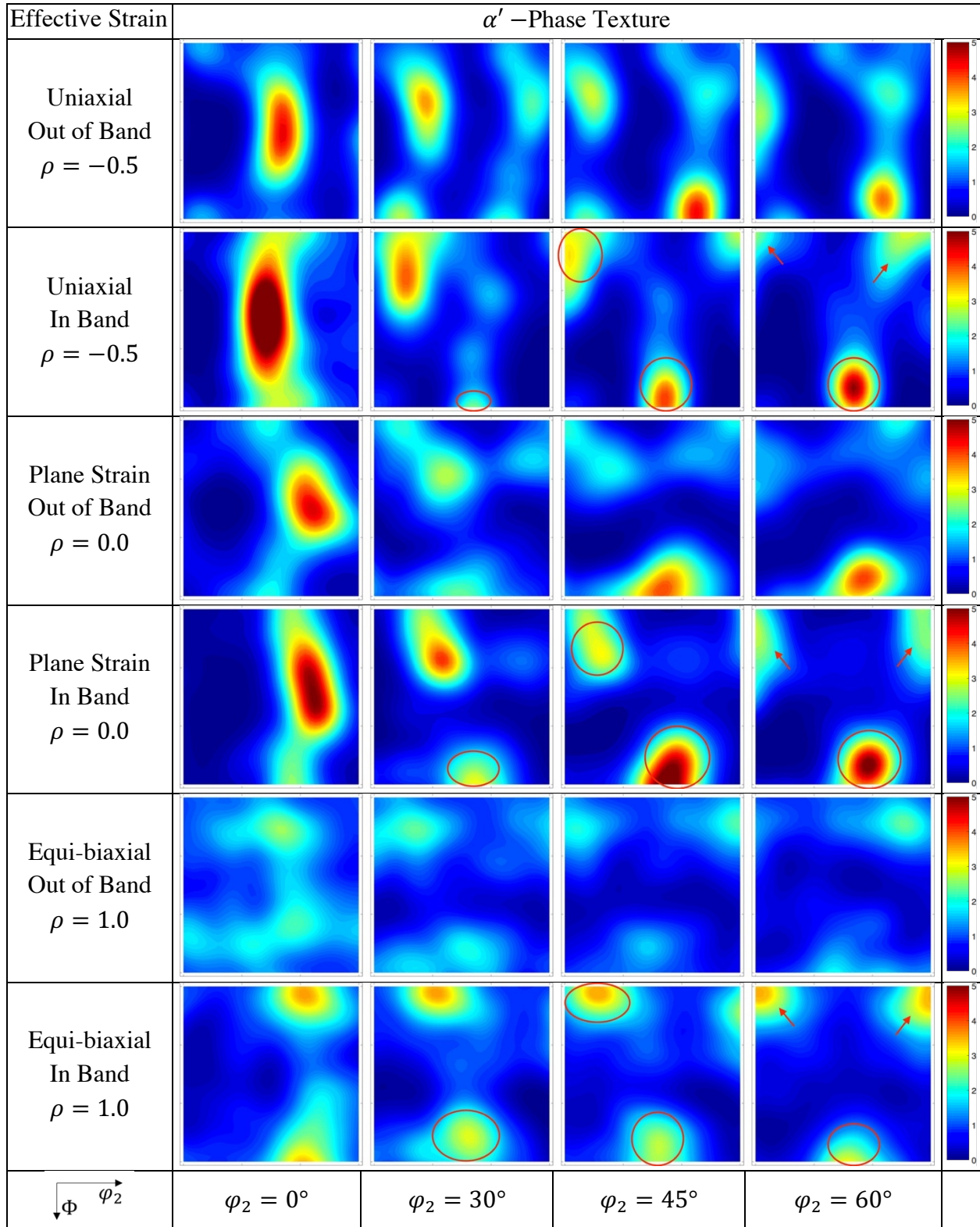
7.3.1.2 Analysis of Incorporating Martensite Transformation Kinetics into Formability Analysis

Figure 42 presents the predicted formability of the DSS without the Bain spin variant, DSS without martensite transformation and austenite material parameters replaced with martensite material parameters. The complete formulation of TRIP for simulating the DSS is also presented for comparison. Table 24 presents a summary of the limit strains at uniaxial, plane strain, and equi-biaxial tension. Figure 43 presents the thinning ratio, stress response, hardening rate and martensite volume fraction evolution inside and outside the band at various load paths for the four simulations studied. The thinning ratio is defined as the ratio between the strain rate outside of the band and inside of the band ($\dot{\varepsilon}_{33}/\dot{\varepsilon}_{33}^{b}$). Note that this is the inverse of the *Hutchinson and Neale* [184] relationship for localization.

Formability of the full TRIP model shows superior formability throughout the entire strain proportionality domain; the full TRIP model shows at least 20% more formability and more than 100% increase in the formability in plane strain tension. This result highlights the significance of TRIP in increasing formability. Until approximately 10% strain, no martensite has formed in the material. Thus, the hardening and necking responses are identical with a steady increase in the thinning ratio. In the full model, martensite begins to evolve that results in an immediate increase in the hardening rate (black arrows in Figure 43). Yet, the hardening rate of the model without transformation continues to decline. This rapid change in the hardening rate stabilizes the localization behavior by a sudden reduction of the thinning ratio which increased the strain to failure (red arrows in Figure 43).

Overall, predictions with and without incorporating the Bain variant show little to no influence on formability. The complete TRIP formulation shows a slight increase in formability (~0.3% strain) on the drawing side ($\rho < 0$) due to the abrupt rotation that introduces an additional straining mechanism. As mentioned earlier, *Cherkaoui et al.* [157] [158] has shown that multiple variants of crystallographic orientations for martensite are possible. A further study should be performed that incorporates multiple variant selection schemes of martensite and its impact on formability.

Comparison of the dual phase ferrite-martensite forming limit curve further highlights the advantages of the TRIP mechanism. From uniaxial tension to midway through the stretching regime ($\rho = 0.5$), the full model DSS predicts higher formability. The dual phase ferrite-martensite curve, however, shows superior formability in the biaxial regime. In the TRIP-assisted material, the majority of transformation occurs in the first 20% strain before localization becomes uncontrollable. As such, there was too much martensite generation to suppress necking in an efficient manner. Furthermore, the dual phase ferrite-martensite has 24 slip systems for all crystals compared to the TRIP-enhanced material with 12 slip systems in the FCC phase. The higher number of slip systems leads to a smoother yield locus in the biaxial to plane strain region that produces better formability in the biaxial region [118]. Nevertheless, one could control the material processing parameters to govern the rate of martensite transformation in this critical strain path.
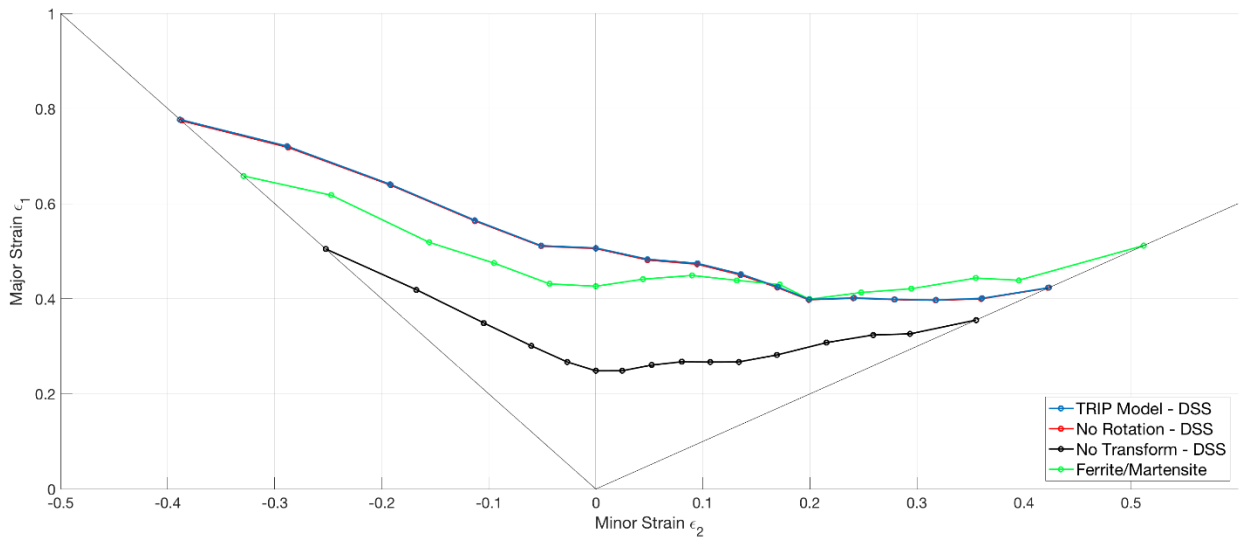
Figure 42: Predicted formability of a) Full Model of DSS, b) No Bain Spin, c) No Martensite Transformation and d) Ferrite/Martensite

Table 24: Transformation Kinetics Study of Forming Limit Strains

Simulation	Simulation Type	Major Strain $\rho = -0.5$	Major Strain $\rho = 0.0$	Major Strain $\rho = 1.0$
1	Full Model of DSS	0.777	0.507	0.423
2	No Bain Spin	0.774	0.506	0.423
3	No Martensite Transformation	0.505	0.249	0.355
4	No Austenite Phase	0.658	0.426	0.512
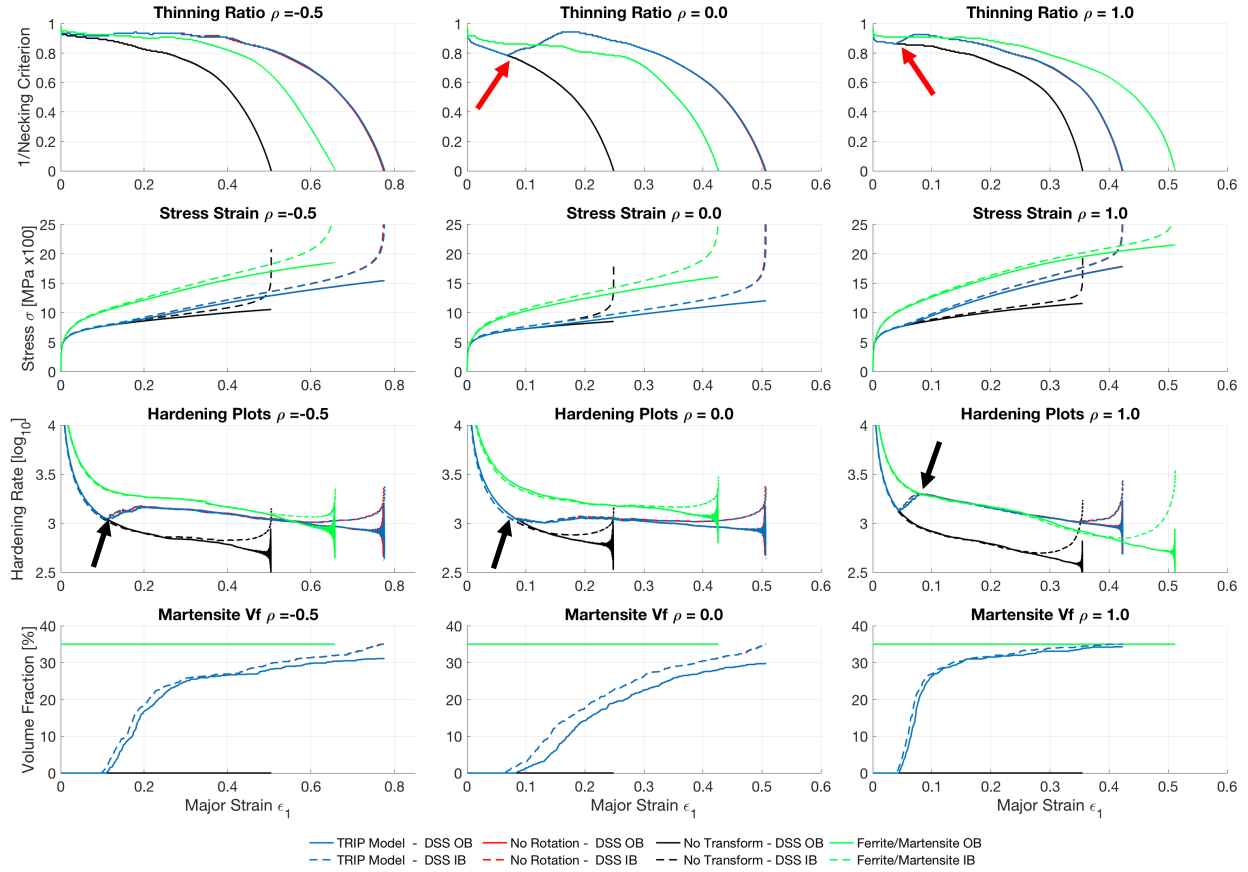
Figure 43: Thinning Ratio, Stress Response, Hardening Rate and Martensite Volume Fraction Evolution vs Out of Band Effective Strain at various load paths for the four simulations studied

7.3.2   *Effect of Transformation Threshold Criteria Parameters on Formability*

The TRIP effect is known to be sensitive to temperature [34] [180] [200], strain-rate [153] [154] [155] and triaxiality [217] [218] [219] [220] [221]. Typically, TRIP models and criteria that describe the driving energy of transformation are calibrated to a series of experiments performed at various boundary conditions. As presented earlier, the effect of triaxiality is inherently captured through the accumulated shear component of the transformation criteria (Equation 4.26). Similar to the coefficients in *Iwamoto and co-workers* [153] [154] [155], thermal sensitivity can be expressed in terms of the coefficients C_{t1} and C_{t2} such that an increase in temperature represents an increase in the threshold energy needed for transformation. Varying C_{t1} and C_{t2} changes the transformation rate of martensite, which directly influences the hardening rate that is fundamental in influencing formability [198]. Unfortunately, no experimental measurements exist at various temperatures for the DSS studied in this work. Nevertheless, there still exists little understanding

on how these factors affect the forming limit of TRIP-assisted steel [203]. As such, a parametric study of the transformation criteria parameters, C_{t1} and C_{t2}, can provide significant insight into the formability of TRIP steel. In this section, the sensitivity of the transformation threshold criteria is presented and discussed. The parameter coefficients used were $C_{t1} = \{280, 300, 320, 340, 360, 380\}$ and $C_{t2} = \{10, 20, 30, 40, 50, 60\}$. This generated 36 different combinations of threshold criteria. Figure 44 presents a graphical representation of the domain of transformation thresholds that this study explored.
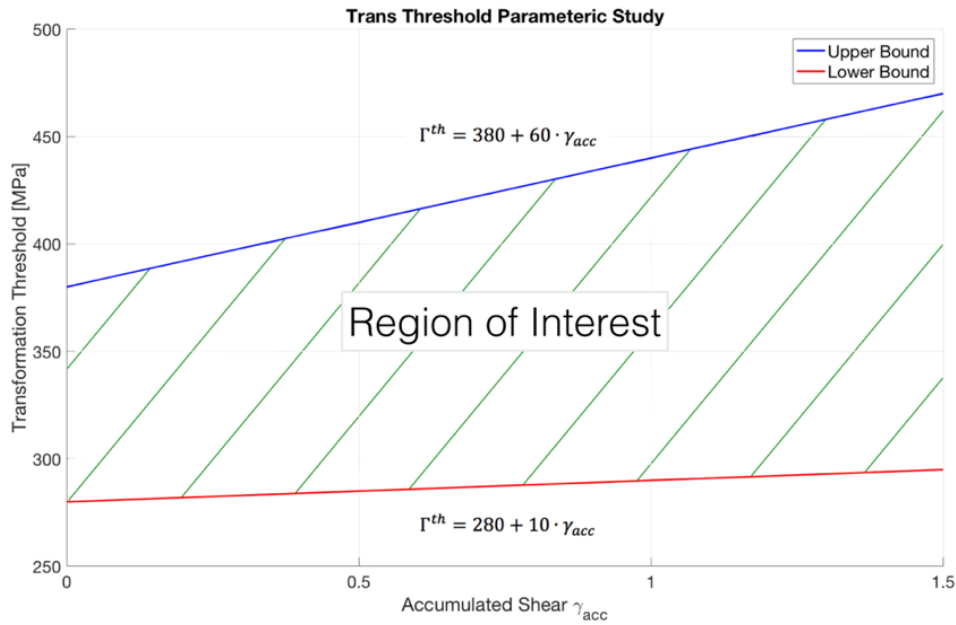
Figure 44: Domain of transformation thresholds studied

For each combination, the forming limit diagram was generated along with the thinning ratio, stress response, hardening rate and martensite volume fraction evolution inside and outside the band during uniaxial, plane strain, and biaxial tension. This study yielded a substantial amount of information and results. As such, three studies that are of significance are presented for further discussion:

1) Varying C_{t2} for a low value of $C_{t1} = 280$
2) Varying C_{t2} for a high value of $C_{t1} = 380$
3) Varying C_{t1} for a low value of $C_{t2} = 10$

A summary of the other remaining analyses is presented in APPENDIX A.3.

7.3.2.1   Varying C_{t2} for a Low Value of $C_{t1} = 280$

Figure 45 presents the FLD for $C_{t1} = 280$ and C_{t2}=10:10:60 with thinning ratio, stress response, hardening rate and martensite volume fraction evolution. In general, increasing C_{t2} increased in formability in this study. This was accomplished by reducing the volume fraction generation rate that helped stabilize and prevent localization. However, the hardening behavior and martensite evolution were all similar. With a low C_{t1} threshold, low stress/energy is required for transformation resulting in high volume fraction of martensite during deformation with minimal variation due to C_{t2}.

7.3.2.2   Varying C_{t2} for a High Value of $C_{t1} = 380$

Figure 46 presents the FLD for $C_{t1} = 380$ and C_{t2}=10:10:60 with thinning ratio, stress response, hardening rate and martensite volume fraction evolution. At a higher value of C_{t1}, transformation from austenite to martensite is more difficult. As such, lower volume fractions of martensite were observed, as well as lower generation rates. Furthermore, with higher value of C_{t1}, C_{t2} becomes much more influential on the FLD response. With a high value of the C_{t2} coefficient, transformation of martensite is completely suppressed outside of the band. Yet, the volume fraction of martensite still evolves within the band. As the in-band evolves towards plane strain due to localization, more habit planes can satisfy the transformation threshold, which accelerates the martensite generation in the band. This amplifies the incompatibility between the two points, which promotes necking.

7.3.2.3   Varying C_{t1} for a Low Value of $C_{t2} = 10$

Figure 47 presents the FLD for $C_{t2} = 10$ and C_{t2}=280:20:380 with thinning ratio, stress response, hardening rate and martensite volume fraction evolution. At a low value of C_{t2}, the rate of martensitic transformation is reduced and delayed through an increase of C_{t1}. As observed in plane strain, there is a significant delay in martensite formation. As such, as the material begins to localize, the martensite generation rate is insufficient to recover from localizing and eventually necks. Conversely, martensite formation is highly favoured in biaxial tension. This means that delaying martensite formation during biaxial stretching allows for increased hardening at a suitable time that stabilizes localization to enhance the limit strain.
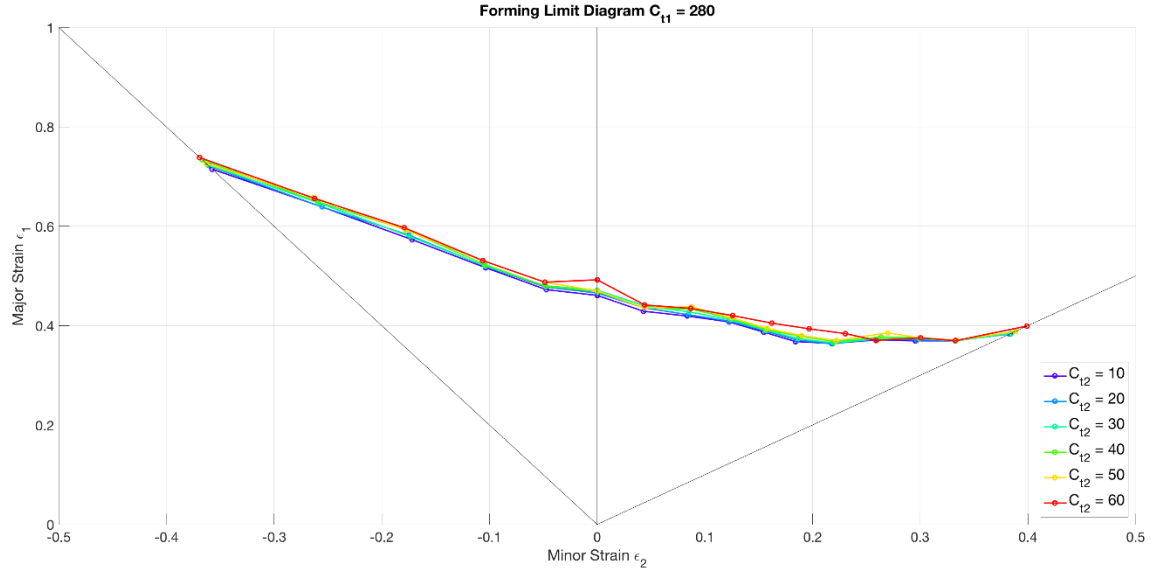
Figure 45: Forming Limit Diagram for $C_{t1} = 280$ and $C_{t2} = 10:10:60$ with Thinning Ratio, Stress Response, Hardening Rate and Martensite Volume Fraction Evolution vs Out of Band Effective Strain at various load paths
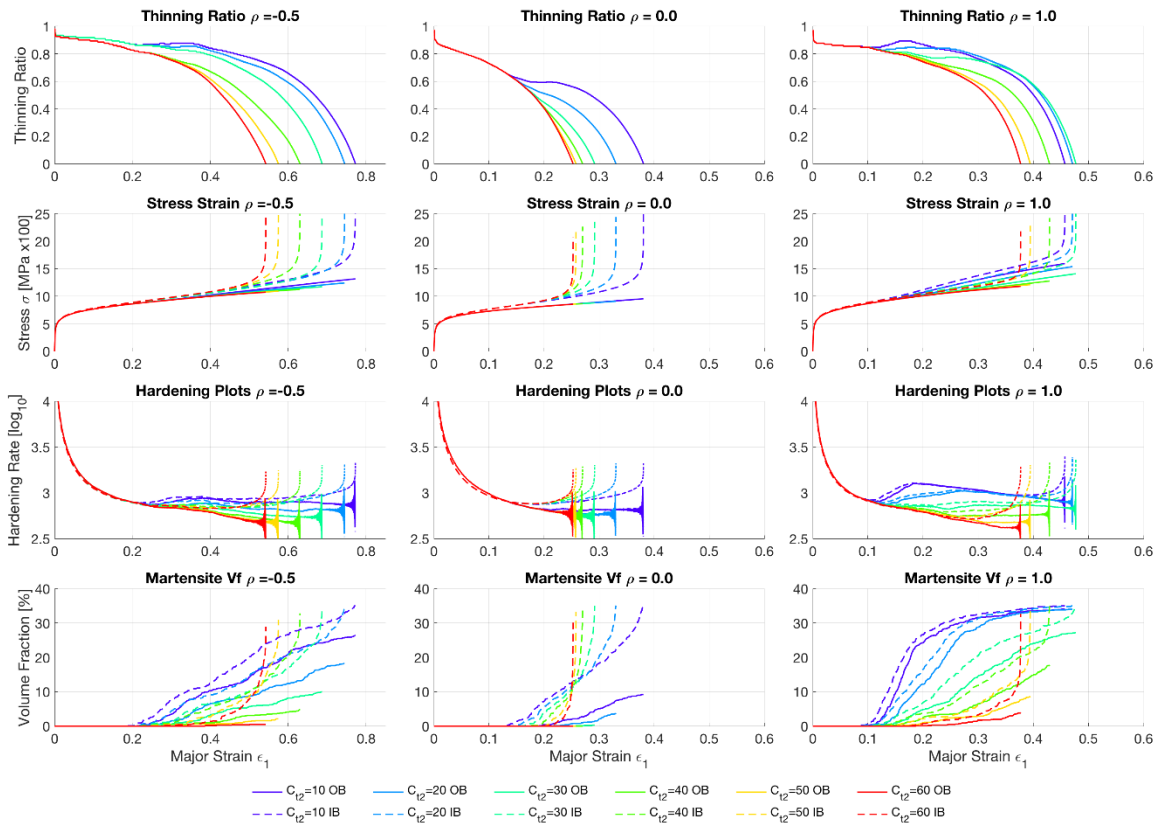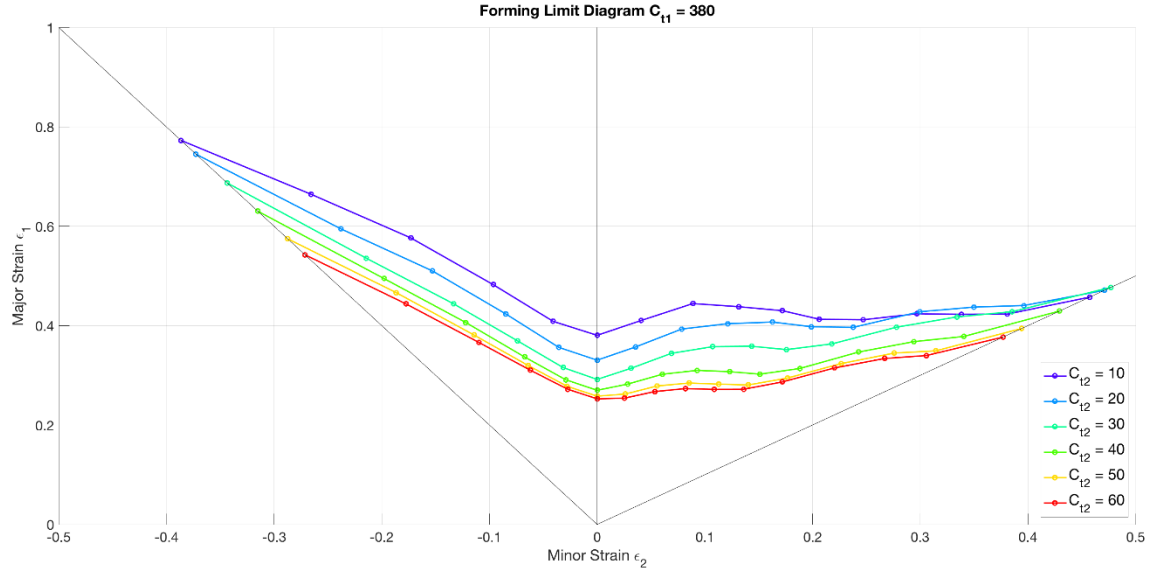
Figure 46: Forming Limit Diagram for $C_{t1} = 380$ and C_{t2} =10:10:60 with Thinning Ratio, Stress Response, Hardening Rate and Martensite Volume Fraction Evolution vs Out of Band Effective Strain at various load paths
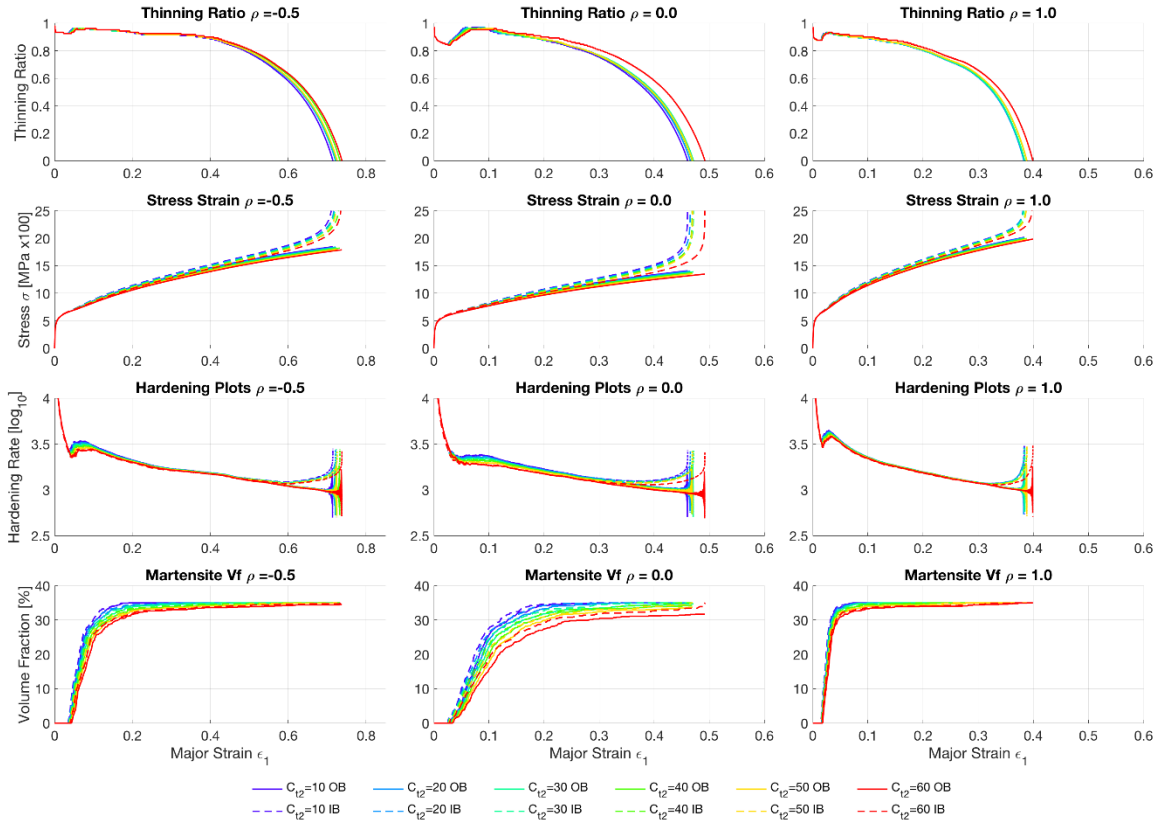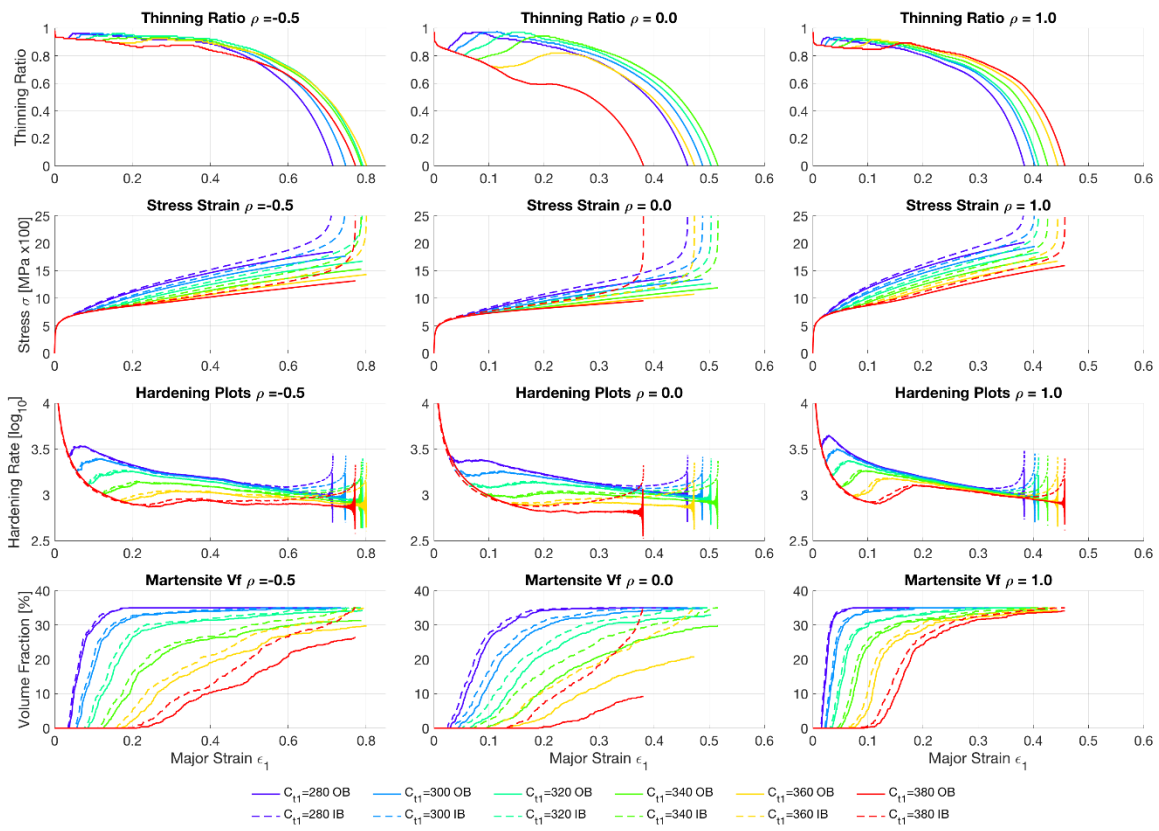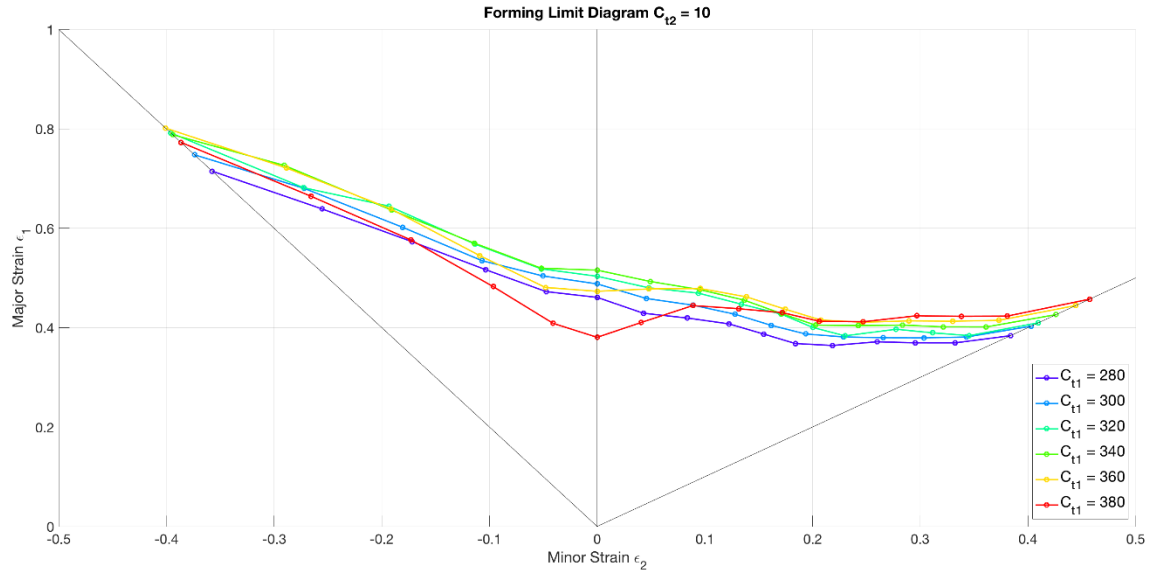
Figure 47: Forming Limit Diagram for $C_{t2} = 10$ and $C_{t2} = 280{:}20{:}380$ with Thinning Ratio, Stress Response, Hardening Rate and Martensite Volume Fraction Evolution vs Out of Band Effective Strain at various load paths

7.3.2.4 Summary of Transformation Threshold Criteria Parameters

Table 25 presents a summary of the maximum obtainable major limit strains uniaxial, plane strain, and equibiaxial and their corresponding coefficients for the range of C_{t1} and C_{t2} studied. The predicted formability of the DSS is used as a baseline for comparison. As expected, high coefficients of C_{t1} and C_{t2} that suppressed martensite had the lowest formability. Modest gains were achieved in improving the plane strain and uniaxial formability (2% - 3%). However, if the forming conditions are not optimal, there is a large decrease in formability (up to ~50% reduction) that can occur. However, a gain of 5.6% strain, which corresponds to a relative improvement of 13.3% can be obtained by delaying martensite formation.

Table 25: Potential formability improvements with transformation criterion control

	$\rho = -0.5$	C_{t1}	C_{t2}	$\rho = 0.0$	C_{t1}	C_{t2}	$\rho = 1.0$	C_{t1}	C_{t2}
Baseline	0.776	300	24	0.507	300	24	0.422	300	24
Lowest	0.543	380	60	0.253	380	60	0.377	380	60
Highest	0.801	360	10	0.516	340	10	0.478	340	50
Highest Gain Baseline	+3.2 %			+1.8 %			+13.3 %		
Lowest Gain Baseline	−30.0 %			−50.1 %			−10.7 %		

8 CONCLUSIONS & FUTURE WORK

The objective of this thesis was to develop a crystal plasticity constitutive model that incorporated martensitic transformation to simulate formability of TRIP assisted AHSS. A Taylor type TRIP crystal plasticity formulation was developed to capture the macro and micro-mechanical response of TRIP assisted multiphase steels for forming. A new stress-based transformation criterion, based on the micromechanics of habit-plane interaction, was developed to initiate transformation. The model was successfully calibrated to the experimental stress-strain and volume fraction evolution presented in *Kim et al.* [163] for duplex stainless steel. Simulations of single crystal and polycrystalline aggregates were performed to highlight the transformation mechanisms of the TRIP effect for different loading directions. The crystal plasticity framework was implemented into the *Marciniak and Kuczynski* (MK) [45] framework to simulate the forming limit diagram of the TRIP assisted AHSS.

8.1 TRIP Crystal Plasticity Constitutive Model

The key conclusions drawn from the study of the TRIP crystal plasticity constitutive model are as follows:

- This is the first Taylor type TRIP crystal plasticity framework to simulate the macro and micro-mechanical response of TRIP assisted multiphase steels.
- Transformation criterion is triaxiality dependent through the variation of accumulated shear in different loading conditions.
- Austenite orientations of rotated brass ($\varphi_1 = 50°, \Phi = 45°, \varphi_2 = 0°$) and copper ($\varphi_1 = 40°, \Phi = 90°, \varphi_2 = 45°$) were common textures for not promoting transformation during uniaxial tension along the rolling direction and transverse direction. However, orientations that did not promote transformation were strain path dependent. Interestingly, all ODFs of α'- martensite showed common orientations at ($\varphi_1 = 0°/90°, \Phi = 45°, \varphi_2 = 0°$) and ($\varphi_1 = 80°, \Phi = 45°, \varphi_2 = 0°$).
- Simulations of uniaxial tension showed that austenite crystals with lower Schmid factor generally transformed with the least amount of deformation. This is a result of the transformation criteria being stress-based where austenite crystals with a lower Schmid factor generate higher stress through elasticity that is needed to transform. Although the

stress-based transformation biased higher Schmid factor on the habit plane crystals, competition exists between the magnitude of the stress developed by low Schmid factor crystals on the dislocation planes.

- Although some orientations were primed for transformation, the resulting texture evolution could re-orientate a crystal lattice away from generating stress on the habit planes which delay transformation.

- It was observed that a small change in the transformation threshold could lead to an abrupt, discontinuous change in the strain at which austenite crystals can transform.

8.2 TRIP Crystal Plasticity MK Model

The highlights from the study of the MK-analysis with TRIP crystal plasticity constitutive model are as follows:

- To the author's knowledge, this is the first Taylor type TRIP crystal plasticity MK framework for modeling multiphase TRIP steel.

- The mechanism of transforming from low strength austenite to high strength martensite showed enhanced formability compared to a material without the mechanism. At least 20% improvement in formability was observed when incorporating the transformation mechanism. This was a result of martensite transformation occurring at a time where it could suppress necking through a sudden increase in hardening rate.

- Incorporation of the single variant Bain orientation into the TRIP formulation showed a minor difference in formability predictions with a peak difference of ~0.3% strain out of 78% strain on the drawing side ($\rho < 0$).

- Controlling the processing properties that influence the transformation threshold criteria can delay the formation of martensite to a time that is advantageous. Through this method, a gain of 5.6% strain, which corresponds to a relative improvement of 13.3%, for equibiaxial tension compared to the formability of the DSS studied.

- Controlling these threshold parameters yield modest gains in improving the plane strain and uniaxial formability (2% - 3%) over the formability of DSS. However, if the forming conditions are not optimal, a reduction by up to 50% could be observed (from 50% strain to 25% strain).

8.3   Future Work

The results of this thesis highlighted the influence of TRIP effect on the micro and macro-mechanical response in multiple loading conditions as well as the effect of the transformation criterion on formability. The following recommendations are presented for future work:

1) In the present work, a single uniaxial tension stress strain curve and the corresponding volume fraction evolution was used to calibrate the model. However, the mechanical response and martensite evolution of TRIP-assisted steel have been shown to be sensitive to triaxiality [221], strain-rate [225] [226], and temperature [155]. It is recommended that the following sets of data be obtained for a complete calibration of a single material:
    a.   Initial and final EBSD measurements of the material's texture
    b.   Stress strain curves at varying strain rates, temperatures and sheet orientation with corresponding in-situ volume fraction measurements
    c.   Heat generation profiles during deformation
2) Experimental forming limit diagrams with varying isothermal conditions, as experimentally conducted by *Krauer and Hora* [227], is recommended for further validation of this framework.
3) The current model assumes a Taylor-type homogenization approach to simulate the polycrystalline response. *Kim et al*. [163] used CPFEM to simulate the non-uniform deformation behavior of the RVE. Then again, the CPFEM approach is currently not suitable for calculations in the MK-framework (due to computational limitations). However, advanced homogenization techniques, such as the viscoplastic self-consistent scheme (VPSC) [228], can be implemented into MK-calculations using the TRIP constitutive model. This concept should be explored and compared to the Taylor-type TRIP crystal plasticity homogenization scheme for MK-calculations.
4) The current model transformed only to a single variant of martensite and showed little to no significant influence on formability. However, *Cherkaoui et al*. [157] [158] has shown that multiple variants of crystallographic orientations for martensite are possible. A further study should be performed that incorporates multiple variant selection schemes of martensite and its impact on formability.

5) The current formulation assumed that all conditions were performed isothermally. No thermal effects, such as heat generation from plastic work or latent heating of martensite transformation. *Rusinek and Klepaczko* [73] has shown that significant heat generation occurred during uniform and localized deformation. Furthermore, recent models have been developed for crystal plasticity that incorporates thermally-induced deformations [132] [199] [229]. With the current framework, thermodynamic effects can be added to enhance the physics of this model further to capture thermal softening of the individual phase parameters at elevated temperatures.

6) Naturally, additional slip system activity for the BCC lattice needs to be incorporated to simulate formability at elevated temperatures for these TRIP-assisted steels [137].

7) Recently, *Kohar et al.* [109] presented a multi-scaling approach for calibrating phenomenological constitutive models that captures microstructural evolution. The current framework can be used to calibrate a yield surface by generating virtual experiments and simulate the behaviour of TRIP-assisted steel in lab-scale simulations of deformation.

9 References

[1] US Department of Transportation, "Corporate Average Fuel Economy," 21 May 2010. [Online]. Available: https://www.nhtsa.gov/laws-regulations/corporate-average-fuel-economy#light-duty-stakeholders.

[2] L. Cheah, "Cars on a Diet: The Material and Energy Impacts of Passenger Vehicle Weight Reduction in the U.S.," *Ph.D. Thesis, Massachusetts Institute of Technology*, 2010.

[3] N.H.T.S.A., "Overview of NHTSA Priority Plan for Vehicle Safety and Fuel Economy, 2015 to 2017," N.H.T.S.A., Washington, D.C., 2015.

[4] United States Evironmental Protection Agency, "Light-Duty Automotive Technology, Carbon Dioxide Emissions, and Fuel Economy Trends: 1975 Through 2016," 15 November 2016. [Online]. Available: https://www.epa.gov/sites/production/files/2016-11/documents/420s16001.pdf.

[5] N. Lutsey, "Review of technical literature and trends related to automobile mass reduction technology," University of California, Davis, Davis, California, 2010.

[6] Y. Miyaoka and H. Muraoka, "Developement of an all-aluminium automotive body," *Joural of Materials Processing Technology,* vol. 38, no. 4, pp. 655-674, 1993.

[7] M. Kulekci, "Magnesium and its alloys applications in automotive industry," *International Journal of Advanced manufacturing Technology,* vol. 29, no. 9-10, pp. 851-865, 2008.

[8] D. Gerard, "Materials and Processes in the Z06 Corvette," *Advanced Materials and Processes,* vol. 166, no. 1, pp. 30-33, 2008.

[9] Autointell, "World's first volume-production aluminium car Audi A2 - fascinating technology and a new form of agility," 23 August 1999. [Online]. Available: http://www.autointell-news.com/european_companies/volkswagen/audi-ag/audi-cars/audi-a2/audiag1112.htm. [Accessed 1 July 2017].

[10] F. Froes, H. Friedrich, J. Kiese and D. Bergoint, "Titanium in the family automobile: The cost challenge," *Journal of Materials,* vol. 56, no. 2, pp. 40-44, 2004.

[11] H. Adam, "Carbon fiber in automotive applications," *Materials and Design,* vol. 18, no. 4-6, pp. 349-355, 1997.

[12] E. Fuchs, F. Field, R. Roth and R. Kirchain, "Strategic materials selection in the automobile body: Economic opportunities for polymer composite design," *Composites Science and Technology,* vol. 68, no. 9, pp. 1989-2002, 2008.

[13] R. Schultz and A. Abraham, "Metallic Material Trends For North American Light Vehicles," 2009. [Online]. Available: http://www.autosteel.org/~/media/Files/Autosteel/Great%20Designs%20in%20Steel/GDIS%202009/06%20-%20Metallic%20Material%20Trends%20For%20North%20American%20Light%20Vehicles.pdf. [Accessed 1 July 2017].

[14] O. Bouaziz, H. Zurob and M. Huang, "Driving Force and Logic of Development of Advanced High Strength Steels for Automotive Applications," *Steel Research International,* vol. 84, no. 10, pp. 937-947, 2013.

[15] S. Birch, "Jaguar remakes XJ," 4 March 2010. [Online]. Available: http://articles.sae.org/7547/. [Accessed 1 July 2017].

[16] G. Speich, V. Demarest and R. Miller, "Formation of Austenite During Intercritical Annealing of Dual-Phase Steels," *Metallurgical Transactions A,* vol. 12, no. 8, pp. 1419-1428, 1981.

[17] R. Davies, "Influence of martensite composition and content on the properties of dual phase steels," *Metallurgical Transactions A,* vol. 9, no. 5, pp. 671-679, 1978.

[18] G. Thomas and N. Kim, "Effects of morphology on the mechanical behaviour of a dual phase Fe/2Si/0.1C steel," *Metallurgical Transactions A,* vol. 12, no. 3, pp. 483-489, 1981.

[19] R. Davies, "The deformation behavior of a vanadium-strengthened dual phase steel," *Metallurgical Transactions A,* vol. 9, no. 1, pp. 41-52, 1978.

[20] M. Delince, Y. Brechet, J. Embury, M. Geers, P. Jacques and T. Pardoen, "Structure - property optimization of ultrafine-grained dual-phase steels using a microstructure-based strain hardening model," *Acta Materialia,* vol. 55, no. 7, pp. 2337-2350, 2007.

[21] Y. Sakuma, O. Matsummura and H. Takechi, "Mechanical properties and retained austenite in intercritically heat-treated bainite-transformed steel and their variation with Si and Mn additions," *Metallurgical Transactions A,* vol. 22, no. 2, pp. 489-498, 1991.

[22] K.-I. Sugimoto, M. Kobayashi and S.-I. Hashimoto, "Ductility and strain-induced transformation in a high-strength transfromation-induced plasticity-aided dual-phase steel," *Metallurgical Transactions A,* vol. 23, no. 11, pp. 3085-3091, 1992.

[23] K.-I. Sugimoto, M. Misu, M. Kobayashi and H. Shirasawa, "Effects of Second Phase Morphology on Retained Austenite Morphology and Tensile Properties in a TRIP-aided Dual-phase Steel Sheet," *Iron and Steel Institute of Japan,* vol. 33, no. 7, pp. 775-782, 1993.

[24] A. Hanzaki, P. Hodgson and S. Yue, "The Influence of Bainite on Retained Austenite Characteristics in Si-Mn TRIP Steels," *The Iron and Steel Insitute of Japan,* vol. 35, no. 1, pp. 79-85, 1995.

[25] P. Jacques, F. Delannay, X. Cornet, P. Harlet and J. Ladriere, "Enhancement of the mecahnical properties of a low-cabon, low-silicon steel by formation of a multiphased microstructure containing retained austenite," *Metallurgical and Materials Transactions A,* vol. 29, no. 9, pp. 2383-2393, 1998.

[26] G. Olson and M. Cohen, "Kinetics of strain-induced martensite nucleation," *Metallurgical and Materials Transactions A,* vol. 6, no. 4, pp. 791-795, 1975.

[27] P. Jacques, "Transformation-induced plasticity for high strength formable steels," *Current Opinion in Solid State and Materials Science,* vol. 8, no. 3-4, pp. 259-265, 2004.

[28] S. Zaefferer, J. Ohlert and W. Bleck, "A study of microstructure, transformation mechanisms and correlation between microstructure and mechanical properties of a low alloyed TRIP steel," *Acta Materialia,* vol. 52, no. 9, pp. 2765-2778, 2004.

[29] E. Girault, P. Jacques, P. Harlet, K. Mols, J. Van Humbeeck, E. Aermoudt and F. Delannay, "Metallographic Methods for Revealing the Multiphase Microstructure of TRIP-Assisted Steels," *Materials Characterization,* vol. 40, no. 2, pp. 111-118, 1998.

[30] K. Zhu, D. Barbier and T. Lung, "Characterization and quantification methods of complex BCC matrix microstructures in advanced high strength steels," *Journal of Material Science,* vol. 48, no. 1, pp. 413-423, 2013.

[31] H. Karbasian and A. Tekkaya, "A review on hot stamping," *Journal of Materials Processing Technology,* vol. 210, no. 15, pp. 2103-2118, 2010.

[32] M. Merklein and J. Lechler, "Investigation of the thermo-mechanical properties of hot stamping steels," *Journal of Materials Processing Technology,* vol. 177, no. 1-3, pp. 452-455, 2006.

[33] A. Bardelcik, M. Worswick, S. Winkler and M. Wells, "A strain rate sensitive constitutive model for quenched boron steel with tailored properties," *International Journal of Impact Engineering,* vol. 50, pp. 49-62, 2012.

[34] T. Angel, "Formation of martensite in austenitic stainless steels," *Journal of Iron Steel Institute,* vol. 177, pp. 165-174, 1954.

[35] P. Hein and J. Wilsius, "Status and Innovation Trends in Hot Stamping of USIBOR 1500 P," *Steel Research International,* vol. 79, no. 2, pp. 85-91, 2008.

[36] O. Bouaziz, S. Allain and C. Scott, "Effect of grain and twin boundaries on the hardening mechanisms of twinning-induced plasticity steels," *Scripta Materialia,* vol. 58, no. 6, pp. 484-487, 2008.

[37] O. Bouaziz, S. Allain, C. Scott, P. Cugy and D. Barbier, "High manganese austenitic twinning induced plasticity steels: A review of the microstructure properties relationships," *Current Opinion in Solid State and Materials Science,* vol. 15, no. 4, pp. 141-168, 2011.

[38] M. Huang, O. Bouaziz, D. Barbier and S. Allain, "Modelling the effect of carbon on deformation behaviour of twinning induced plasticity steels," *Journal of Material Science,* vol. 46, no. 23, pp. 7410-7414, 2011.

[39] R. Ueji, N. Tsuchida, D. Terada, N. Tsuji, Y. Tanaka, A. Takemura and K. Kunishige, "Tensile properties and twinning behavior of high mananese austenitic steel with dine-grained structure," *Scripta Materialia,* vol. 59, no. 9, pp. 963-966, 2008.

[40] J. Speer, E. De Moor, K. Findley, D. Matlock, B. De Cooman and D. Edmonds, "Analysis of microstructure evolution in quenching and partitioning automotive sheet steel," *Metallurgical and Materials Transaction A,* vol. 42, no. 12, pp. 3591-3601, 2011.

[41] M. Santofimia, L. Zhao and J. Sietsma, "Microstructural evolution of a low-carbon steel during application of quenching and partitioning heat treatments after partial austenitization," *Metallurgical and Materials Transaction A,* vol. 40, no. 1, pp. 46-57, 2009.

[42] M. Santofimia, L. Zhao, R. Petrov, C. Kwakernaak, W. Sloof and J. Sietsma, "Microstructual development during the quenching and partitioning process in a newly designed low-carbon steel," *Acta Materialia,* vol. 59, no. 15, pp. 6059-6068, 2011.

[43] T. Furukawa, H. Morikawa, H. Takechi and K. Koyama, "Process factors for highly ductile dual-phase sheet steels," *Strcture and Properties of Dual-Phase Steels,* pp. 281-303, 1979.

[44] G. Taylor, "The mechanism of plastic deformation of crystals. Part I. Theoretical," *Proceedings of the Royal Society of London. Series A, Containing Papers of a Mathematical and Physical Character,* vol. 145, no. 855, pp. 362-387, 1934.

[45] Z. Marciniak and K. Kuczynski, "Limit strains in the processes of stretch-forming sheet metal," *International Journal of Mechanical Sciences,* vol. 9, no. 9, pp. 609-620, 1967.

[46] World Auto Steel, "Steel Market Development Institute Automotive Market Program," [Online]. Available: www.autosteel.org.

[47] World Auto Steel, "Automotive Steel Definitions: Today's AHSS," World Auto Steel, [Online]. Available: http://www.worldautosteel.org/wp-content/uploads/2012/03/AHSSDiagram_WorldAutoSteel-copy.png. [Accessed 1 July 2017].

[48] R. Lawson, D. Matlock and G. Krauss, "The effect of microstructure on the deformation behavior and mechanical properties of a dual-phase steel," *Fundamentals of Dual-Phase Steels,* pp. 347-381, 1981.

[49] W. Bleck and K. Phiu-On, "Effects of Microalloying in Multi Phase Steels for Car Body Manufacture," *Microstructure and Texture in Steels,* pp. 145-163, 2009.

[50] B. De Cooman, "Structure–properties relationship in TRIP steels containing carbide-free bainite," *Current Opinion in Solid State and Material Science,* vol. 8, no. 3, pp. 285-303, 2004.

[51] B. De Cooman, L. Chen, H. Kim, Y. Estrin, S. Kim and H. Voswinckel, "State-of-the-science of high manganese TWIP steels for automotive applications," *Microstructure and Texture in Steels,* pp. 165-183, 2009.

[52] H. Bhadeshia and R. Honeycombe, Steels: microstructure and properties, 4th Ed, Oxford: Butterworth-Heinemann, 2017.

[53] M. Maalekian, "The effects of alloying elements on steels (I)," Christian Doppler Laboratory for Early Stages of Precipitation, 2007.

[54] E. Bain, Alloying Elements in Steels, Cleveland, Ohio: ASM, 1939.

[55] O. Kubaschewski, Iron - Binary phase diagrams, Berlin: Springer Science & Business Media, 2013.

[56] H. Okamoto, Phase diagrams for binary alloys, ASM International, 2000.

[57] A. Bardelcik, C. Calisbury, S. Winkler, M. Wells and M. Worswick, "Effect of cooling rate on the high strain rate properties of boron steel," *International Journal of Impact Engineering,* vol. 37, no. 6, pp. 694-702, 2010.

[58] G. Olson and M. Cohen, "A general mechanism of martensitic nucleation: Part II. FCC > BCC and other martensitic transformations," *Metallurgical and Materials Transactions A,* vol. 7, no. 12, pp. 1905-1914, 1976.

[59] R. Oshima, "Successive martensitic transformation in Fe Pd alloys," *Scripta Metallurgica,* vol. 15, no. 8, pp. 829-833, 1981.

[60] M. Watanabe and C. Wayman, "Crystallography of the martensite transformation in Fe-Al-C alloys," *Metallurgical and Materials Transactions B,* vol. 2, no. 8, pp. 2229-2236, 1971.

[61] J. Breedis and C. Wayman, "The martensitic transformation in Fe-31 WT% Ni," Urbana, 1961.

[62] D. Dunne and J. Bowles, "Measurement of the shape strain for the (225) and (259) martensitic transformations," *Acta Metallurgica,* vol. 17, no. 3, pp. 201-212, 1969.

[63] C. Cayron, "One-step model of the face-centred-cubic to body-centred-cubic martensitic transformation," *Acta Crystallographica Section A: Foundations of Crystallography,* vol. 69, no. 5, pp. 498-509, 2013.

[64] J.-P. Borg, C.-L. Chanez, A. Crochet and K. Fromm, "Polymorphism, what it is and how to identify it: a systematic review," *Royal Society of Chemistry Advances,* vol. 3, no. 38, pp. 16905-16931, 2013.

[65] M. Hatherley and W. Hutchinson, "An introduction to textures in metals," *Institution of Metallurgists,* p. 76, 1979.

[66] F. Humphreys and M. Hatherly, Recrystallization and related annealing phenomena, Elsevier, 2012.

[67] H. Bhadeshia, "Martensite in Steels," in *Materials Science & Metallurgy*, Cambridge, University of Cambridge, 2002, pp. 1-12.

[68] V. Zackay, E. Parker, D. Fahr and R. Busch, "The enhancement of ductility in high-strength steels," *ASM Trans Quart,* vol. 60, no. 2, pp. 252-259, 1967.

[69] S. Keeler, M. Kimchi and P. Mooney, "Advanced high-strength steels application guidelines version 6.0," World Auto Steel, 2017.

[70] D. Bhattacharya, "An overview of advanced high strength steel (AHSS)," Chicago, 2006.

[71] L. Kaufman and M. Cohen, "Thermodynamics and kinetics of martensitic transformations," *Progress in Metal Physics,* vol. 7, pp. 165-246, 1958.

[72] A. Perlade, O. Bouaziz and Q. Furnemont, "A physically based model for TRIP-aided carbon steels behaviour," *Materials Science and Engineering: A,* vol. 356, no. 1, pp. 145-152, 2003.

[73] A. Rusinek and J. Klepaczko, "Experiments on heat generated during plastic deformation and stored energy for TRIP steels," *Materials & Design,* vol. 30, no. 1, pp. 35-48, 2009.

[74] M. Fine and R. Guard, "Surface thermodynamic treatment of adsorption on a dislocation-suzuki locking," *Trans Metall Soc AIME, Transactions,* vol. 233, no. 7, pp. 1383-1388, 1965.

[75] J. Hirth, "Thermodynamics of stacking faults," *Metallurgical Transactions,* vol. 1, no. 9, p. 2367, 1970.

[76] R. Howard, "Relation of the stacking fault energy to segregation at stacking faults and to the occurrence of phase boundaries in fcc binary alloys," *Acta Metallurgica,* vol. 13, no. 6, pp. 655-661, 1965.

[77] F. Lecroisey and A. Pineau, "Martensitic transformations induced by plastic deformation in the Fe-Ni-Cr-C system," *Metallurgical and Materials Transactions B,* vol. 3, no. 2, pp. 391-400, 1972.

[78] G. Olson and M. Cohen, "A general mechanism of martensitic nucleation: Part I. General concepts and the FCC→HCP transformation," *Metallurgical Transactions A,* vol. 7, no. 12, pp. 1897-1904, 1976.

[79] G. Olson and M. Cohen, "A general mechanism of martensitic nucleation: Part III. Kinetics of martensitic nucleation," *Metallurgical and Materials Transactions A,* vol. 7, no. 12, pp. 1915-1923, 1976.

[80] E. Bain and N. Dunkirk, "The nature of martensite," *Trans. AIME,* vol. 70, no. 1, pp. 25-47, 1924.

[81] M. Wechsler, D. Lieberman and T. Read, "On the theory of the formation of martensite," *Journal of Metals,* vol. 197, pp. 1503-1515, 1953.

[82] J. Patel and M. Cohen, "Criterion for the action of applied stress in the martensitic transformation," *Acta Metallurgica,* vol. 1, no. 5, pp. 531-538, 1953.

[83] C. Magee, "Transformation Kinetics, Microplasticity and Aging of Martensite in Fe-31 Ni," Carnegie Institute of Technology, Pittsburgh, PA, 1966.

[84] J. Bowles and J. Mackenzie, "The crystallography of martensite transformations I," *Acta Metallurgica,* vol. 2, no. 1, pp. 129-137, 1954.

[85] S. Kundu and H. Bhadeshia, "Crystallographic texture and intervening transformations," *Scripta Materialia,* vol. 57, no. 9, pp. 869-871, 2007.

[86] J. Klostermann, "The concept of the habit plane and the phenomenological theories of the martensite transformation," *Journal of the Less Common Metals,* vol. 28, no. 1, pp. 75-94, 1972.

[87] E. Scheil, "Über die Umwandlung des Austenits in Martensit in Eisen-Nickellegierungen unter Belastung," *Zeitschrift für anorganische und allgemeine Chemie,* vol. 207, no. 1, pp. 21-40, 1932.

[88] A. Borgers and W. Burgers, "Partial dislocation on the {110} planes in the BCC lattice and the transition of the FCC into the BCC lattice," *Acta Metallurgica,* vol. 12, no. 2, pp. 255-261, 1964.

[89] G. Kurdjumov and G. Sachs, "Über den mechanismus der stahlhärtung," *Zeitschrift für Physik A Hadrons and Nuclei,* vol. 64, no. 5, pp. 325-343, 1930.

[90] Z. Nishiyama, "X-ray investigation of the mechanism of the transformation from face centered cubic lattice to body centered cubic," *Sci. Rep. Tohoku Univ.,* vol. 23, p. 637, 1934.

[91] G. Wassermann and K. Mitt, "About the mechanism of α–γ transformation of the iron," *Wilh. Inst. Wisenforsche,* vol. 17, p. 149, 1935.

[92] A. Greninger and A. Troiano, "The mechanism of martensite formation," *Trans AIME,* vol. 185, no. 9, pp. 590-598, 1949.

[93] W. Pitsch, "Z Inst. Metals, 1958, vol. 87," *Phil Mag 4,* p. 577, 1959.

[94] G. Miyamoto, N. Iwata, N. Takayama and T. Furuhara, "Mapping the parent austenite orientation reconstructed from the orientation of martensite by EBSD and its application to ausformed martensite," *Acta Materialia,* vol. 58, no. 19, pp. 6393-6403, 2010.

[95] R. von Mises, "Mechanik der festen Korper im plastisch-deformablen Zustand," *Nachrichten con der Gesellschaft der Wissenschaften zu Gottingen, Mathematisch-Physikalische Klasse,* pp. 582-292, 1913.

[96] R. Hill, "A theory of the yielding and plastic flow of anisotropic metals," *Proceedings of the Royal Society of London A,* vol. 193, pp. 281-297, 1948.

[97] W. Hosford, "A generalized isotropic yield criterion," *Journal of Applied Mechanics,* vol. 39, no. 2, pp. 607-609, 1972.

[98] F. Barlat and J. Lian, "Plastic behaviour and stretchability of sheet metals. Part I: A yield function for orthotropic sheets under plane stress condition," *International Journal of Plasticity,* vol. 5, pp. 51-66, 1989.

[99] F. Barlat, J. Brem, J. Yoon, K. Chung, R. Dick, D. Lege, F. Pourboghrat, S. Choi and E. Chu, "Plane stress yield function for aluminum alloy sheets - part 1: Theory," *International Journal of Plasticity,* vol. 19, pp. 1297-1319, 2003.

[100] F. Barlat, H. Aretz, J. Yoon, M. Karabin, J. Brem and R. Dick, "Linear transformation-based anisotropic yield functions," *Interantional Journal of Plasticity,* vol. 21, pp. 1009-1039, 2005.

[101] O. Cazacu, B. Plunkett and F. Barlat, "Orthotropic yield criterion for hexagonal closed packed metals," *Interantional Journal of Plasticity,* vol. 22, pp. 1171-1194, 2006.

[102] J. Hallquist, "LS-DYNA Theory Manual," Livermore Software Technology Corporation, Livermore, California, 2006.

[103] E. Voce, "A practical strain-hardening function," *Metallurgia,* vol. 51, no. 307, pp. 219-226, 1955.

[104] G. Cowper and P. Symonds, "Strain hardening and strain-rate effects in the impact loading of cantilevered beams," Providence, Rhode Island, 1957.

[105] G. Johnson and H. Cook, "A sonstitutive model and data for metals subjected to large strains, high strain rates and high temperatures," *Proceedings of the 7th International Symposium on Ballistics,* vol. 21, pp. 541-547, 1983.

[106] D. Mohr, M. Dunand and K. Kim, "Evaluation of associated and non-associated quadratic plasticity models for advanced high strength steel sheets under multi-axial loading," *International Journal of Plasticity,* vol. 26, no. 7, pp. 939-956, 2010.

[107] S. Panich, F. Barlat, V. Uthaisangsuk, S. Suranuntchai and S. Jirathearanat, "Experimental and theoretical formability analysis using strain and stress based forming limit diagram for advanced high strength steels," *Materials & Design,* vol. 51, pp. 756-766, 2013.

[108] T. Rahmaan, A. Bardelcik, J. Imbert, C. Butcher and M. Worswick, "Effect of strain rate on flow stress and anisotropy of DP600, TRIP780, and AA5182-O sheet metal alloys," *International Journal of Impact Engineering,* vol. 88, pp. 72-90, 2016.

[109] C. Kohar, J. Bassani, A. Brahme, W. Muhammad, R. Mishra and K. Inal, "A new multi-scale framework to incorporate microstructure evolution in phenomenological plasticity: Theory, explicit finite element formulation, implementation and validation," *International Journal of Plasticity,* 2017.

[110] E. Schmid, "Yield point of crystals, Critical shear stress law," in *Proceedings of the First International Congress for Applied Mechanics*, Delft, 1924.

[111] R. Asaro and A. Needleman, "Texture development and strain hardening in rate dependent polycrystals," *Acta Metallurgica,* vol. 33, pp. 923-953, 1985.

[112] G. Sachs, "Zur Ableitung einer Filebedingung," *Zeitschrift des Vereines Deutscher Ingenieure,* vol. 72, pp. 734-736, 1928.

[113] A. Kochendorfer, Plastiche Eigenschaften von Kristallen und Metallischen Werkstoffen, Berlin: Springer, 1941.

[114] J. Bishop and R. Hill, "A theory of the plastic distortion of a polycrystalline aggregate under combined stresses," *Philosopical Magazine,* vol. 42, pp. 414-427, 1951.

[115] J. Bishop and R. Hill, "A theoretical derivation of the plastic properties of a polycrystalline face centered metal," *Philosophical Magazine,* vol. 42, pp. 1298-1307, 1951.

[116] G. Taylor and C. Elam, "The distorsion of an aluminum crystal during a tensile test," *Proceedings of the Royal Society of London A: Mathematical, Physical and Engineering Sciences,* vol. 102, no. 719, pp. 643-667, 1923.

[117] U. Kocks, C. Tomé and H. Wenk, Texture and anisotropy: preferred orientations in polycrystals and their effect on materials properties, Cambridge University Press, 2000.

[118] K. Inal, K. Neale and A. Aboutajeddine, "Forming limit comparisons for FCC and BCC sheets," *International Journal of Plasticity,* vol. 21, pp. 1255-1266, 2005.

[119] J. Lévesque, K. Inal, K. Neale and R. Mishra, "Numerical modeling of formability of extruded magnesium alloy tubes," vol. 26, no. 1, pp. 65-83, 2010.

[120] H. Honneff and H. Mecking, "A method for the determination of the active slip systems and orientation changes during single crystal deformation," *Proceedings of ICOTOM 5, Aachen,* vol. 1, pp. 265-275, 1978.

[121] G. Canova, U. Kocks and J. Jonas, "Theory of torsional texture development," *Acta Metallurgica,* vol. 32, pp. 211-226, 1984.

[122] E. Kroner, "Berechnung der elastischen konstanten des vielkristalls aus den konstanten des einkristalls," *Zeitschrift fur Physik,* vol. 151, pp. 504-518, 1958.

[123] B. Budiansky and T. Wu, "Theoretical prediction of plastic strains of polycrystals," *Proceedings of the 4th congress of applied mechanics,* p. 1175, 1962.

[124] R. Hill, "Continuum micro-mechanics of elasto-plastic polycrystals," *Journal of mechanics and physics of solids,* vol. 13, pp. 89-101, 1965.

[125] J. Eshelby, "The deformation behaviour of the elastic field of an ellipsoidal inclusion and related problems," *Proceedings of the Royal Society London A,* vol. 241, pp. 376-396, 1957.

[126] S. Kalidindi, C. Bronkhorst and L. Anand, "Crystallographic texture evolution in bulk deformation processing of FCC metals," *Journal of Mechanics and Physics of Solids,* vol. 40, no. 3, pp. 537-569, 1992.

[127] K. Inal, P. Wu and K. Neale, "Finite element analysis of localization in FCC polycrystalline sheets under plane stress tension," *International Journal of Solids and Structures,* vol. 39, pp. 3469-3486, 2002.

[128] J. Rossiter, A. Brahme, M. Simha, K. Inal and R. Mishra, "A new crystal plasticity scheme for explicit time integration codes to simulate deformation in 3D microstructures: effects of strain path, strain rate and thermal softening on localized deformation in the aluminum alloy 5754 during simple shear," *International Journal of Plasticity,* vol. 26, no. 12, pp. 1702-1725, 2010.

[129] A. Ma, F. Roters and D. Raabe, "A dislocation density based constitutive model for crystal plasticity fem including geometrically necessary dislocations," *Acta Materialia,* vol. 54, no. 8, pp. 2169-2179, 2006.

[130] A. Izadbakhsh, K. Inal and R. Mishra, "Numerical formability assessment in single crystals of magnesium," *Computational Materials Science,* vol. 50, no. 2, pp. 571-585, 2010.

[131] A. Staroselsky and L. Anand, "Inelastic deformation of polycrystalline face centered cubic materials by slip and twinning," *Journal of the Mechanics and Physics of Solids,* vol. 46, no. 4, pp. 671-696, 1998.

[132] E. Cyr, M. Mohammadi, R. Mishra and K. Inal, "A three dimensional (3D) thermo-elasto-viscoplastic constitutive model for FCC polycrystals," *International Journal of Plasticity,* vol. 70, pp. 166-190, 2015.

[133] G. Taylor and C. Elam, "The distorsion of iron crystals," *Proceedings of the Royal Society of London. Series A, Containing Papers of a Mathematical and Physical Character,* vol. 112, no. 761, pp. 337-361, 1926.

[134] H. Gough, "The Behaviour of a Single Crystal a-Iron Subjected to ALternating Torsional Stresses," *Proceedings of the Royal Society of London. Series A, Containing Papers of a Mathematical and Physical Character,* vol. 118, no. 780, pp. 498-534, 1928.

[135] W. Fahrenhorst and E. Schmid, "Über die plastische Dehnung von α-Eisenkristallen," *Zeitschrift für Physik A Hadrons and Nuclei,* vol. 78, no. 5, pp. 383-394, 1932.

[136] F. Sauerwald and H.-G. Sossinka, "Über Sprödigkeit, Plastizität und die Gleitelemente des α-Eisens," *Zeitschrift für Physik A Hadrons and Nuclei,* vol. 82, no. 9, pp. 634-643, 1933.

[137] A. Seeger, "Why anomalous slip in body-centred cubic metals?," *Materials Science and Engineering: A,* Vols. 319-321, pp. 254-260, 2001.

[138] E. Scheil and W. Thiele, "Aenderungen von mechanischen Spannungen bei der Austenit-Martensit-Umwandlung," *Steel research international,* vol. 10, no. 10, pp. 477-480, 1937.

[139] G. Wassermann, "Untersuchungen an einer Eisen- Nickel- Legierung fiber die Verformbarkeit wahrend der α-γ-Umwandlung," *Arch Eisenhuttenwessen,* vol. 10, no. 7, pp. 321-325, 1937.

[140] L. Porter and P. Rosenthal, "Effect of applied tensile stress on phase transformation in steel," *Acta Metallurgica,* vol. 7, no. 7, pp. 504-514, 1959.

[141] M. De Jong and G. Rathenau, "Mechanical properties of iron and some iron alloys while undergoing allotropic transformation," *Acta Metallurgica,* vol. 7, pp. 246-253, 1959.

[142] G. Greenwood and R. Johnson, "The deformation of metals under small stresses during phase transformations," *Proceedings of the Royal Society of London A: Mathematical, Physical and Engineering Sciences,* vol. 283, no. 1394, pp. 403-422, 1965.

[143] J. Leblond, J. Devaux and J. Devaux, "Mathematical modelling of transformation plasticity in steels I: case of ideal-plastic phases," *International Journal of Plasticity,* vol. 5, no. 6, pp. 551-572, 1989.

[144] J. Leblond, "Mathematical modelling of transformation plasticity in steels II: coupling with strain hardening phenomena," *International Journal of Plasticity,* vol. 5, no. 6, pp. 573-591, 1989.

[145] F. Fischer, "A micromechanical model for transformation plasticity in steels," *Acta Mettallurgica et Materialia,* vol. 38, no. 8, pp. 1535-1546, 1990.

[146] F. Fischer, "Transformation induced plasticity in triaxially loaded steel specimens subjected to a martensitic transformation," *European journal of mechanics. A. Solids,* vol. 11, no. 2, pp. 233-244, 1992.

[147] F. Fischer, "Modelling and simulation of transformation induced plasticity in elasto-plastic materials," *Mechanics of solids with phase changes,* pp. 189-237, 1997.

[148] J. Venables, "The interaction of fast-moving dislocation," *Philosophical Magazine,* vol. 10, no. 107, pp. 771-778, 1964.

[149] P. Mangonon and G. Thomas, "The martensite phases in 304 stainless steel," *Metallurgical and Materials Transactions B,* vol. 1, no. 6, pp. 1577-1586, 1970.

[150] W. Gerberich, G. Thomas, E. Parker and V. Zackary, "Metastable austenites: decomposition and strength," *Second international conference on strength of metal and alloys,* pp. 894-899, 1970.

[151] R. Stringfellow and D. Parks, "A self-consistent model of isotropic viscoplastic behavior in multiphase materials," *International Journal of Plasticity,* vol. 7, no. 6, pp. 529-547, 1991.

[152] R. Stringfellow, D. Parks and G. Olson, "A constitutive model for transformation plasticity accompanying strain-induced martensitic transformations in metastable austenitic steels," *Acta Metallurgica et Materialia,* vol. 40, no. 7, pp. 1703-1716, 1992.

[153] T. Iwamoto and T. Tsuta, "Computational simulation of the dependence of the austenitic grain size on the deformation behavior of TRIP steels," *International Journal of Plasticity,* vol. 16, pp. 791-804, 2000.

[154] T. Iwamoto and T. Tsuta, "Computational simulation on deformation behavior of CT specimens of TRIP stel under mode I loading for evaluation of fracture toughness," *International Journal of Plasticity,* vol. 18, no. 11, pp. 1583-1606, 2002.

[155] Y. Tomita and T. Iwamoto, "Constitutive modeling of TRIP steel and its application to the improvement of mechanical properties," *International Journal of Mechanical Sciences,* vol. 37, no. 12, pp. 1295-1305, 1995.

[156] C. Kohar, M. Cherkaoui, H. El Kadiri and K. Inal, "Numerical modeling of TRIP steel in axial crashworthiness," *International Journal of Plasticity,* vol. 84, pp. 224-254, 2016.

[157] M. Cherkaoui, M. Berveiller and H. Sabar, "Micromechanical modelling of martensitic transformation induced plasticity (TRIP) in austenitic single crystals," *International Journal of Plasticity,* vol. 14, no. 7, pp. 597-626, 1998.

[158] M. Cherkaoui, A. Soluami, A. Zeghloul and M. Khaleel, "A phenomenological dislocation theory for martensititic transformation in ductile materials: from micro-to macroscopic description," *Philosophical Magazine,* vol. 88, no. 30-32, pp. 3479-3512, 2008.

[159] M. Cherkaoui, M. Berveiller and X. Lemoine, "Couplings between plasticity and martensitic phase transformation: overall behavior of polycrystalline TRIP steels," *International Jounral of Plasticity,* vol. 16, pp. 1215-1241, 2000.

[160] R. Kubler, M. Berveiller, M. Cherkaoui and K. Inal, "Transformation textures in unstable austenitic steel," *Journal of Engineering Materials and Technology,* vol. 125, no. 1, pp. 12-17, 2003.

[161] J. Serri and M. Cherkaoui, "Constitutive modeling and finite element analysis of the formability of TRIP steels," *Journal of Engineering Materials and Technology,* vol. 130, no. 3, p. 031009, 2008.

[162] K. Choi, W. Liu, X. Sun and M. Khaleel, "Microstructure-based constitutive modeling of TRIP steel: prediction of ductity and failure modes under different loading conditions," *Acta Materialia,* vol. 57, no. 8, pp. 2592-2604, 2009.

[163] E. Kim, W. Woo, Y. Heo, B. Seong, J. Choi and S. Choi, "Effect of kinematic stability of the austenite phase on phase transformation behavior and deformation heterogeneity in duplex stainless steel using the crystal plasticity finite element method," *International Journal of Plasticity,* vol. 79, pp. 48-67, 2016.

[164] S. Keeler, "Plastic instability and fracture in sheets stretched over rigid punches, Ph.D Thesis," Massachusetts Institute of Technology, Cambridge, MA, 1961.

[165] S. Keeler and W. Backofen, "Plastic instability and fracture in sheets stretched over rigid punches," *ASM TRANS Q*, vol. 56, no. 1, pp. 25-48, 1963.

[166] G. Goodwin, "Application of strain analysis to sheet metal forming in the press shop," *SAE Technical Paper 680093*, 1968.

[167] I. 12004-2:2008, "Metallic materials -- Sheet and strip -- Determination of forming-limit curves - Part 2: Determination of forming-limit curves in the laboratory," International Organization for Standardization, 2008.

[168] K. Chung, C. Lee and H. Kim, "Forming limit criterion for ductile anisotropic sheets as a material property and its deformation path insensitivity, Part II: Boundary value problems," *International Journal of Plasticity*, vol. 58, pp. 35-65, 2014.

[169] S. Hecker, "A cup test for accessing stretchability," *Metals Engineering Quarterly*, vol. 14, pp. 30-36, 1974.

[170] A. Ghosh and S. Hecker, "Failure in thin sheets stretched over rigid punches," *Metallurgical Transactions A*, vol. 6, no. 5, pp. 1065-1074, 1975.

[171] K. Nakazima, T. Kikuma and K. Hasuka, "Study on the formability of steel sheets," Yawata Tech. Report No. 264, 1968, pp. 8517-8530.

[172] Z. Marciniak, "Limits of sheet metal formability," *WNT, Warsaw in Polish*, 1971.

[173] B. E. I. 20482:2003, "Metallic Materials- Sheet and Strip- Erichsen Cupping Test," British Standards Institution, 2003.

[174] K. Sugimoto, M. Kobayashi, A. Nagasaka and S. Hashimoto, "Warm stretch-formability of TRIP-aided dual-phase sheet steels," *ISIJ International*, vol. 35, no. 11, pp. 1407-1414, 1995.

[175] S. Peterson, M. Mataya and D. Matlock, "The formability of austenitic stainless steels," *JOM Journal of the Minerals, Metals and Materials Society*, vol. 49, no. 9, pp. 54-58, 1997.

[176] W. Bleck, J. Ohlert and K. Papamantellos, "Sheet metal forming behaviour and mechanical properties of TRIP steels," *Steel Research, International*, vol. 70, no. 11, pp. 472-479, 1999.

[177] C. Lee, S. Kim, T. Lee and S. Lee, "Effects of volume fraction and stability of retained austenite on formability in a 0.1 C–1.5 Si–1.5 Mn–0.5 Cu TRIP-aided cold-rolled steel sheet," *Materials Science and Engineering A*, vol. 371, no. 1, pp. 16-23, 2004.

[178] P. Verleysen, J. Peirs, J. Van Slycken, K. Faes and L. Duchene, "Effect of strain rate on the forming behaviour of sheet metals," *Journal of Materials Processing Technology*, vol. 211, no. 8, pp. 1457-1464, 2011.

[179] D. Hao, D. Hua, C. Qiu, Z. Tang, J. Zeng and Y. Ping, "Formability of TRIP/TWIP steel containing manganese of 18.8%," *Journal of Iron and Steel Research, International*, vol. 18, no. 1, pp. 36-40, 2011.

[180] V. Talyan, R. Wagoner and J. Lee, "Formability of stainless steel," *Metallurgical and Materials Transactions A*, vol. 29, no. 8, pp. 2161-2172, 1998.

[181] H. Swift, "Plastic instability under plane stress," *Journal of the Mechanics and Physics of Solids*, vol. 1, no. 1, pp. 1-18, 1952.

[182] R. Hill, "On discontinuous plastic states, with special reference to localized necking in thin sheets," *Journal of the Mechanics and Physics of Solids*, vol. 1, no. 1, pp. 19-30, 1952.

[183] J. Hutchinson, K. Neale and A. Needleman, "Sheet Necking I: Validity of Plane Stress Assumption of the Long-Wavelength Approximation," *Mechanics of Sheet Metal Forming*, vol. 1, pp. 111-126, 1978.

[184] J. Hutchinson and K. Neale, "Sheet necking II: Time-independent behavior," *Mechanics of sheet metal forming,* pp. 127-152, 1978.

[185] J. Hutchinson and K. Neale, "Sheet necking III: Strain-rate effects," *Mechanics of sheet metal forming,* pp. 269-285, 1978.

[186] M. Azrin and W. Backofen, "The deformation and failure of a biaxially stretched sheet," *Metallurgical and Materials Transactions B,* vol. 1, no. 10, pp. 2857-2865, 1970.

[187] S. Stroen and J. Rice, "Localized necking in thin sheets," *Journal of the Mechanics and Physics of Solids,* vol. 23, no. 6, pp. 421-441, 1975.

[188] J. Bassani, J. Hutchinson and K. Neale, "On the prediction of necking in anisotropic sheets," *Metal Forming Plasticity,* pp. 1-13, 1979.

[189] J. Lian, F. Barlat and B. Baudelet, "Plastic behaviour and stretchability of sheet metals. Part II: Effect of yield surface shape on sheet forming limit," *International Journal of Plasticity,* vol. 5, no. 2, pp. 131-147, 1989.

[190] P. Dasappa, K. Inal and R. Mishra, "The effects of anisotropic yield functions and their material parameters on prediction of forming limit diagrams," *International Journal of Solids and Structures,* vol. 49, pp. 3528-3550, 2012.

[191] F. Barlat, "Crystallographic texture, anisotropic yield surface and forming limits of sheet metals," *Materials Science and Engineering,* vol. 91, pp. 55-72, 1987.

[192] F. Barlat and O. Richmond, "Prediction of tricomponent plane stress yield surfaces and associated flow and failure behavior of strongly textured fcc polycrystalline sheets," *Materials Science and Engineering,* vol. 95, pp. 15-29, 1987.

[193] F. Barlat, "Forming limit diagrams - predictions based on some microstructual aspects of materials," *Forming Limit Diagrams: Concepts, Methods, and Applications,* pp. 275-301, 1989.

[194] D. Lege, F. Barlat and J. Brem, "Characterization and modeling of the mechanical behavior and formability of a 2008-T4 sheet sample," *International Journal of Mechanical Science,* vol. 31, pp. 549-563, 1989.

[195] V. Tvergaard and A. Needleman, "Shear band development in polycrystals," *Proceedings of the Royal Society of London A,* vol. 22, pp. 219-231, 1993.

[196] Y. Zhou and K. Neale, "Predictions of forming limit diagrams using a rate-sensitive crystal plasticity model," *International Journal of Mechanical Sciences,* vol. 37, pp. 1-20, 1995.

[197] Y. Qiu, K. Neale, A. Makinde and S. MacEwen, "Numerical modelling of metal formability using polycrystal plasticity," *Simulation of materials processing: theory, methods and applications,* pp. 327-331, 1995.

[198] P. Wu, K. Neale and E. Van der Giessen, "On crystal plasticity FLD analysis," *Proceedings of the Royal Society of London A: Mathematical, Physical and Engineering Sciences,* vol. 453, pp. 1813-1848, 1997.

[199] E. Cyr, M. Mohammadi, A. Brahme, R. Mishra and K. Inal, "Modelling the formability of aluminum alloys at elevated temperatures using a new thermo-elasto-viscoplastic crystal plasticity framework," *International Journal of Mechanical Sciences,* 2017.

[200] Z. Tourki, H. Bargui and H. Sidhom, "The kinetic of induced martensitic formation and its effect on forming limit curves in the AISI 304 stainless steel," *Journal of Materials Processing Technology,* vol. 166, pp. 330-336, 2005.

[201] H. Campos, M. Butuc, J. Gracio, J. Rocha and J. Duarte, "Theoretical and experimental determination of the forming limit diagram for the AISI 304 stainless steel," *Journal of Materials Processing Technology,* vol. 179, no. 1, pp. 56-60, 2006.

[202] R. Makkouk, N. Bourgeois, J. Serri, B. Bolle, M. Martiny, M. Teaca and G. Ferron, "Experimental and theoretical analysis of the limits to ductility of type 304 stainless steel sheet," *European Journal of Mechanics-A/Solids,* vol. 27, no. 2, pp. 181-194, 2008.

[203] D. Connolly, C. Kohar, R. Mishra and K. Inal, "A New Coupled Thermomechanical Framework for Modeling Formability in Transformation Induced Plasticity Steels," *Under Review: International Journal of Plasticity,* 2018.

[204] D. Peirce, R. Asaro and A. Needleman, "An analysis of nonuniform and localized deformation in ductile single crystals," *Acta Metallurgica,* vol. 30, no. 6, pp. 1087-1119, 1982.

[205] C. Bronkhorst, S. Kalidindi and L. Anand, "Polycrystalline plasticity and the evolution of crystallographic texture in FCC metals," *Proceedings of the Royal Society A: Mathematical, Physical and Engineering Sciences,* vol. 341, pp. 443-477, 1992.

[206] Y. Chang and R. Asaro, "An experimental study of shear localization in aluminum-copper single crystals," *Acta Metallurgica,* vol. 29, no. 1, pp. 241-257, 1981.

[207] J. Bassani and T. Wu, "Latent hardening in single crystals II. Analytical characterization and predictions," *Proceedings: Mathematical and Physical Sciences,* vol. 435, no. 1893, pp. 21-41, 1991.

[208] D. Peirce, R. Asaro and A. Needleman, "Material rate dependence and localized deformation in crystalline solids," *Acta Metallurgica,* vol. 31, no. 12, pp. 1951-1976, 1983.

[209] D. Peirce, C. Shih and A. Needleman, "A tangent modulus method for rate dependent solids," *Computers and Structures,* vol. 18, no. 5, pp. 875-887, 1984.

[210] E. Van der Giessen and K. Neale, "Analysis of the inverse Swift effect using a rate-sensitive polycrystal model," *Computer methods in applied mechanics and engineering,* vol. 103, no. 1, pp. 291-313, 1993.

[211] T. O. A. f. Windows, "EDAX TSL," TexSem Laboratories Inc., Draper, UT, USA, 2004.

[212] F. Bachmann and R. Hielscher, "Texture analysis with MTEX-free and open source software toolbox," *Solid State Phenomena,* vol. 160, pp. 63-68, 2010.

[213] S. Freour, D. Gloaguen, M. Francois and R. Guillen, "Modelling and simulation of multi-phase effects on X-ray elasticity constants," *Physica Status Solidi (b),* vol. 239, no. 2, pp. 297-309, 2003.

[214] C. Seo, K. Kwon, K. Choi, K. Kim, J. Kwak, S. Lee and N. Kim, "Deformation behavior of ferrite–austenite duplex lightweight Fe–Mn–Al–C steel," *Scripta Materialia,* vol. 66, no. 8, pp. 529-522, 2012.

[215] Z. Cai, H. Ding, X. Xue and Q. Xin, "Microstructural evolution and mechanical properties of hot-rolled 11% manganese TRIP steel," *Materials Science and Engineering A,* vol. 560, pp. 388-395, 2013.

[216] N. Gey, B. Petit and M. Humbert, "Electron backscattered diffraction study of ε/α′ martensitic variants induced by plastic deformation in 304 stainless steel," *Metallurgical and Materials Transaction A,* vol. 36, no. 12, pp. 3291-3299, 2005.

[217] C.-C. Young, "Transformation toughening of phosphocarbide-strengthened austenitic steels," Massachusetts Institute of Technology, Cambridge, MA, 1988.

[218] A. Lebedev and V. Kosarchuk, "Influences of phase transformations on the mechnaical properties of austenitic stainless steels," *International Journal of Plasticity,* vol. 16, no. 7, pp. 749-767, 2000.

[219] Q. Furnemont, "The micromechanics of TRIP-assisted multiphase steels," Université Catholique de Louvain, Louvain, Belgium, 2003.

[220] A. Beese and D. Mohr, "Effect of stress triaxiality and Lode angle on the kinetics of strain-induced austenite-to-martensite transformation," *Acta Materialia,* vol. 59, no. 7, pp. 2589-2600, 2011.

[221] J. Serri, "Caractérisation expérimentale et modélisation du comportement plastique d'aciers à transformation martensitique: applications à la mise en forme," University of Lorraine, Nancy, France, 2006.

[222] P. Eyckens, A. Van Bael and P. Van Houtte, "An extended Marciniak–Kuczynski model for anisotropic sheet subjected to monotonic strain paths with through-thickness shear," *International Journal of Plasticity,* vol. 27, no. 10, pp. 1577-1597, 2011.

[223] M. Zhang, L. Li, Y. Su, R. Fu, Z. Wan and B. De Cooman, "Forming Limit Curve (FLC) and Fracture Mechanism of Newly Developed Low-Carbon Low-Silicon TRIP Steel," *Steel Research International,* vol. 78, no. 6, pp. 501-505, 2007.

[224] M. Mohammadi, A. Brahme, R. Mishra and K. Inal, "Effects of post-necking hardening behavior and equivalent stress–strain curves on the accuracy of M–K based forming limit diagrams," *Computational Materials Science,* vol. 85, pp. 316-323, 2014.

[225] L. Durrenberger, J. Klepaczko and A. Rusinek, "Constitutive Modeling of Metals Based on the Evolution of the Strain-Hardening Rate," *Journal of Engineering Materials and Technology,* vol. 129, no. 4, pp. 550-558, 2007.

[226] W. Dan, W. Zhang, S. Li and Z. Lin, "A model for strain-induced martensitic transformation of TRIP steel with strain rate," *Computation Materials Science,* vol. 40, pp. 101-107, 2007.

[227] J. Krauer and P. Hora, "Enhanced material models for the process design of the temperature dependent forming behavior of metastable steels," *International Journal of Material Forming,* vol. 5, no. 4, pp. 361-370, 2012.

[228] R. Lebensohn and C. Tomé, "A self-consistent anisotropic approach for the simulation of plastic deformation and texture development of polycrystals: application to zirconium alloys," *Acta metallurgica et materialia,* vol. 41, no. 9, pp. 2611-2624, 1993.

[229] J. Clayton, "Dynamic plasticity and fracture in high density polycrystals: constitutive modeling and numerical simulation," *Journal of the Mechanics and Physics of Solids,* vol. 53, no. 2, pp. 261-301, 2005.

APPENDIX

A.1 – Texture Evolution Plots with Respect to Effective Strain for Plane Strain

Table A1-1: Plane strain tension $\rho = 0.0$ along RD γ- austenite texture at a) 0% b) 10% c) 20% d) 30% e) 40% effective strain
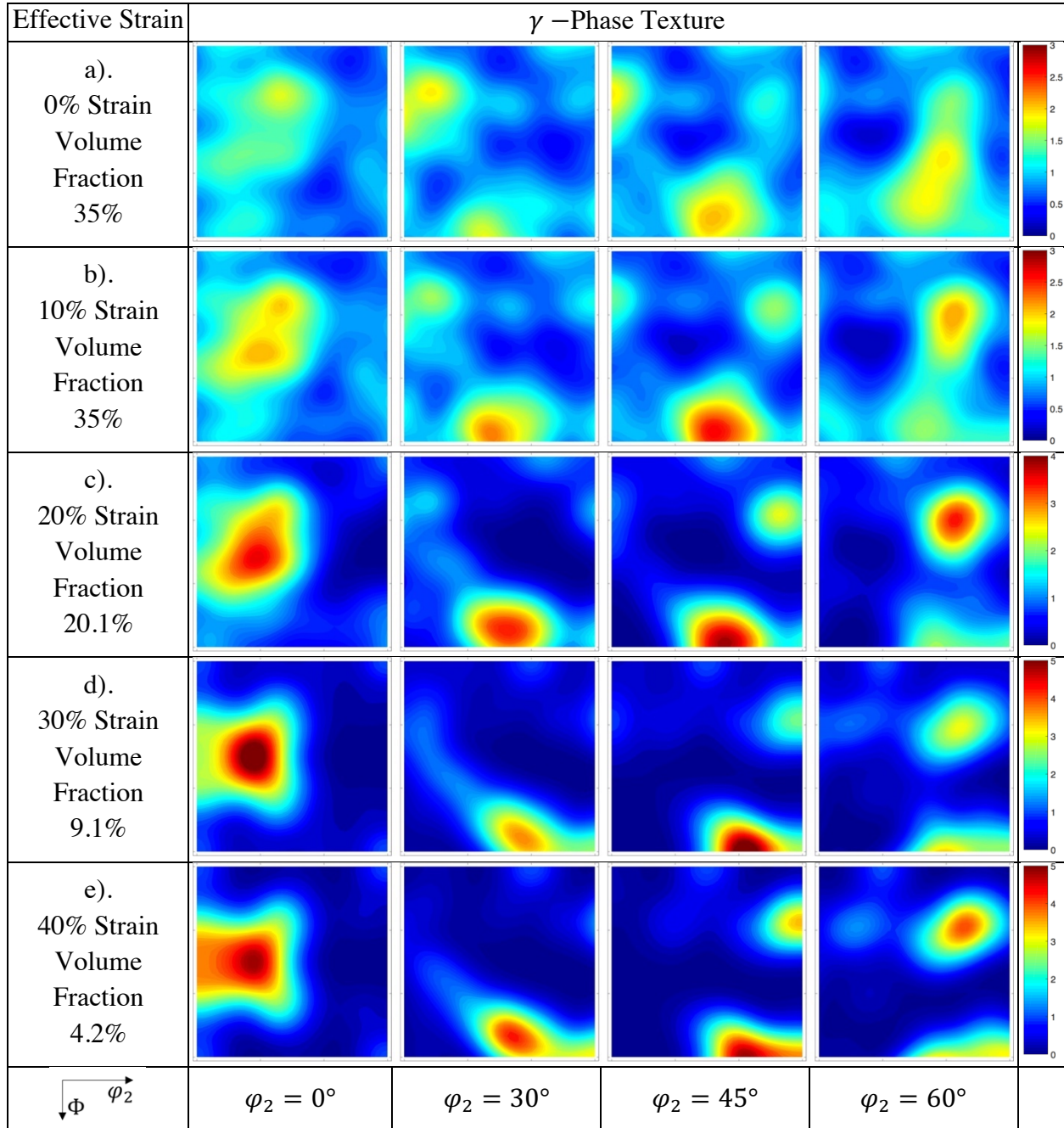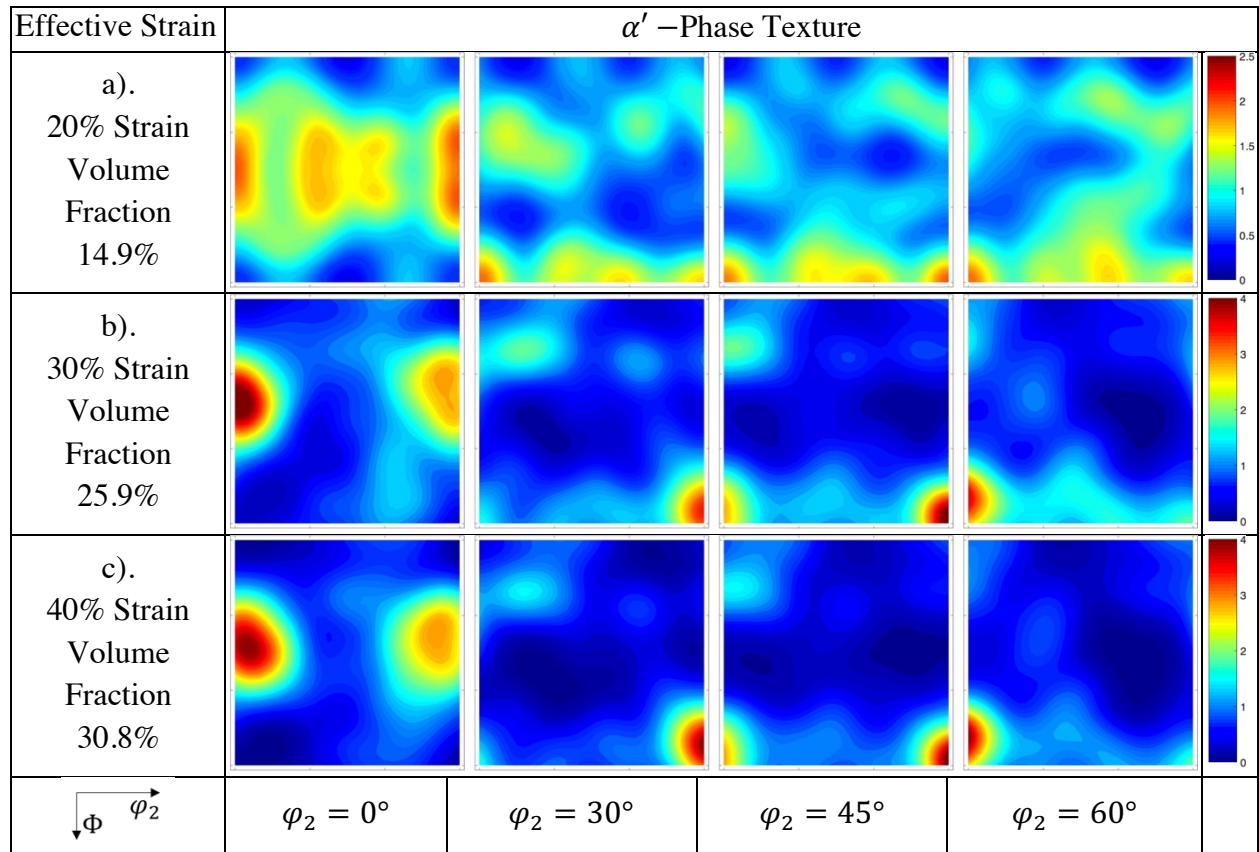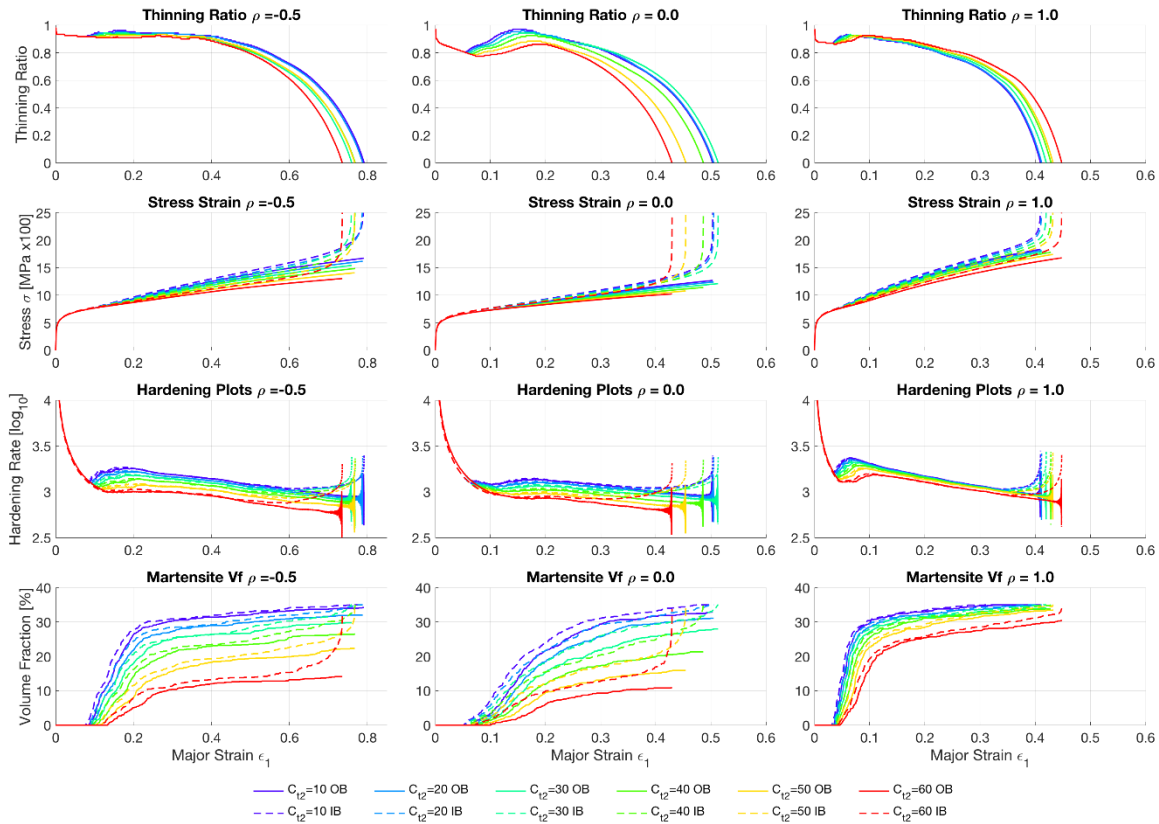
Effective Strain	γ −Phase Texture				
a). 0% Strain Volume Fraction 35%					
b). 10% Strain Volume Fraction 35%					
c). 20% Strain Volume Fraction 20.1%					
d). 30% Strain Volume Fraction 9.1%					
e). 40% Strain Volume Fraction 4.2%					
Φ φ_2	$\varphi_2 = 0°$	$\varphi_2 = 30°$	$\varphi_2 = 45°$	$\varphi_2 = 60°$	

Table A1-2: Plane strain tension $\rho = 0.0$ along RD α'- martensite texture at a) 20% b) 30% c) 40% effective strain

Effective Strain	α' −Phase Texture				
a). 20% Strain Volume Fraction 14.9%					
b). 30% Strain Volume Fraction 25.9%					
c). 40% Strain Volume Fraction 30.8%					
Φ φ_2	$\varphi_2 = 0°$	$\varphi_2 = 30°$	$\varphi_2 = 45°$	$\varphi_2 = 60°$	

A.2 – Texture Evolution Plots with Respect to Effective Strain for Biaxial

Table A2-1: Equi-biaxial tension $\rho = 1.0$ γ- austenite texture at a) 0% b) 10% c) 20% d) 30% e) 40% effective strain

Effective Strain	γ −Phase Texture				
a). 0% Strain Volume Fraction 35%					
b). 10% Strain Volume Fraction 35%					
c). 20% Strain Volume Fraction 9.1%					
d). 30% Strain Volume Fraction 1.4%					
e). 40% Strain Volume Fraction 0.9%					
Φ φ_2	$\varphi_2 = 0°$	$\varphi_2 = 30°$	$\varphi_2 = 45°$	$\varphi_2 = 60°$	
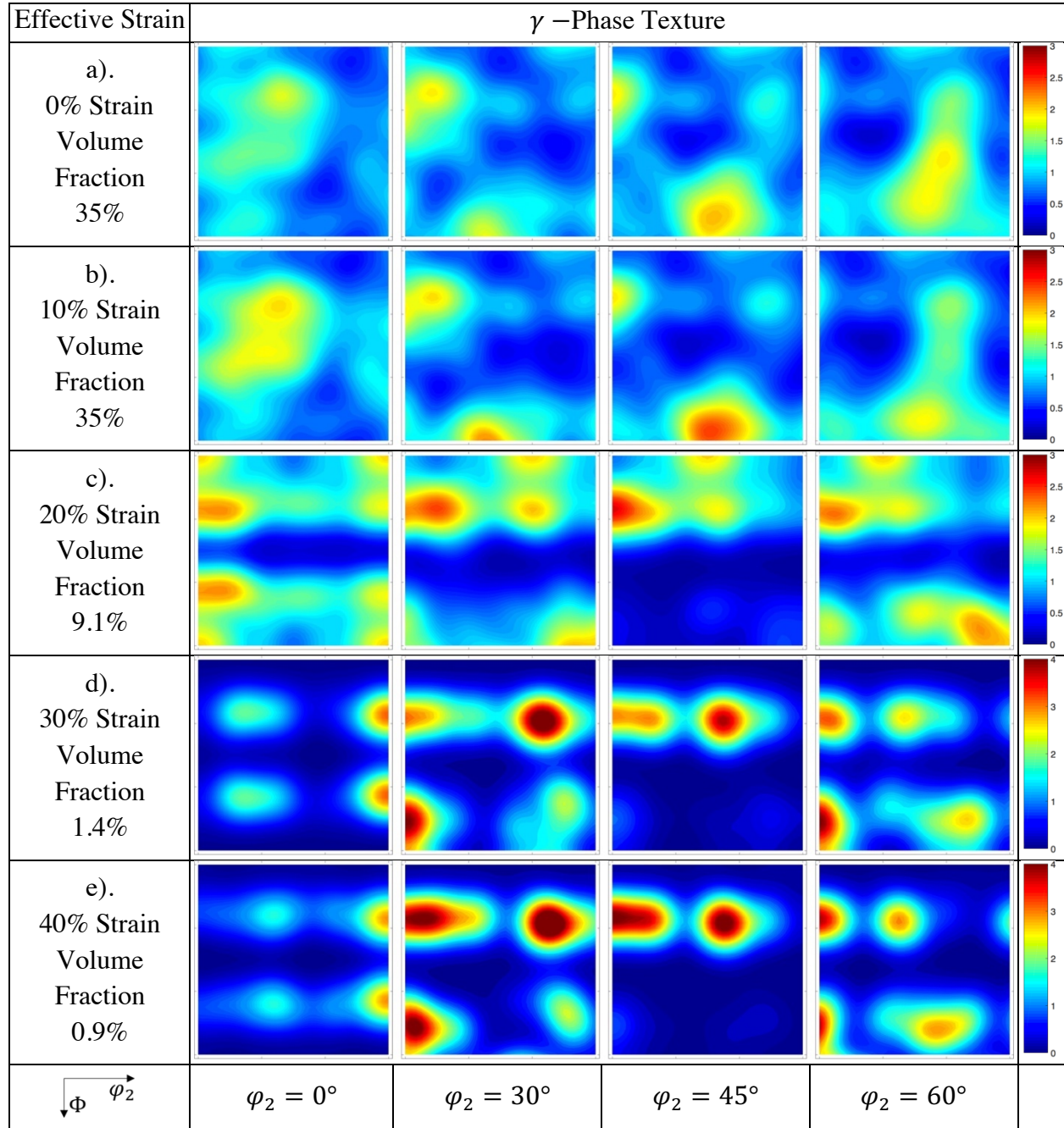
Table A2-2: Equi-biaxial tension $\rho = 1.0$ α'- martensite texture at a) 20% b) 30% c) 40% effective strain

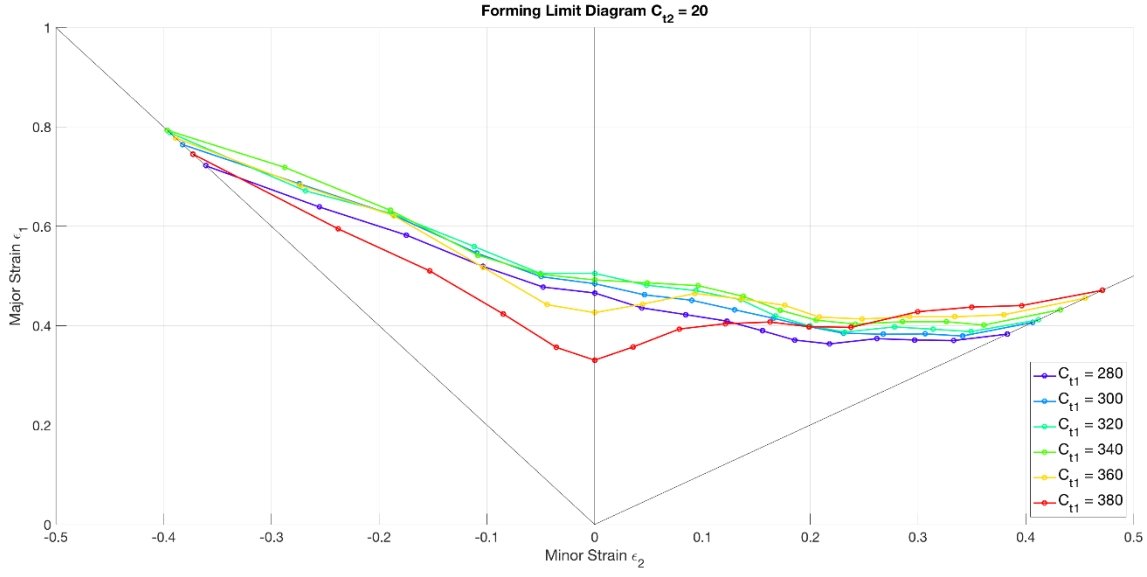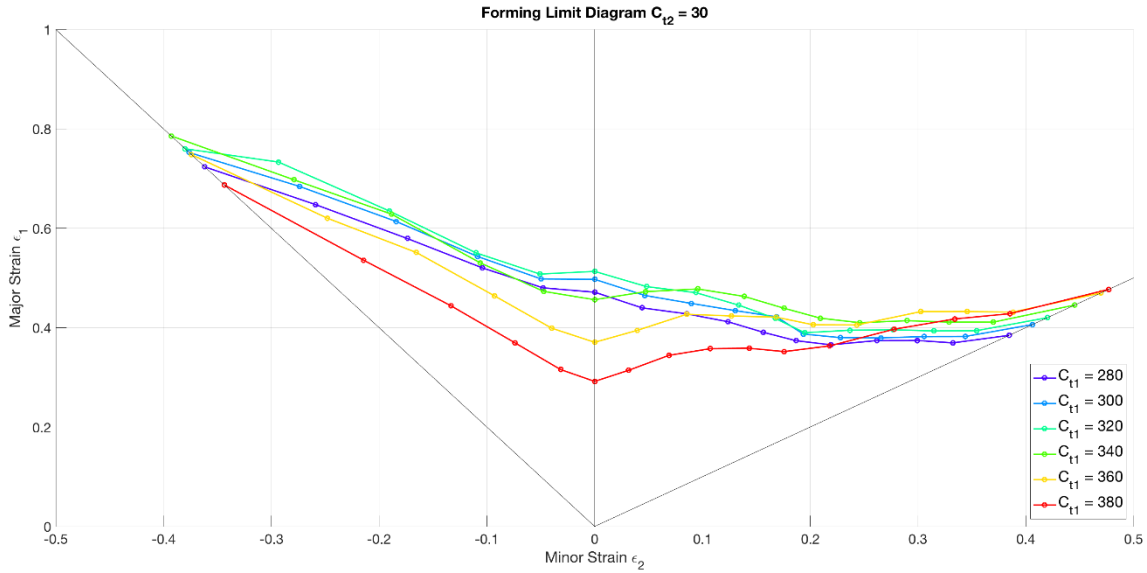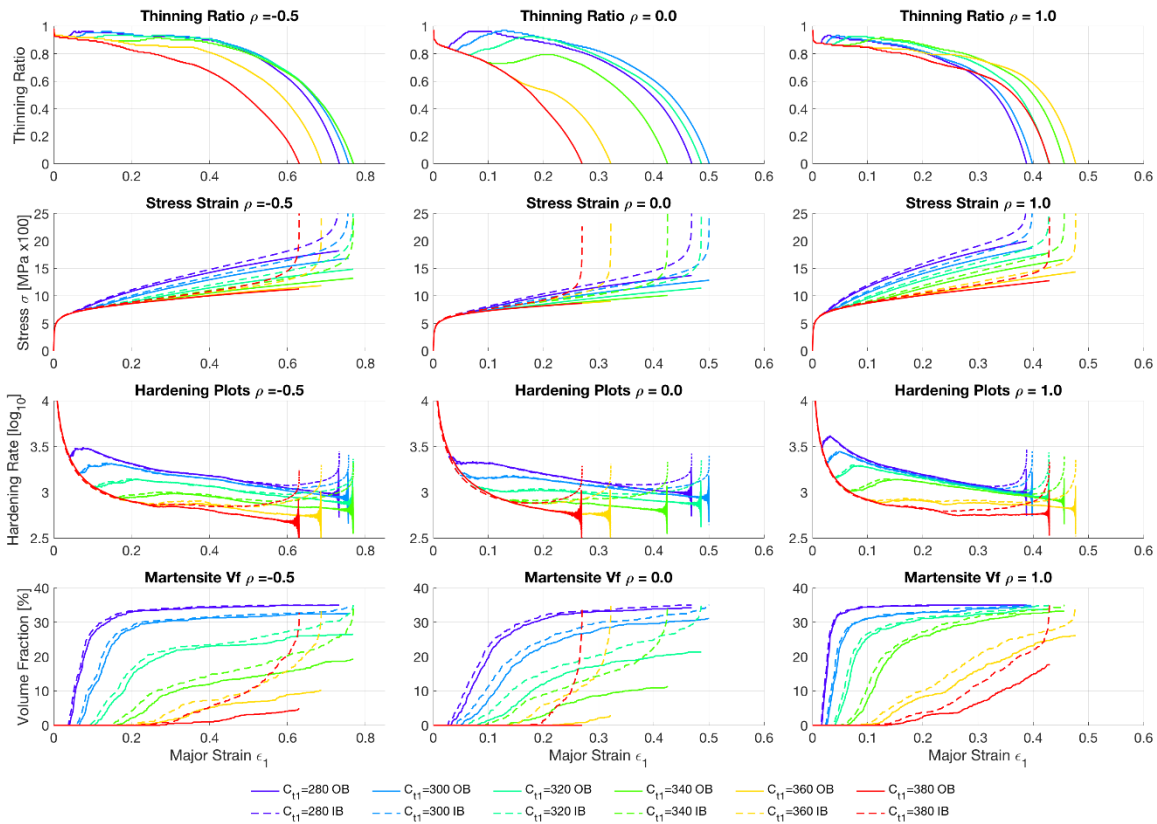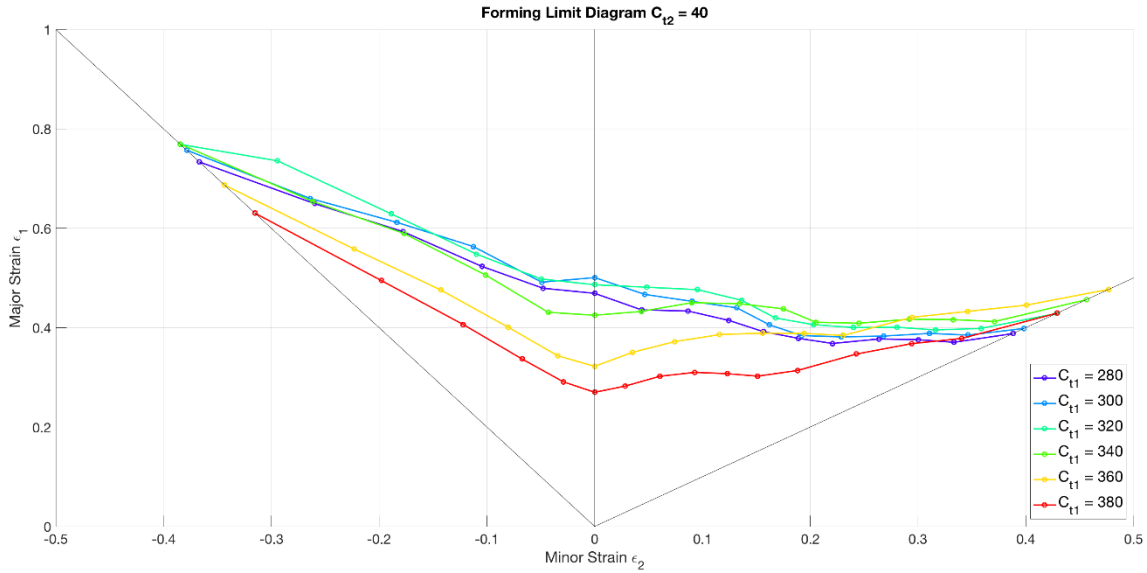| Effective Strain	α' −Phase Texture				
a). 20% Strain Volume Fraction 25.9%					
b). 30% Strain Volume Fraction 33.6%					
c). 40% Strain Volume Fraction 34.1%					
$\downarrow\Phi$ $\overrightarrow{\varphi_2}$	$\varphi_2 = 0°$	$\varphi_2 = 30°$	$\varphi_2 = 45°$	$\varphi_2 = 60°$	
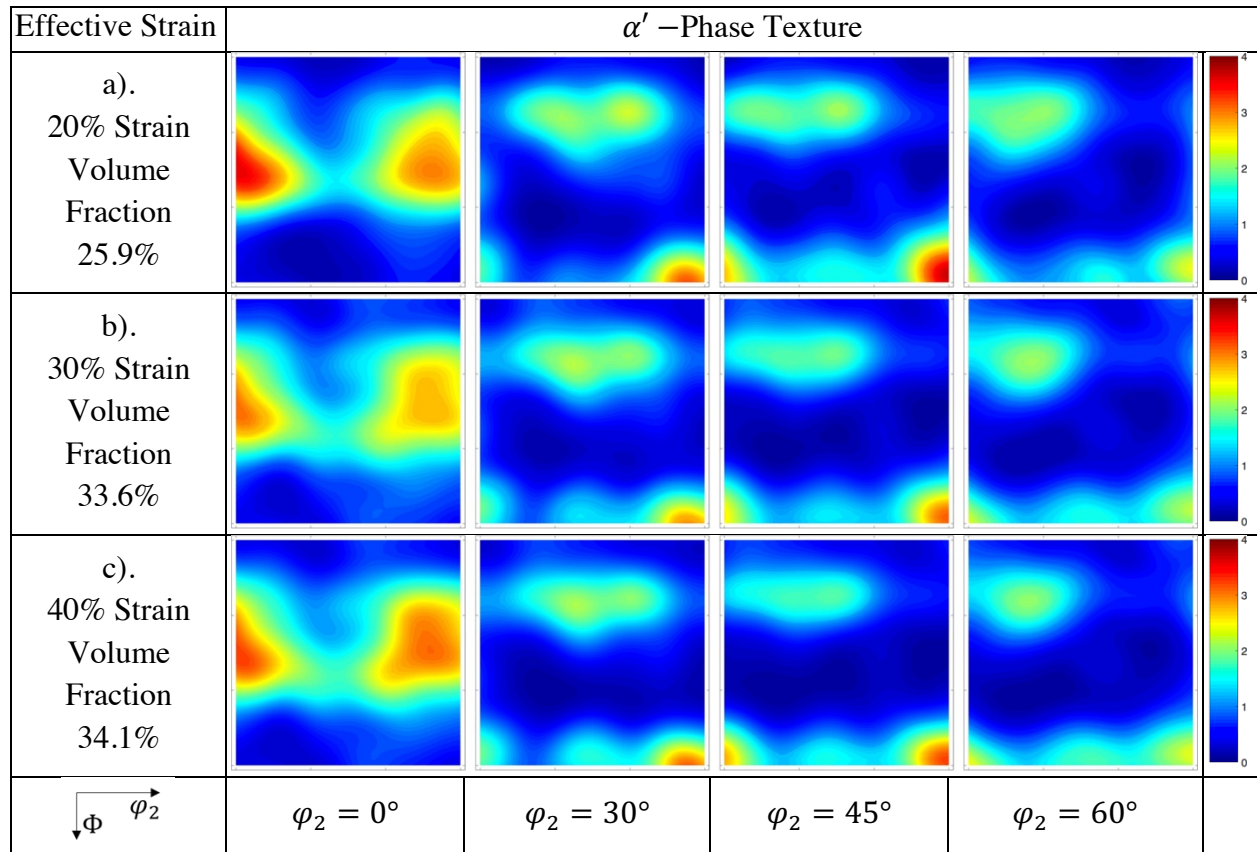
A.3 – Transformation Threshold Parametric Study Plots

Forming Limit Diagram $C_{t1} = 300$

Forming Limit Diagram $C_{t1} = 320$

Forming Limit Diagram $C_{t1} = 340$

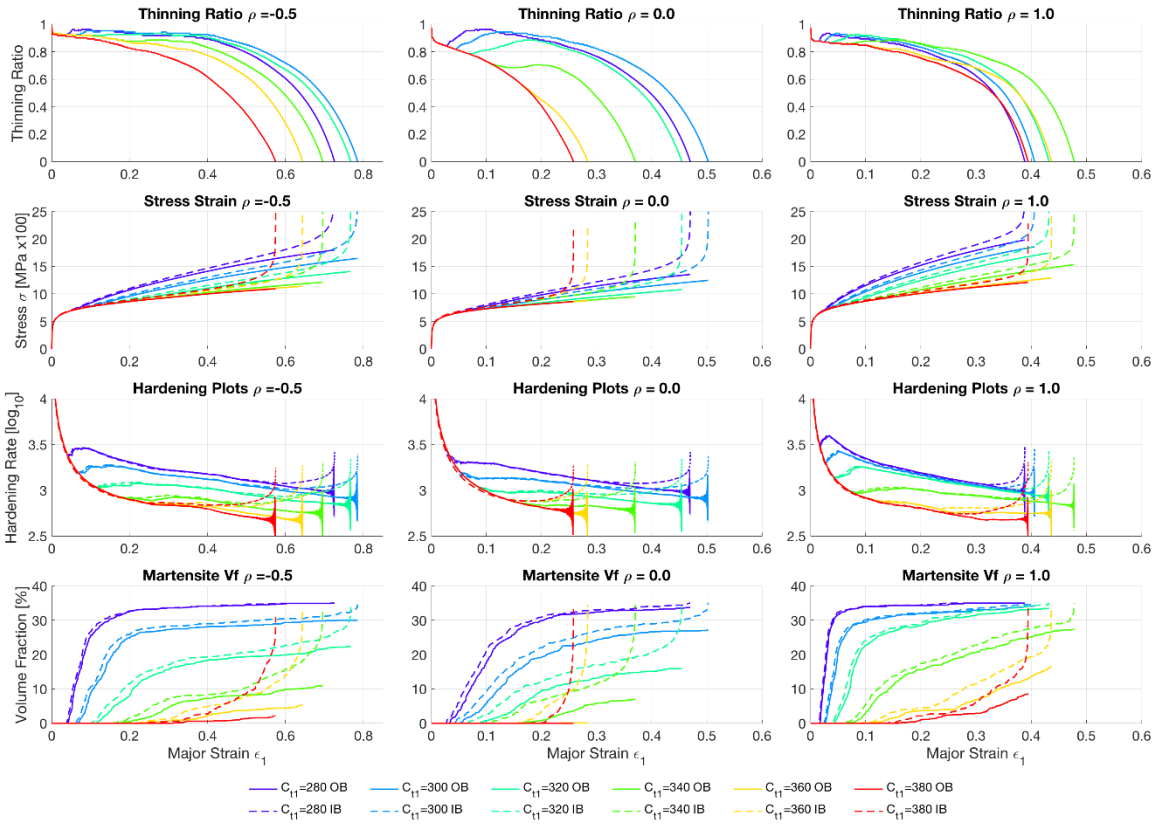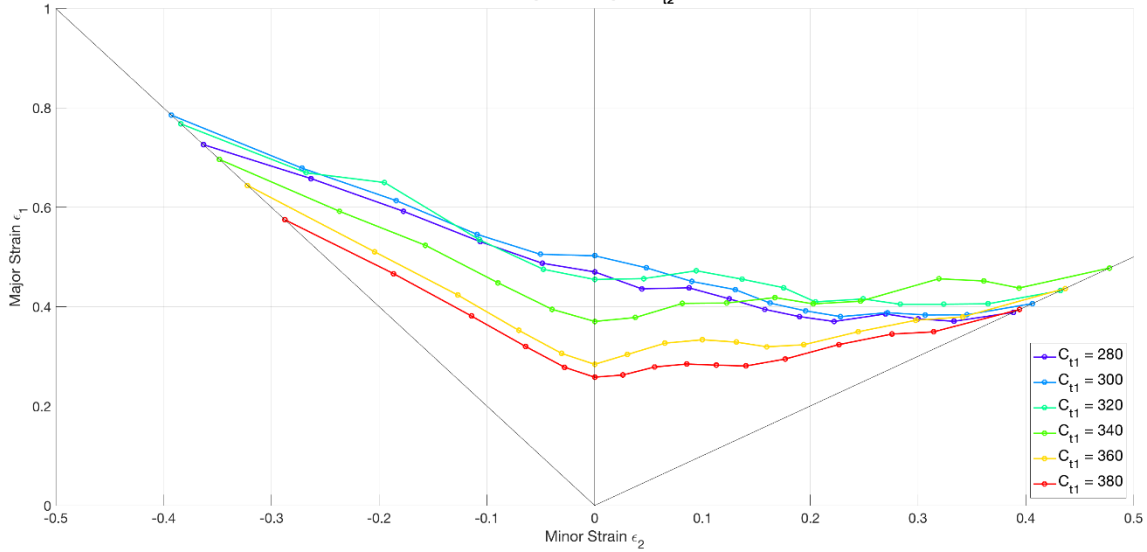Forming Limit Diagram $C_{t1} = 360$

123

Forming Limit Diagram $C_{t2} = 20$

Forming Limit Diagram $C_{t2} = 30$

125

Forming Limit Diagram $C_{t2} = 40$

127

Forming Limit Diagram $C_{t2} = 60$